

January 2015

"Transistor-Like" Spin Nano-Switches: Physics and Applications

Vinh Quang Diep
Purdue University

Follow this and additional works at: https://docs.lib.purdue.edu/open_access_dissertations

Recommended Citation

Diep, Vinh Quang, ""Transistor-Like" Spin Nano-Switches: Physics and Applications" (2015). *Open Access Dissertations*. 1458.
https://docs.lib.purdue.edu/open_access_dissertations/1458

This document has been made available through Purdue e-Pubs, a service of the Purdue University Libraries. Please contact epubs@purdue.edu for additional information.

**PURDUE UNIVERSITY
GRADUATE SCHOOL
Thesis/Dissertation Acceptance**

This is to certify that the thesis/dissertation prepared

By Vinh Quang Diep

Entitled

"TRANSISTOR-LIKE" SPIN NANO-SWITCHES: PHYSICS AND APPLICATIONS

For the degree of Doctor of Philosophy

Is approved by the final examining committee:

Prof. Supriyo Datta

Chair

Prof. Joerg Appenzeller

Prof. Zhihong Chen

Dr. Behtash Behin-Aein

To the best of my knowledge and as understood by the student in the Thesis/Dissertation Agreement, Publication Delay, and Certification Disclaimer (Graduate School Form 32), this thesis/dissertation adheres to the provisions of Purdue University's "Policy of Integrity in Research" and the use of copyright material.

Approved by Major Professor(s): Prof. Supriyo Datta

Approved by: Michael R. Melloch

Head of the Departmental Graduate Program

4/20/2015

Date

“TRANSISTOR-LIKE” SPIN NANO-SWITCHES: PHYSICS AND
APPLICATIONS

A Dissertation

Submitted to the Faculty

of

Purdue University

by

Vinh Quang Diep

In Partial Fulfillment of the

Requirements for the Degree

of

Doctor of Philosophy

May 2015

Purdue University

West Lafayette, Indiana

ACKNOWLEDGMENTS

First of all, it has been a great honor working with and learning from an original thinker as Professor Supriyo Datta who has always sought for the essence of complex problems. Simplicity, especially for Ph.D. level research problems, certainly does not come naturally without enormous effort. I can not remember how many times he asked: ‘Can you explain your research to a high school student?’. The strong driving force for clear thinking has greatly influenced my academics and future career. For this, I am deeply indebted to Professor Datta and I am also very grateful for what he has been guiding and supporting me through out my Ph.D. life.

I would like to express my sincere gratitude to Professor Joerg Appenzeller and Professor Zhihong Chen for giving me opportunities to participate in their researches. The interaction with the best experimentalists has shaped my thinking about the experimental challenges and this is one of the most important experiences for a theorist like me.

I especially would like to thank Dr. Behtash Behin-Aein for helping me during the early days of my Ph.D. period. I thank him for introducing me to the field of neural network in which I am very much interested. I highly appreciate his valuable feedbacks and suggestions on many topics in my research.

I would like to thank my colleagues: Dr. Seokmin Hong, Brian Sutton, Dr. Srikant Srinivasan, Dr. Angik Sarkar, Chia-Ching Lin, Ashish V. Penumatcha, Kerem Yunus Camsari, Samiran Ganguly and Dr. Yunfei Gao, from whom I have learnt a lot for my research. I also thank: Dr. Seung Hyun Park, Rafatul Faria, Shehrin Sayed, Ahmed Zeeshan Pervaiz and Dr. Kuntal Roy for their valued feedbacks from time to time.

Last but not least, I would like to dedicate this work to my family: my parents and my wife, who have always shown their love and support.

TABLE OF CONTENTS

	Page
LIST OF FIGURES	vi
LIST OF TABLES	xiv
ABSTRACT	xv
1 INTRODUCTION	1
1.1 This thesis	2
2 “TRANSISTOR-LIKE” SPIN NANO-SWITCHES: THE PHYSICS	5
2.1 CMOS in the view of input-output isolation and gain	5
2.2 Magnetic Tunneling Junction (MTJ) based logic devices	8
2.3 A Write-Read unit with gain	11
2.4 Summary	16
3 MAGNETIC COUPLING AS A WAY OF INPUT-OUTPUT ISOLATION	17
3.1 Motivation and key results	17
3.2 Modeling magnetic coupling fields	23
3.3 Stability considerations for spin current interacting with <i>in-plane</i> dipolar coupled magnets	26
3.3.1 Key parameters describing the dipolar and demagnetization fields	26
3.3.2 Stability condition for in-plane coupled magnets	28
3.3.3 Critical spin current for in-plane coupled magnets	31
3.3.4 Benchmark against experiments	32
3.4 Stability considerations for spin current interacting with <i>PMA</i> dipolar coupled magnets	36
3.4.1 Key parameters describing the dipolar and demagnetization fields	36
3.4.2 Stability condition for PMA coupled magnets	38

	Page
3.4.3 Critical spin current for PMA coupled magnets	39
3.5 Dipolar coupling designs in Spin Switches	39
3.6 Summary	42
4 DIPOLAR FIELDS IN PERPENDICULAR MAGNETIC TUNNEL JUNCTIONS (pMTJ)	43
4.1 Dipolar fields and their effects on Magnetic Tunnel Junctions	43
4.2 General numerical framework for calculating dipolar fields in pMTJs	45
4.2.1 Dipolar fields of a perpendicular magnetic anisotropy (PMA) magnet	45
4.3 Benchmarking the framework	47
4.3.1 Compare to micromagnetic simulation: OOMMF	47
4.3.2 Compare to Tohoku's Experiments	49
4.4 Modeling dipolar fields of full MTJ stacks including Synthetic Antiferromagnetic (SAF) layers	52
4.4.1 Benchmark against experiments	55
4.5 From multi-layer model to three magnet model	58
4.6 Summary	63
5 SPIN SWITCH OSCILLATOR: A NEW APPROACH BASED ON GAIN AND FEEDBACK	64
5.1 Motivation and Key Results	64
5.2 Modeling spin switch oscillator	66
5.2.1 Oscillator: parallel or anti-parallel?	67
5.2.2 Spin Switch Oscillator	70
5.3 SSO frequency: analytical model	72
5.4 SS oscillator with tunable output and power estimations	76
5.5 Summary	79
6 SPIN SWITCHES FOR COMPACT IMPLEMENTATION OF NEURON AND SYNAPSE	80
6.1 Motivation	80
6.2 Spin switch as a basic building block for Neural Network	82

	Page
6.2.1 Modified Spin Switch for neural network	82
6.2.2 Composite spin switch neuron with built-in synapses	84
6.2.3 Training methods for hysteresis activation function by back propagation method	86
6.2.4 Modeling Spin Switches Neural Network(NN)	91
6.3 Spin Switch neural network for Exclusive Or	93
6.4 Spin Switch Neural Network for character recognition	95
6.5 Summary	99
7 “TRANSISTOR-LIKE” SPIN SWITCHES FOR HARDWARE NEURAL NETWORK: AN OUTLOOK	101
7.1 A brief-overview of neural network	101
7.1.1 Deep Belief Network	104
7.2 Implementation of the building block of DBN by transistor-like spin switches	106
7.2.1 Implementation of the stochastic sigmoid function	106
7.3 Stochastic Spin Switch NN implementation for a Bayesian network .	107
7.4 Summary	110
LIST OF REFERENCES	113
A Simple model for GSHE	121
A.1 Drift-diffusion model for GSHE	121
A.2 Spin Hall Effect: spin current and spin voltage	123
B Evaluating dipolar coupling tensor for in-plane magnets	127
C Derivation of the Jacobian of coupled magnets interacting with spin current	131
C.1 In-plane dipolar coupled magnets	131
C.1.1 Stability of one magnet: Sun’s criteria	133
C.1.2 Stability of coupled magnet	134
C.2 PMA dipolar coupled magnets	136
D LLG with thermal noise	138
VITA	140

LIST OF FIGURES

Figure	Page
2.1 (a) CMOS inverter and its input-output relation. (b) The input-output relation can be separated into Write and Read processes. Reprinted by permission from John Wiley and Sons [7], copyright 2015.	6
2.2 CMOS inverter in the view of Read and Write units. Reprinted by permission from John Wiley and Sons [7], copyright 2015.	7
2.3 Write and Read operations in a MTJ device. Reprinted by permission from John Wiley and Sons [7], copyright 2015.	9
2.4 Magnetic coupling (dashed line) between \hat{m} and \hat{m} can be used to achieve input-output isolation between Write and Read units. Reprinted by permission from John Wiley and Sons [7], copyright 2015.	10
2.5 (a) Input-output isolation and gain device: a GSHE for Write and a MTJ device for Read. The magnets in Write and Read are coupled via the magnetic coupling (dipolar coupling). (b) Input-output characteristic. Reprinted by permission from John Wiley and Sons [7], copyright 2015.	12
2.6 The Spin Switch, a transistor-like device having input-output isolation, gain and concatenability. It consists of: GSHE for Write, dual MTJ for Read and magnetic coupling for input-output isolation. (b) The symbolic representation of a spin switch and (c) its input-output characteristic. Reprinted with permission from [17]. Copyright 2012, AIP Publishing LLC.	14
2.7 Spin switch ring oscillator: a proof of input-output isolation and gain. Adapted from [17].	15
3.1 Stability consideration of a system of two Read and Write magnets coupled via dipolar and/or exchange coupling and the Write could interact with spin current \vec{I}_s . The Read and Write magnets could be either: a) in-plane magnets with z, x and y being the easy, hard and out-of-plane axes respectively or b) perpendicular magnetic anisotropy (PMA) magnets with y, z, x being the easy and in-plane axes respectively.	18

- 3.2 Stability consideration of the system in Fig.3.1(a) where Read and Write are in-plane magnets a) Numerical LLG simulations show the stable/unstable regimes of a parallel state $m_z^W m_z^R = 1$ (without spin current) as a function of normalized dipolar coupling strength d_{zz} and d_{xx} (All the fields are normalized to the coercive field of the Read and $H_c^R = 1$). The red line separating the two regimes is the analytical solution of $RT_{51}^{ip} = 0$ in Eq.(3.5). b) LLG simulations of the required critical spin currents (normalized by the critical spin current of the isolated Write magnet i_{sc}^W) to make the anti-parallel state $m_z^W m_z^R = -1$ unstable as a function of d_{xx} for different values of d_{zz} . Here the spin current is polarized in the z direction and the analytical red lines are obtained by solving $RT_{41}^{ip} = 0$ (Eq.(3.7)). The dash blue line is used to determine the smallest $|d_{xx}|$ (for a given d_{zz}) such that above this value, the dipolar coupling is strong enough to make parallel states unstable. Parameters: $h_d^W = h_d^R = 100$; $h_c^R = h_c^W = 1$; $V_{rw} = V_R M_s^R / V_W M_s^W = 0.5$ 29
- 3.3 Numerical LLG simulations show the stable/unstable regimes of a parallel state $m_z^W m_z^R = 1$ as a function of normalized dipolar coupling strength d_{zz} , d_{xx} and d_{yz} . Here all the fields are normalized to the coercive field of the Read H_c^R . The lines separating the stable and unstable regimes are almost independent from the values of d_{yz} . Note that $RT_{51}^{ip} = 0$ is the **analytical** solution of Eq.(3.5) or Eq.(3.36). 30
- 3.4 a) Experimental setups to detect the anti-parallel states between the Read and Write magnets as a function of offsets (distance from center to center in the easy axis of two magnets). They are initially aligned by an external magnetic field, the field is then removed and MFM scan is followed. Read: $120nm \times 100nm \times 10nm$, Write: $600nm \times 140nm \times 10nm$ and they are separated by $15nm$ insulator. b) LLG simulations show the switching of Read magnet m_z^R when offsets are greater than $150nm$. c) The stability phase diagram obtained from determining the sign of RT_{51}^{ip} and the calculations of d_{xx} and d_{zz} as a function of offset (dot line) for the experiment. The system enters the unstable regime when offsets are greater than $150nm$, which also agrees with both numerical and experimental results. 33
- 3.5 The trends of d_{zz} and d_{xx} as a function of offsets can be captured by the charge model mentioned in appendix B. 35

Figure	Page	
3.6	Stability consideration of the system where Read and Write are PMA magnets. (a) LLG simulations and analytical results show the stable/unstable regimes of anti-parallel states $m_z^W m_z^R = -1$ (without spin current) as a function of normalized d_{xx} and $V_{rw} = V_R M_s^R / V_W M_s^W$ (all the fields are normalized to the coercive field of the Read: H_c^R). (b) LLG and analytical results for required critical spin current (normalized by the critical spin current of the isolated Write magnet i_{sc}^W) to make the parallel state $m_y^W m_y^R = 1$ unstable as a function of d_{xx} for different values of V_{rw} . The dash blue line is used to determine smallest $ d_{xx} $ (for a given V_{rw}) such that above this value, the dipolar coupling is strong enough to make anti-parallel state unstable. Here $h_c^R = h_c^W = 1$	37
3.7	(a) Schematic of spin switch device and the dipolar coupling between Write and Read magnets in SS. b) The two components of $D^{RW} = [D]$ as a function of the lengths of Write and Read having fixed aspect ratio $z_b/x_b = z_t/x_t = 1.5$, same thicknesses $y_b = y_t$ and the fixed distance between nearest edges $\delta/y_b = 10$. In all cases, the Read was always put close to the edge of the Write. c) The numerical LLG simulation lines separating the switched (white) and not switched (black) regimes starting from parallel states of $m_z^W m_z^R = 1$ as a function of $H_c^R / \mu_0 M_s^W$. The analytical red lines were obtained by solving $RT_{51}^{ip} = 0$. Here we assumed $H_c^W = H_c^R = 1$ and $M_s^W = M_s^R = 10^6 A/m$ and restricted ourselves to the case where $V_W \leq V_R$	41
4.1	A schematic structure of a full pMTJ stack. Because of the dipolar fields coming from the Ref and SAF layers, the hysteresis of the Free layer magnet does not center at 0 and the strength of the dipolar coupling can be measured via the shift of the hysteresis or H_s . Dipolar field also results in the energy difference for state 1 and 0.	44
4.2	Dipolar fields of a PMA magnet calculated by Eq.(4.3). The fields are strongest near the boundaries of the Ref magnet where $Offset \approx R_{ref}$ and smallest at the center where $Offset = 0$. Note that at $Offset = 0$, the fields can be analytically described by Eq.(4.10). In the simulation, $t = 2nm$, $\delta = 3nm$, $M_s = 10^6 A/m$	47
4.3	a) A schematic setup for the calculating of the dipolar strength (D_{yy}) at Free magnet due to Reference magnet (both have the same diameters). b) D_{yy} could be measured via the shift in hysteresis of the Free magnet due to the dipolar field of Reference magnet. c) OOMMF simulations (reproduced by permission from Professor A. D. Kent at New York University) of D_{yy} as a function of diameters of Ref layer and the distances between Ref and Free layers. d) Macro-spin model calculations of D_{yy} by integrating Eq.(4.11) and using $M_s^{ref} = 0.86 \times 10^6$	48

Figure	Page
4.4 Schematic setups for conventional and stepped structures in Tohoku's experiment [44]. $t_{ref} = 1nm$, $t_{free} = 1.7nm$, $MgO = 1nm$, $M_s^{RL} = 10^6 A/m$	50
4.5 D_{yy} : the strength of dipolar field at FL due to RL, as a function of radius of the RL and for a given size of FL. $t_{ref} = 2nm$, $t_{free} = 2nm$, $\delta = 4nm$, $M_s = 10^6 A/m$	51
4.6 An example of a full pMTJ stack [54] and its schematic representation. The SAF1 and SAF2 layers are $[Co/Pd]$ multi-layers where $N1$ and $N2$ represent the number of repetition of the layers. Note that the SAF1 and SAF2 are separated by the Ru layer whose thickness is well chosen so that the SAF1 and SAF2 to be in the <i>anti-parallel</i> configuration due to the Ruderman-Kittel-Kasuya-Yosida (RKKY) interaction.	53
4.7 $M_s^{Co/Pd}$ of composite $[Co(t_{Co})/Pd(0.9nm)]$ layer. The dotted circle line is the experimental data [63]. The analytical line is obtained by using Eq.(4.12) with $M_s^{Pd-induced} = 210emu/cm^3$	54
4.8 Experimental data on the magnetic properties of composite $[Co/Pt]_n$ as a function of the repetition number n . Reprinted with permission from [60]. Copyright 2010, AIP Publishing LLC.	55
4.9 Comparison between theory and experimental data (Reprinted with permission from [54]. Copyright 2012, AIP Publishing LLC) for the <i>total</i> dipolar fields H_{offset} at the Free layer as a function of the diameters of the stack (H_{offset} was extracted from the shifts of the hysteresis). For theoretical calculation, the black dot curve calculates the dipolar field at FL due to only the RL. Here $M_s(Co/Pt) = M_s(Co/Pd) = 0.4$, $M_s(RL) = 1$ (in the unit of $10^6 A/m$).	56
4.10 The hysteresis shifts as a function of diameters for the structure in Fig.4.9. The theoretical calculations imply that the dipolar fields at Free layer are dominated by the RL and SAF1 layers. Reprinted with permission from [54]. Copyright 2012, AIP Publishing LLC.	57
4.11 A hysteresis of the free layer in an IBM's MTJ stack [64]. The theoretical calculations agree with experiment about the magnitude of the H_{offset} and suggest that the main contribution is from SAF2. Reprinted figure with permission from [64] Copyright 2011 by the American Physical Society.	58
4.12 The complex pMTJ structure can be understood in terms of a system of three magnets. The simulations for the full stack are the same as the simulations in Fig.4.9.	59

Figure	Page
4.13 Numerical (averaging the dipolar field over the FL) and analytical (only dipolar field at the center of FL) simulations for the total field at the FL: a) Geometry factors. The parameters used in the simulations: diameter of the pMTJ stack =55nm, $M_s^{RL} = 10^6 A/m$, $M_s^{SAF1} = M_s^{SAF2} = 0.5 \times 10^6 A/m$, $t_{MgO} = t_{FL} = 1nm$, $t_{Ru} = 0.9nm$. b) Material factors. The parameters used in the simulations: diameter of the pMTJ stack =55nm, $M_s^{RL} = 10^6 A/m$, $M_s^{SAF1} = 0.5 \times 10^6 A/m$, $t_{SAF1} = 5nm$, $t_{MgO} = t_{FL} = 1nm$, $t_{Ru} = 0.9nm$. In both a) and b) the analytical results are obtained via Eq.(4.15) and Eq.(4.14)	61
4.14 Numerical (averaging the dipolar field over the FL) and analytical (only dipolar field at the center of FL) calculations for the critical thickness of SAF2, t_{SAF2}^0 (needed in order to have the total zero dipolar field at FL) as a function of the diameters of the pMTJ for different values of SAF1 thicknesses. Here $M_s^{SAF1} = M_s^{SAF2} = 0.5 \times 10^6 A/m$ and $M_s^{RL} = 10^6 A/m$, $t_{RL} = t_{LF} = t_{MgO} = 1nm$. The analytical results are obtained via Eq.(4.15) and Eq.(4.14).	62
5.1 (a) The schematic and (b) the operational principle of Spin Switch Oscillator (SSO) is similar to the feedback oscillator: for a given voltage V_{in} , input magnet \hat{m}_R gives rise to the charge current $I_{in} \sim m_{R,z} V_{in}$ (z is the easy axis) and the amplified spin current $\vec{I}_{s,W}$ forces the output \hat{m}_W to be parallel to $m_{R,z} \hat{z}$. Because of dipolar coupling, \hat{m}_R wants to anti-parallel to \hat{m}_W . As a result, there are no stable configurations in SSO. When oscillation occurs, both \hat{m}_W and \hat{m}_R will move in-phase (Barkhausen criterion). (c) Detailed structure of spin switch, adapted from [7], and it behaves as an (hysteresis) inverter. Copyright 2014 IEEE. Reprinted, with permission, from [14].	65
5.2 The role of GSHE block in SSO: \hat{m}_W wants to be parallel to \hat{m}_R	68
5.3 The role of dipolar coupling block in SSO: \hat{m}_R and \hat{m}_W want to be in anti-parallel states.	69
5.4 By combining the GSHE and Dipolar block, one can obtain the oscillation of \hat{m}_W and \hat{m}_R magnets. Note that both magnets are moving in-phase.	70
5.5 SSO oscillators for different values of dipolar tensors.(a) Full dipolar tensor as in Eq.(5.5). (b) Only d_{xx} and d_{zz} are presented in the D tensor and (c) Only d_{zz} is presented in the D tensor.	72

Figure	Page
5.6 The frequencies of SSO as a function of the strength of the dipolar coupling for different input voltages V_{in} . As one can see, the frequency does not strongly depend on the voltage as long as it is above threshold. The analytical frequency Eq.(5.17) is in good agreement with the numerical results.	75
5.7 The phase diagram for the frequencies of SS oscillator as a function of dimensions of Write magnet where the gray color is proportional to oscillation amplitude of $m_{r,z}$. In all simulations, we fix the thicknesses of both magnets, $y_t = y_b = 2nm$. While changing the dimensions of Write magnet, we also adjust the dimensions of Read magnet accordingly: $x_t = 0.9x_b, z_t = 0.9z_b$. Copyright 2014 IEEE. Reprinted, with permission, from [14].	77
5.8 SS oscillator with tunable output: it comprises two spin switches, $S1$ and $S2$. Spin switch $S1$ generates the oscillations and $S2$ duplicates the signals of $S1$ given that \hat{m}_W of both $S1$ and $S2$ see the same (oscillating) charge/spin current. The \hat{m}_W of both $S1$ and $S2$ oscillate in-phase and so as the \hat{m}_R of $S2$. The spin switch $S2$ provides a way to independently control the amplitude of oscillating output via the voltage V_{out}	78
5.9 Equivalent circuit for the MTJ at $S2$ unit in Fig.5.8	79
6.1 Standard model for the basic building block of neural networks: A neuron sums the incoming signal x_i with weights w_i and generates the output according to the activation function f as expressed by Eq.(6.1). Spin switches can be used to provide a compact implementation of this building block as evident from comparing Eq.(6.4) with Eq.(6.1). Reprinted with permission from [15]. Copyright 2014, AIP Publishing LLC.	81
6.2 A composite spin switch neuron with built-in synapses. The magnetization of any R unit represents the state of the neuron. The voltages at R units represent the weight of synapses connecting to other neurons. Reprinted with permission from [15]. Copyright 2014, AIP Publishing LLC.	85
6.3 An example of a neural network used to illustrate the idea behind the BP method.	86
6.4 An approximation of hysteresis function ($c = 4$ in Eq.(6.14)) used in the training of hysteretic NN. Reprinted with permission from [15]. Copyright 2014, AIP Publishing LLC.	88

Figure	Page
6.5 A typical spin switch neural network with 3 layers: input, hidden and output layers. $[x]$ is the input vector, $[b_1]$ and $[y]$ are respectively the bias and output of W neurons in the hidden layer. $[b_2]$ and $[O]$ are bias and output vectors of neurons in the output layer respectively. Reprinted with permission from [15]. Copyright 2014, AIP Publishing LLC.	89
6.6 Switching characteristic of Spin Switch (or the activation function): $V = 0$ (solid line) and $V = V_{th}$ (dash line). Reprinted with permission from [15]. Copyright 2014, AIP Publishing LLC.	92
6.7 a) Spin switch neural network implementation for exclusive or gate. Here A and B are inputs. Hidden and output neurons are labeled 1, 2 and 3. b) Simulation results of the dynamics of the network responding to inputs. Here R1, R2 and output are the magnetizations (R units) of neuron 1, 2 and 3 respectively. All the neuron states are randomized initially. We assume all magnets have the same polarization and conductance: $P_i = 0.4, g_i = (1.1k\Omega)^{-1}, \beta = 12$	94
6.8 (a) Implementation of spin switch neural network for character recognition: for simplicity the connections (copper wires) between layers are not shown. (b) Matrices of interconnection weight voltages between input and hidden layers (35×6) and between hidden and output layers (6×3) shown by color scale. Reprinted with permission from [15]. Copyright 2014, AIP Publishing LLC.	96
6.9 (a) LLG simulations for the output layer of the SS neural network described in Fig.6.8(a) in response to eight input characters: $A, B, C \dots H$. Here $R7, R8$ and $R9$ are the magnetizations of magnets in the R units of neuron 7, 8 and 9 respectively. (b) The network still recognizes a letter that is not in the training set (a random defect). We assume all Read units have the same polarization and conductance: $P_i = 0.4, g_i = (1.1k\Omega)^{-1}, \beta = 12$. Reprinted with permission from [15]. Copyright 2014, AIP Publishing LLC.	97

Figure	Page
6.10 Possible way of supplying/storing long term voltage a) The weights (+/- V) of the MTJ stack are provided through the use of tunable complementary floating-gate low dropout voltage regulators. Channel Hot Electron Injection and Fowler-Nordheim tunneling modulated by V_G, V_{tun} can be used to adjust the charge trapped on the floating gate. In turn, those charges adjust the threshold of the nFET/pFET devices giving +/-V at the MTJ of the R unit. b) Each floating-gate may be formed in a bit-addressable array for individual nFET/pFET threshold tuning. c) The spin-switch layer is formed in the metallization above the silicon layer along with the interconnect for the neural network. Reprinted with permission from [15]. Copyright 2014, AIP Publishing LLC.	98
7.1 Unlabeled data or multi-levels of representation of data. The picture could mean: it is a car, a man, a race, etc... with some probabilities.	103
7.2 a) A transistor like device used for hardware implementation of the stochastic neurons having many synapses. b) The probabilistic logistic function for the device where the simulations are done for Spin Switch devices.	111
7.3 a) A simple Bayesian network for inference problem: Rain, Sprinkler and Lawn. The Rain has direct influence on the Sprinkler: when the Rain is ON, the Sprinkler is OFF. Given a wet Lawn, what is the likelihood that it is due to Rain or Sprinkler? b) The proposed hardware implementation of the Bayesian network based on probabilistic SS.	112
A.1 Physical structure for calculating spin current at the FM magnet	124
A.2 Physical structure for calculating spin voltage	125
B.1 The equivalent charge model of a bar magnet.	128

LIST OF TABLES

Table	Page
4.1 Experimental data and simulation results for the shift in hysteresis of the FL (D_{yy}) for both conventional and stepped structures.	51
6.1 Calculating the Weighted sum Z_W and corresponding magnet states at neurons 1,2 and 3 as a function of input magnets for SS XOR problem as in Fig.6.7(a).	95
7.1 Conditional probability tables among Rain, Sprinkler and Lawn. Here 1 presents the ON state while -1 is the OFF state. The tables were obtained by taking average over 10000 trials of LLG simulations for the network in Fig.7.3(b) where the electrical signals are given in Table.7.2	108
7.2 Electrical values used in Fig.7.3(b) to produce the conditional probabilities in table 7.1. The values are normalized by threshold voltage or threshold current.	109
7.3 Inference can be made based on the conditional probabilities values in table 7.1	109

ABSTRACT

Diep, Vinh Quang Ph.D., Purdue University, May 2015. “Transistor-Like” Spin Nano-Switches: Physics and Applications. Major Professor: Professor Supriyo Datta.

Progress in the last two decades has effectively integrated spintronics and nanomagnetism into a single field, creating a new class of spin-based devices that are now being widely used in magnetic memory devices. However, it is not clear if these advances could also be used to build logic devices.

The objective of this thesis is three-fold:

The first is to describe a general paradigm for combining Read and Write units used in memory devices into transistor like nano-switches having input-output isolation and gain. Such switches could be used to build logic circuits without the need of any external circuits or amplification.

The second is to describe an experimentally benchmarked simulation model for designing a concrete implementation of a transistor-like switch based on: Giant Spin Hall Effect(Write), Magnetic Tunnel Junction (Read) and magnetic coupling for isolation. It turns out that the model can also be used to analyze/design stray fields in perpendicular magnetic tunnel junction (pMTJ), an important problem in scaled pMTJ devices.

The third is to discuss the novel features and possible new class of circuits of spin nano-switches. We will first describe a spin switch nano-oscillator based on the standard principle of incorporating feedback into a device with gain. We then discuss how spin nano-switches can be used to implement different types of neural networks such as second generation, third generation and deep belief neural networks.

1. INTRODUCTION

Complementary metal-oxide semiconductor (CMOS) has been very successful from scaling of its dimension over the years, resulting in the performance improvement of the device. However, it has been well accepted that one of the main problems of CMOS logic devices is the heat dissipated [1, 2]. This has led to an intensive search for alternative switches that could potentially provide improvement or add new functionalities to CMOS devices. The industry sponsored Nanoelectronic Research Initiative (NRI) has pioneered the efforts for realizing a better (logic) switch and analyzing different beyond-CMOS devices [3].

On the other hand, there has been great progress in the field of spintronic and nanomagnetic in the past three decades. In particular, there has been great understanding in Reading information from a magnet and Writing information into a magnet. The question is: can this understanding be used to build logic devices?

Note that a logic device is different from a memory device in the sense that it could drive another one and this requires gain, directionality and input-output isolation. Therefore, the next question is that: how spintronic and nanomagnetic based devices could be integrated into transistor-like switches that can perform logic applications without the need of any amplification circuits?

To build logic devices based on spins and magnets, we have two broad options:

- design the devices where gain is provided by CMOS or
- design the devices that have gain.

In this thesis, we will discuss the latter option.

For conventional Boolean logic applications, we should mention that spintronic-based devices basing on established technology, at the moment, are inferior to CMOS transistors [4–7] in terms of energy and delay. However, this could be changed as new

materials and phenomena are discovered (see for example [8–13]) to improve Read and Write mechanisms in magnet-based switches. Until then, in this thesis, we want to establish that spintronic-based switches could still look attractive because of their features (non-volatility, reconfigurability and compactness) that could be very useful in new circuits such as hardware implementation of neural networks.

1.1 This thesis

The outline of the thesis is summarized as in the following:

- In Chapter 2, we argue that key properties of logic devices are input-output isolation and gain. For that reason, a simple combination of Read and Write devices will not make a logic switch. We then introduce one way to integrate (spintronic and nanomagnetic based) Read and Write devices to build the so-called transistor-like spin switch. This work was published in a book chapter [7].
- In Chapter 3, we focus on magnetic coupling (dipolar and/or exchange interaction) which is a way to achieve input-output isolation in transistor-like switches. In particular, we describe in detail the modeling/understanding of the exchange and dipolar coupling between either in-plane or perpendicular magnetic anisotropy magnets. The results are benchmarked against experiments and are in preparation for publication.
- It turns out that dipolar coupling plays an important role in analyzing/designing perpendicular magnetic tunnel junctions (pMTJ) which are important devices for memory applications. Therefore, in Chapter 4, we describe in detail the modeling of dipolar fields in pMTJ and the results are benchmarked against micro-magnetic simulations as well as experimental data. The work is in preparation for publication.
- Since devices with gain and directionality can be used to build oscillators, in Chapter 5, we describe a spin switch oscillator based on the standard principle of

incorporating feedback into a device with gain. Unlike the present-day state-of-the-art spin transfer nano oscillators (STNO) based on the delicate balancing of magnetic fields and spin currents, this spin switch oscillator (SSO) should exhibit high tunable output power without the need of external magnetic fields. On the other hand, the SSO is an initial step towards the implementation of spiking neurons or the third generation of neural network. This work was published in a conference [14].

- In Chapter 6, we explore the non-Boolean logic applications of transistor-like spin switches. In particular, it describes the possibility of hardware implementation of neural networks using a spin switch as its basic building block (neurons and synapses). Here, we will show that a **single** spin switch neuron is capable of performing summation, multiplication and activation function, which normally require extra circuitry in other hardware implementations. The weights of the neurons are conveniently adjusted through analog voltages that can be stored in a non-volatile manner. Furthermore, the SS neurons can have many fan-outs (synapses) which enable the realization of the neural networks. The SS neural network can be constructed with purely passive interconnects without intervening clocks or amplifiers. This work was published in a journal [15].
- Chapter 7 is a vision for the future work where we discuss the possible extensions of spin based neural network discussed in Chapter 6. We discuss the implementation of **stochastic** neuron, by a single transistor-like spin nano switch, for possible use in deep belief networks used for data mining and machine learning applications. To our knowledge, this is the first proposal for a hardware implementation of such a neuron within a single device. We specifically demonstrate the operation of a *spin based* Bayesian neural network designed for inference problems by using a standard simulation model based on coupled Landau-Lifshitz-Gilbert (LLG) equations, one for each magnet in the network. This work is in preparation for publication.

Overall, in the last three chapters, this thesis tries to establish that a **single** transistor-like spin nano-switch could be used to implement different types of neural networks: second generation (Chapter 6), third generation or spiking neuron (Chapter 5) and deep belief network (Chapter 7).

2. “TRANSISTOR-LIKE” SPIN NANO-SWITCHES: THE PHYSICS

Most of the material in this chapter have been extracted from the following book chapter: ‘What Constitutes a Nanoswitch? A Perspective’, Supriyo Datta, Vinh Diep and Behtash Behin-Aein. *Emerging Nanoelectronic Devices*, Editors: An Chen, James Hutchby, Victor Zhirnov and George Bourianoff, John Wiley & Sons (2015).

Our objective in this chapter is to discuss the possibility of constructing transistor-like switches based on spintronic and nanomagnetic based devices. To do so, we first would like to review the complementary metal oxide semiconductor (CMOS) transistors which are widely used as logic devices and identify key properties allowing CMOS inverter to perform logic applications without the need of any amplification circuits, namely: input-output isolation and gain. We then argue that CMOS can also be viewed as Read and Write processes understood in memory devices.

Next we will discuss how Read (R) and Write (W) units widely used in magnetic memory devices can be integrated into a single device having input-output isolation. We will show that a simple combination of MTJ devices could achieve input-output isolation (for example by using the dipolar coupling between magnets) but it is not enough because of no gain. The Giant Spin Hall Effect (GSHE) discovered recently [16] could be used to implement the Write unit and provide gain, leading to the spin switch devices introduced by Datta et al. [17].

2.1 CMOS in the view of input-output isolation and gain

Fig.2.1(a) shows a schematic structure of a CMOS inverter and its input-output relation. The inverter is made of two types of transistors: a NMOS and a PMOS

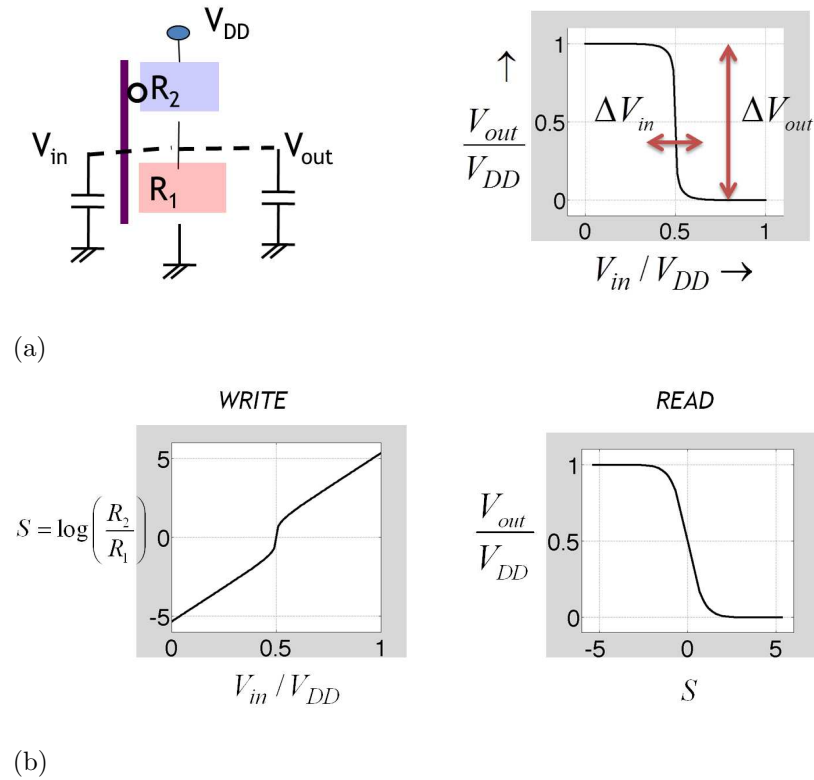


Fig. 2.1. (a) CMOS inverter and its input-output relation. (b) The input-output relation can be separated into Write and Read processes. Reprinted by permission from John Wiley and Sons [7], copyright 2015.

which are represented by resistors R_1 and R_2 respectively. When V_{in} is high, the NMOS is ON (R_1 is low) and the PMOS is OFF (R_2 is high), which results in a low output voltage since V_{out} is now connected to the ground. On the other hand, when V_{in} is low, R_1 is high, R_2 is low and the output voltage will be close to the V_{DD} . The input-output characteristic of the CMOS inverter is shown in Fig.2.1(a).

Now, we would like to argue that the above operation of a CMOS can also be broken into two processes: a Write and a Read process indicated in Fig.2.1(b).

In the Write process, input voltage V_{in} will determine the state of the inverter by controlling the resistances R_1 and R_2 as mentioned above. Instead of working with R_1 and R_2 , we can then define the *state* of the inverter as:

$$S = \log\left(\frac{R_2}{R_1}\right)$$

Therefore, we can say that, in the Write process, V_{in} will set the state S of the inverter.

In the Read process, the output voltage can be easily obtained when R_1 and R_2 are known:

$$V_{out} = V_{DD} \frac{R_1}{R_1 + R_2}$$

Again, instead of working with R_1 and R_2 , we can plot the dependence of output voltage on the state S as shown in Fig.2.1(b).

Some of the key properties:

- Input-output isolation: the read and write processes do not interfere with each other. Namely, the state S of CMOS is entirely controlled by the V_{in} and not by the V_{DD} . On the other hand, V_{out} does depend only on V_{DD} .
- Input-output asymmetry or gain = $\Delta V_{out}/\Delta V_{in} > 1$, namely the swing of output voltage can be greater than the swing of input voltage required to switch the

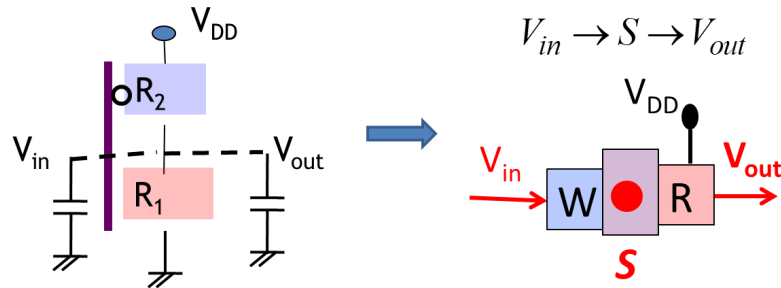


Fig. 2.2. CMOS inverter in the view of Read and Write units. Reprinted by permission from John Wiley and Sons [7], copyright 2015.

inverter. In other words, input V_{in} is much more efficient in controlling the state S than the output is. This makes CMOS very different from often discussed nanoscale devices whose gains are usually $\ll 1$.

For the above reasons, CMOS inverter operation can be schematically viewed as read and write processes shown in Fig.2.2. The input voltage V_{in} will write the information onto the state S of the inverter. Depending on the internal state (read process) S , the supply voltage V_{DD} of the inverter will produce the output voltage V_{out} . The center dot of the schematic figure represents the fact that, Write is isolated from the Read process.

If the CMOS inverter can be viewed as Write and Read processes, then what is the possibility of designing transistor-like devices based on Read and Write units widely used in magnetic memory devices such as MTJ?

2.2 Magnetic Tunneling Junction (MTJ) based logic devices

MTJ has been an important and widely used device for Reading and Writing information in magnetic devices (see for example [18]). So far we have argued that CMOS inverter can also be viewed as an integrated Read and Write unit. If so, the immediate question is that: can we build a switch based on MTJ devices having ‘transistor-like’ characteristic? Before answering the question, let us remind how Read and Write are operated in an MTJ-based device. Fig.2.3 shows the basic Write and Read operations in a MTJ. For Writing, a charge current I_{in} passing through the fixed layer \hat{M} will result in a spin current acting on the free layer \hat{m} magnet. If the spin current is above a critical value, it can switch the free magnet \hat{m} via the so-called spin transfer torque mechanism [19–22]. Reading the direction (information) of the free layer can be achieved via the tunneling magneto-resistance (TMR) effect [23–25] where the resistance R of the MTJ is determined depending on the relative orientation between the fixed and the free layers. Likewise, Reading the information in the free magnet \hat{m} can be translated into the output current I_{out} :

$$I_{out} = \frac{V}{R + R_L} \quad (2.1)$$

where V is the supply voltage and R_L is a fixed load resistance.

A W-R unit with input-output isolation: We can now design a switching having input-output isolation by simply combining a Read and Write MTJ unit. Before going to the details, we note that our MTJ is a current switching device and information is stored in the direction of \hat{m} . Therefore, we would like to design a switch that takes the input current I_{in} , determines the state \hat{m} of the magnet (information) and produces an output current I_{out} depending on the state of \hat{m} :

$$I_{in} \rightarrow \hat{m} \rightarrow I_{out} \quad (2.2)$$

Fig.2.4 shows one example of a conceptual switch based on MTJ devices having input-output isolation. The switch composes of two isolated MTJ devices serving as Write and Read units. The free layer magnets (\hat{m}) in each MTJ couple to each other via magnetic coupling (dipolar or exchange) in such a way that whenever the free

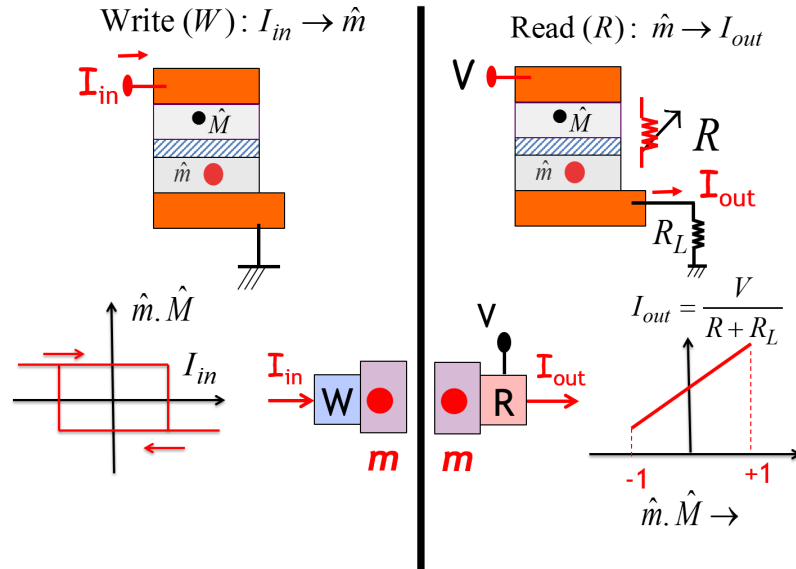


Fig. 2.3. Write and Read operations in a MTJ device. Reprinted by permission from John Wiley and Sons [7], copyright 2015.

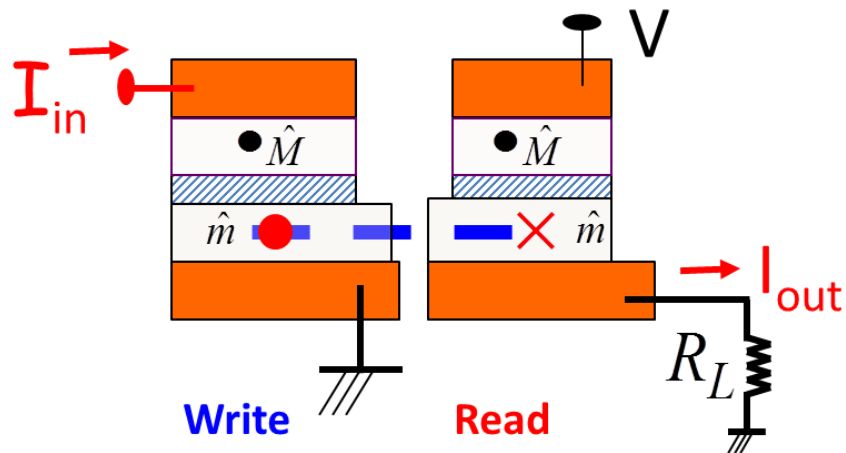


Fig. 2.4. Magnetic coupling (dashed line) between \hat{m} and \hat{m} can be used to achieve input-output isolation between Write and Read units. Reprinted by permission from John Wiley and Sons [7], copyright 2015.

magnet in the Write unit is switched, the other one in the Read unit will follow. This switch satisfies the fact that the Write and Read are electrically isolated, hence the input-output isolation is achieved.

Will the device show gain? The problem is that, output current of the device in Fig.2.4 is not enough to drive the next stage. At first, it seems trivial to say that one can increase the output current simply by increasing the output voltage in Eq.(2.1). However, if we apply a large voltage to the Read unit, the charge current at the Read MTJ also gives rise to a large spin current and switches the free magnet at Read. As a result, the magnet \hat{m} , which is supposed to be controlled **entirely** by the input current in the Write unit, now can also be controlled by the Read current. This violates the input-output isolation criteria hence this is not acceptable for logic devices.

Therefore, we would like to design a switch so that the state of the device is greatly controlled by the Writing and not by the Reading process. The spin switch proposed in 2012 [17] is one example where it showed that Giant Spin Hall Effect (GSHE) [16]

material could be used to design the Write units so that overall W-R device could have gain.

2.3 A Write-Read unit with gain

Now we would like to discuss one example of W-R unit shown in Fig.2.5 that exhibits gain. Unlike the previous structure in Fig.2.4, GSHE material is used to implement the Write unit. Why does the device shown in Fig.2.5 show gain and allow the use of relatively low voltage to switch the next unit? To answer this question, we need to understand why GSHE does offer gain.

In GSHE materials [13, 26] such as Ta, Tungsten, Platinum... an input charge current I_{in} flowing in the GSHE will result in a spin current:

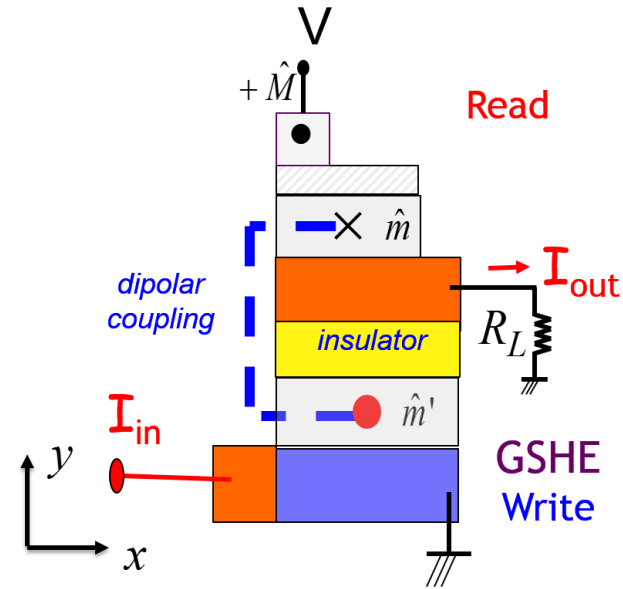
$$\vec{I}_s = \theta_H \frac{A_s}{A} I_{in} \hat{z} = \beta I_{in} \hat{z} \quad (2.3)$$

where A and A_s are the areas of charge current and spin current (or areas of magnet \hat{m}') respectively. θ_H is the Hall angle. The above equation can be derived from (see appendix A.1 for the derivation):

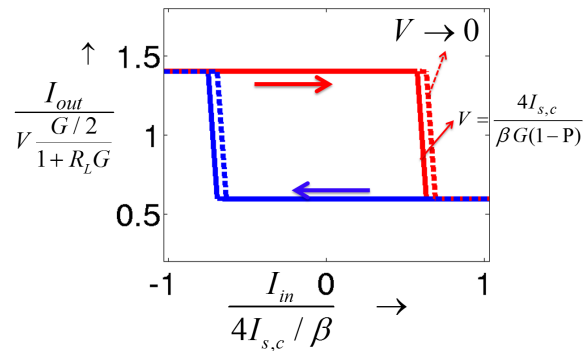
$$J_s = \theta_H J_c \left(1 - \text{sech}(t/\lambda_{sf}) \right) \approx \theta_H J_c \quad (2.4)$$

with the assumption that the spin flip scattering length λ_{sf} is much smaller than the thickness t of the material. The equation implies that a charge current density J_c will give rise to a spin current density J_s in the GSHE material. On top of that, spin current $I_s = J_s A_s$ can exceed the charge current $I_c = J_c A$ if one could design $A_s > A$.

Gain of the device: by definition, is related to the fact that the swing of output current can be greater than the swing of input current. For our device shown in Fig.2.5, we are going to show that gain of the device is ultimately related to the gain (β) in the spin current of the GSHE material (Eq.(2.3)). First, the output charge current is proportional to the applied voltage V as in Eq.(2.1). Second, from Eq.(2.3), the spin current is $I_{s,out} = \beta I_{out}$ where the β factor could be designed to be > 1 . This



(a)



(b)

Fig. 2.5. (a) Input-output isolation and gain device: a GSHE for Write and a MTJ device for Read. The magnets in Write and Read are coupled via the magnetic coupling (dipolar coupling). (b) Input-output characteristic. Reprinted by permission from John Wiley and Sons [7], copyright 2015.

natural amplification β factor allows one to use relatively low voltage to switch the next unit.

Fig.2.5(b) shows the input-output characteristic of a SS obtained from solving coupled Landau-Lifshitz-Gilbert (LLG) equations for a system of two dipolar coupled magnets W/R interacting with spin current. The details of the simulation can be found in [17]. When the voltage $V \rightarrow 0$, the input-output characteristic is symmetric about the origin but it shifts to the left as V increases. This can be understood by the fact that voltage V will also result in a spin current I_s in the Read unit and this bias spin current causes the asymmetric input-output. The gain of the device can be defined as [7]:

$$\text{Gain} \equiv \frac{\Delta I_{out}}{\Delta I_{in}} \approx \frac{VG/2}{1 + R_L G} \frac{\beta}{2I_{sc}} \quad (2.5)$$

where $G = G_{AP} + G_P$ is the total conductance of the MTJ and I_{sc} is the critical spin current required to switch the W magnet. As one can see, with a relative small voltage V , the device still has gain > 1 since the GSHE allows us to have large β .

Concatenability: Although the device in Fig.2.5(a) satisfies the requirements of input-output isolation and gain, it is not ‘concatenable’. The output current I_{out} of the device is always positive for a positive voltage V . However, the input current to the next unit requires both negative and positive currents shown in Fig.2.5(b). There are two broad options that one can modify the device to be concatenated:

- modify the Write unit so that it can only take input positive currents to switch magnet, or
- modify the Read unit so that it produces both positive and negative output currents.

Fig.2.6(a) shows one possible design proposed in Ref. [17] addressing the concatenability issue based on the latter option. It is called spin switch and it modifies the Read unit so that the output current I_{out} can have both positive and negative values. The Read unit now has two MTJ stacks supplied by two equal but opposite voltages, and the fixed magnets in the MTJ are arranged in the opposite directions (\hat{M} and

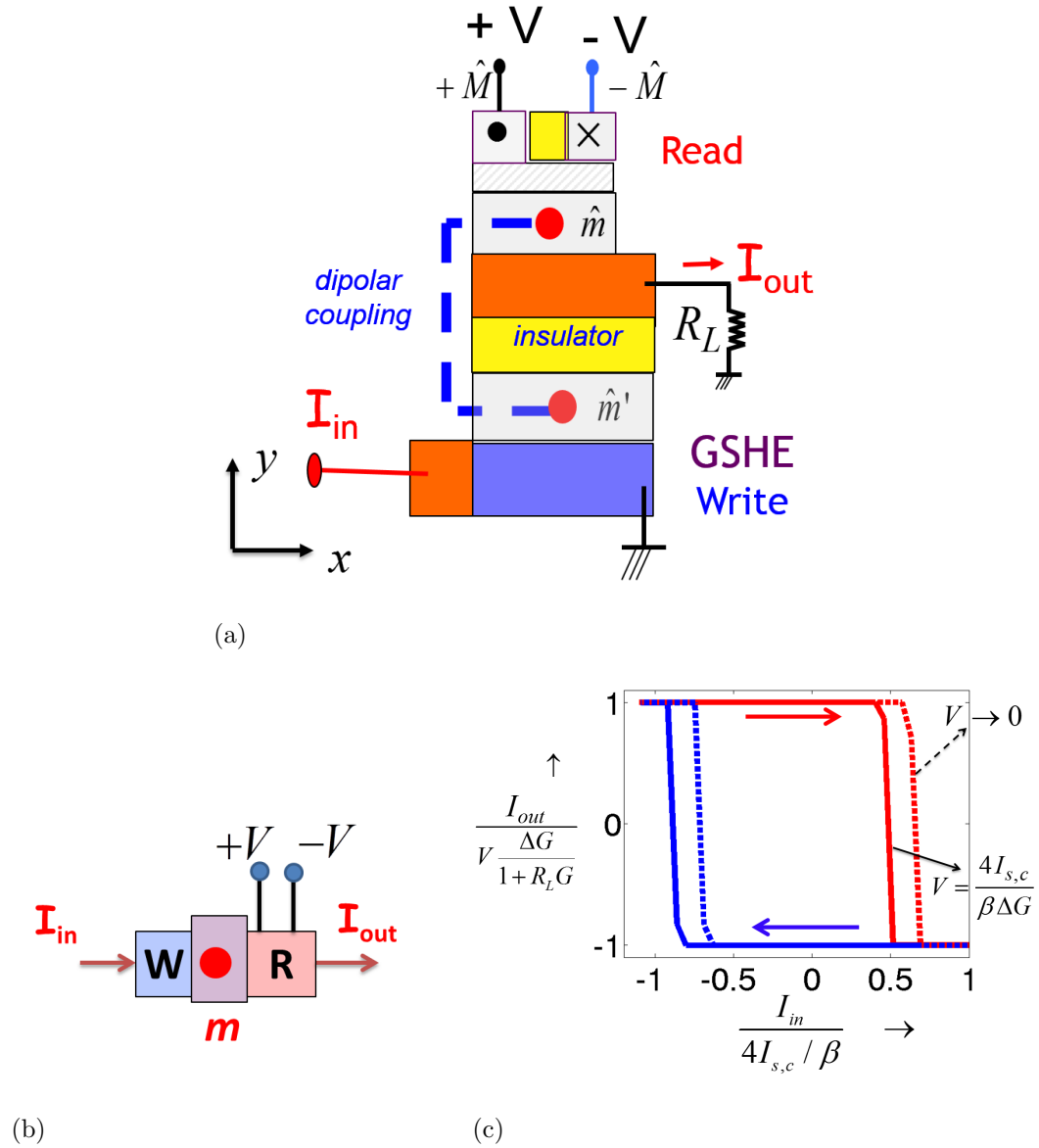


Fig. 2.6. The Spin Switch, a transistor-like device having input-output isolation, gain and concatenability. It consists of: GSHE for Write, dual MTJ for Read and magnetic coupling for input-output isolation. (b) The symbolic representation of a spin switch and (c) its input-output characteristic. Reprinted with permission from [17]. Copyright 2012, AIP Publishing LLC.

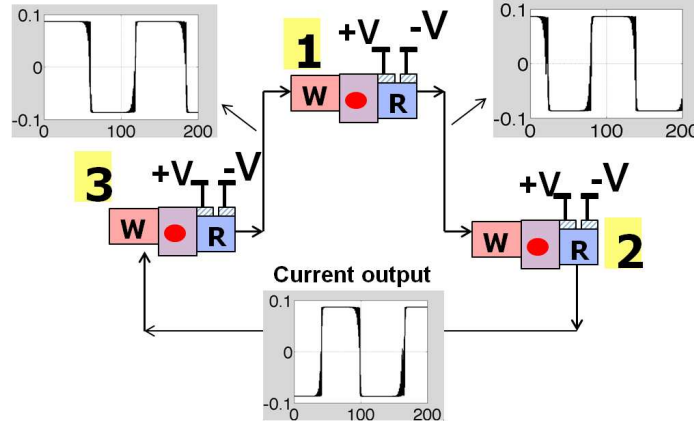


Fig. 2.7. Spin switch ring oscillator: a proof of input-output isolation and gain. Adapted from [17].

$-\hat{M}$) so that the resistances of two MTJ are not the same for a given direction of the free magnet \hat{m} . For this setup, the output current can be easily derived as [17]:

$$I_{out} = \frac{VGPm_z}{1 + R_LG} \quad (2.6)$$

where $P = \Delta G/G$ is the polarization of the MTJ. Therefore, when m_z of the Read magnet changes its sign, so does the output current.

Ring oscillator: So far, our spin switches are designed to have transistor-like characteristics such as input-output isolation, gain and concatenability. One way to test its transistor-like properties is to build ring oscillators without any external circuits. For example, one can connect three spin switch devices (labeled 1, 2 and 3) as shown in Fig.2.7 to form the ring oscillator. From the Eq.(2.1), one can see that the output current of one SS will be proportional to the m_z^R at the R unit of that SS. Therefore, with above threshold voltages V , unit 1 wants $m_z^W(2)$ of Write magnet in unit 2 to be parallel to $m_z^R(1)$ of R magnet in the unit 1. Since $m_z^W(2) = -m_z^R(2)$ due to the magnetic coupling, the final result is that $m_z^R(2)$ wants to be anti-parallel to $m_z^R(1)$ of the unit 1. Similarly, $m_z^R(3)$ wants to be anti-parallel to $m_z^R(2)$ of the unit 2 and so on. The net result is that there is no stable configuration in the ring oscillator and this is confirmed by the simulations shown in Fig.2.7.

The ring oscillator example concludes that our spin switch devices have transistor like characteristics such as input-output isolation, gain and concatenability.

2.4 Summary

In this chapter, we have discussed one possibility of constructing transistor-like switches having input-output isolation and gain based on spintronic and nanomagnetic based devices. We first review the complementary metal oxide semiconductor (CMOS) transistors which are widely used as logic devices, and argue that CMOS can also be viewed as Read and Write processes understood in memory devices. In addition, the input-output isolation and gain are key points allowing CMOS inverter to perform logic applications without the need of any amplification circuits.

Next we discuss how Read (TMR effect) unit and Write (spin transfer torque mechanism) unit widely used in magnetic memory devices (MTJ) can be integrated into a single device having input-output isolation (for example by using the dipolar coupling between magnets). However, we argue that a simple combination of R and W would not provide gain and suggest that Giant Spin Hall Effect (GSHE) could be one of the solutions for gain.

Finally, we would like to mention that, by no means, the GSHE material and MTJ device are the only possibilities of integrating Write and Read units into transistor-like devices having input-output isolation and gain. Examples include all spin logic [27, 28] and m-logic devices [29]. On top of that, new materials and phenomena have been discovered such as topological insulators [8–10], voltage controlled magnetic anisotropy [12, 30], multiferroic [31]... which could be used to implement Read and Write units in the transistor-like spin switch devices.

The matlab codes used to generate the figures can be found at:

<https://drive.google.com/open?id=0B9ggzdMPbfz4VDdld0xPc19ldm8&authuser=0>

3. MAGNETIC COUPLING AS A WAY OF INPUT-OUTPUT ISOLATION

The contents of this chapter would be submitted for review, ‘Stability conditions for spin current interacting with magnetic coupled magnets’, V. Diep, F. Rafatul, C. C. Lin, A. Verma, J. Appenzeller , Z. Chen and S. Datta.

3.1 Motivation and key results

In Chapter 2, we mentioned that one of the key properties of the transistor-like devices is the input-output isolation. In magnetic based devices, this could be archived via the dipolar coupling as in SS [17] or by exchange coupling between magnets [29].

Magnetic coupling between magnets has been investigated in various contexts such as: Magnetic Quantum Cellular Automata, Nanomagnetic Logic (see for example [32–36]), in spring magnetic exchange coupling [37–40]. Recently, dipolar coupling between magnets has been used as a mechanism for transmitting information from the input to the output while maintaining complete electrical isolation between them. This is a very new concept which is only beginning to be tested experimentally. Examples include: spin hall effect clocking of nanomagnetic logics [41] or the dipolar coupling in spin switch (SS) devices [17] which are transistor like devices having input-output isolation and gain.

Here the concept of magnetic coupling used for input-output isolation is new in the sense that it is a system of coupled magnets **interacting with spin current**. Therefore, our objective in this chapter is to present a numerical and analytical macro-spin model (at zero temperature) for a system of Read (R) and Write (W) magnets having magnetic interaction (dipolar and/or exchange interaction) and both of them

could interact with spin current \vec{I}_s . The magnets could be either in-plane magnets as in Fig.3.1(a) or perpendicular magnetic anisotropy (PMA) magnets as in Fig.3.1(b). We first establish our results for dipolar coupled in-plane magnets and then for PMA magnets. Next we discuss exchange interaction in our model. One of the important points is that the magnetic coupling in our model can be easily coupled to spin transport to study the dynamics of the system.

While our numerical model is general, our analytical model mainly focuses on the stability of the system for coupled magnets stacked vertically (along their smallest thicknesses) and the stability criteria are obtained directly from the LLG equations through a Jacobian analysis. Our key analytical results are the expressions for:

1. The stability condition of magnetic coupled Read and Write magnets without spin current and
2. The required critical spin current to make coupled magnets unstable. The latter is essentially an extension of Sun's criteria [21] for coupled magnets.

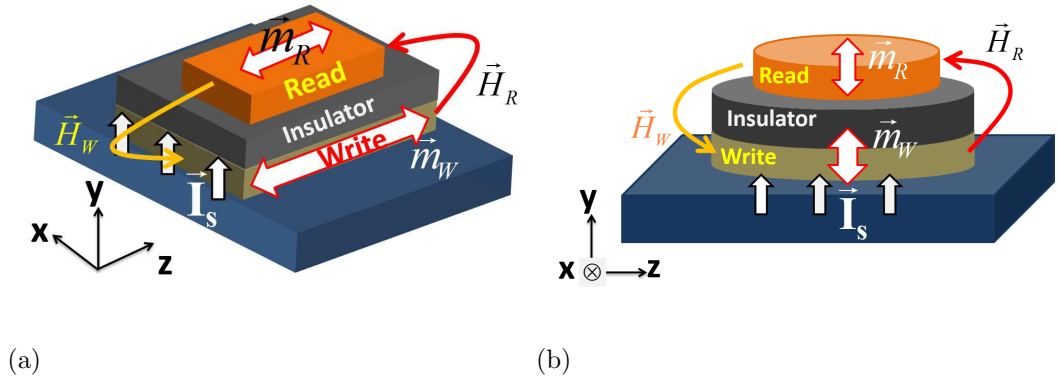


Fig. 3.1. Stability consideration of a system of two Read and Write magnets coupled via dipolar and/or exchange coupling and the Write could interact with spin current \vec{I}_s . The Read and Write magnets could be either: a) in-plane magnets with z, x and y being the easy, hard and out-of-plane axes respectively or b) perpendicular magnetic anisotropy (PMA) magnets with y, z, x being the easy and in-plane axes respectively.

In general, our analytical results are benchmarked against the LLG numerical simulations for both in-plane and PMA magnets. In addition, for in-plane magnets, the switching criteria due to dipolar coupling are also in agreement with our experiments.

For systems of spin current interacting with coupled magnets as in Fig.3.1(a), we use the standard coupled Landau-Lifshitz-Gilbert (LLG) equations to describe the dynamics of the system:

$$\begin{aligned}
(1 + \alpha_W^2) \frac{d\hat{m}_W}{dt} &= -\gamma \hat{m}_W \times \vec{H}_W(\hat{m}_W, \hat{m}_R) - \alpha_W \gamma \hat{m}_W \times \hat{m}_W \times \vec{H}_W(\hat{m}_W, \hat{m}_R) \\
&\quad - \hat{m}_W \times \hat{m}_W \times \frac{\hat{I}_s}{qM_s^W V_W} + \alpha_W \hat{m}_W \times \frac{\hat{I}_s}{qM_s^W V_W} \\
(1 + \alpha_R^2) \frac{d\hat{m}_R}{dt} &= -\gamma \hat{m}_R \times \vec{H}_R(\hat{m}_W, \hat{m}_R) - \alpha_R \gamma \hat{m}_R \times \hat{m}_R \times \vec{H}_R(\hat{m}_W, \hat{m}_R)
\end{aligned} \tag{3.1}$$

where $\vec{H}_W(\hat{m}_W, \hat{m}_R)$ and $\vec{H}_R(\hat{m}_W, \hat{m}_R)$ are the total fields (internal and dipolar fields) at W and R magnets respectively. In the next sections, we are trying to establish:

- General model to evaluate the magnetic coupling between W and R magnets.
- Identify the key parameters governing the magnetic coupling between magnets and derive the analytical expressions for the stability of the system. The stability criteria are obtained directly from the LLG equations through a Jacobian analysis.

We will argue that the dipolar and exchange interactions can be treated on an equal footing. Therefore, from now on, we mainly present our analytical results for the dipolar coupling between magnets.

Key results for in-plane coupled magnets

For dipolar coupled magnets, we will argue that the key parameters describing in-plane coupled W/R magnets stacking vertically are the following:

$$H_W = \begin{bmatrix} 0 & 0 & 0 \\ 0 & -H_d^W & 0 \\ 0 & 0 & H_c^W \end{bmatrix} \begin{bmatrix} m_x^W \\ m_y^W \\ m_z^W \end{bmatrix} + \frac{V_R}{V_W} M_s^R \begin{bmatrix} D_{xx} & 0 & 0 \\ 0 & D_{yy} & D_{yz} \\ 0 & D_{yz} & D_{zz} \end{bmatrix} \begin{bmatrix} m_x^R \\ m_y^R \\ m_z^R \end{bmatrix} \quad (3.2)$$

$$H_R = \begin{bmatrix} 0 & 0 & 0 \\ 0 & -H_d^R & 0 \\ 0 & 0 & H_c^R \end{bmatrix} \begin{bmatrix} m_x^R \\ m_y^R \\ m_z^R \end{bmatrix} + M_s^W \begin{bmatrix} D_{xx} & 0 & 0 \\ 0 & D_{yy} & D_{yz} \\ 0 & D_{yz} & D_{zz} \end{bmatrix} \begin{bmatrix} m_x^W \\ m_y^W \\ m_z^W \end{bmatrix} \quad (3.3)$$

where V_R and V_W are the volumes of Read and Write magnets respectively. H_d and H_c are the demagnetization and coercive fields respectively of the magnets. D_{ij} represents the strength of the dipolar field at Read magnet in the j direction due to the Write magnet pointing in the i direction. For the analytical results, we further assume that the demagnetization field is the dominant field, e.g. $H_d \gg D_{ij}M_s, H_c$, compared to the dipolar and switching fields of the magnets. Therefore, we can approximate $D_{yy} = 0$ in the calculation. On top of that, basing on LLG simulations, we will argue that D_{yz} has a minor role in determining the stability and hence we can approximate $D_{yz} = 0$. This can be justified by noting that the dynamics of the system are basic in-plane $m_y^{W,R} \approx 0$ due to a very large H_d terms.

By analyzing the eigenvalues of Jacobian at fix points of the coupled LLG equations (Eq.(3.1)), we derive the general stability criteria of the system (appendix C). In particular, we derive the Routh's table for the system and in general, one can numerically evaluate the signs of elements of the first column of Routh's table to determine the stability of $\{m_z^W, m_z^R\}$ state. In some cases, however, if we assume the damping coefficients ($\alpha_R = \alpha_W = \alpha \ll 1$) and demagnetization fields $H_d^R = H_d^W = H_d \gg D_{ij}M_s, H_c^R, H_c^W$, the stability conditions (in terms of the normalized fields $h_d^{W,R} = H_d^{W,R}/H_c^R, h_c = 1, h_c^W = H_c^W/H_c^R, d_{ij} = D_{ij}M_s^W/H_c^R$, and $V_{rw} = M_s^R V_R/M_s^W V_W$) are:

- Stability of dipolar coupled magnets without spin current ($\vec{i}_s = 0$): the state $\{m_z^W, m_z^R\}$ is unstable when either $RT_{31}^{ip} < 0$ or $RT_{51}^{ip} < 0$ where:

$$RT_{31}^{ip} = h_c^W + 1 + m_z^R m_z^W (1 + V_{rw} d_{zz}) \quad (3.4)$$

$$RT_{51}^{ip} = (1 + m_z^R m_z^W d_{zz})(h_c^W + m_z^R m_z^W V_{rw} d_{zz}) - V_{rw} d_{xx}^2 \quad (3.5)$$

- In *equilibrium*, an anti-parallel *stable* state, $m_z^W m_z^R = -1$, could be unstable in the presence of a spin current $\vec{i}_s = i_s \hat{z}$. If we assume, $h_d^W = h_d^R = h_d$, $\alpha_W = \alpha_R = \alpha$), then system will be unstable when either $RT_{21}^{ip} < 0$ or $RT_{41}^{ip} < 0$

$$RT_{21}^{ip} = m_z^W i_s + 2i_{sc}^W + \alpha m_z^W m_z^R (1 + V_{rw}) d_{zz} \quad (3.6)$$

$$\begin{aligned} RT_{41}^{ip} = & 4V_{rw} \left[\alpha m_z^W i_s (h_z^R - h_z^W) + (m_z^W i_s + 2I_{sc}^W)^2 \right] d_{xx}^2 \\ & + \alpha (m_z^W i_s + I_{sc}^W) \left[(h_z^R - h_z^W)^2 h_d \right. \\ & \left. + 4(m_z^W i_s + I_{sc}^W) [(m_z^W i_s + I_{sc}^W) h_z^R + I_{sc}^W h_z^W] \right] \end{aligned} \quad (3.7)$$

where

$$h_z^W = h_c^W + V_{rw} d_{zz} m_z^W m_z^R$$

$$h_z^R = h_c^R + d_{zz} m_z^W m_z^R$$

and the normalized spin current is defined as:

$$i_s = \frac{\vec{I}_s \cdot \hat{z}}{(2q/\hbar)\mu_0 H_c^R M_s^W V_W}$$

and $i_{sc}^W = \alpha_W (h_c^W + h_d^W/2)$ is the normalized critical spin current of an isolated Write magnet and it is one of Sun's criteria [21].

Key results for PMA coupled magnets

For the case of PMA magnets as in Fig.3.1(b), we will argue that the key parameters describing dipolar fields of coupled W/R magnet stacked vertically are the following:

$$\begin{aligned}
H_R &= \begin{bmatrix} 0 & 0 & 0 \\ 0 & H_c^R & 0 \\ 0 & 0 & 0 \end{bmatrix} \begin{bmatrix} m_x^R \\ m_y^R \\ m_z^R \end{bmatrix} + M_s^W \begin{bmatrix} D_{xx} & 0 & 0 \\ 0 & -2D_{xx} & 0 \\ 0 & 0 & D_{xx} \end{bmatrix} \begin{bmatrix} m_x^W \\ m_y^W \\ m_z^W \end{bmatrix} \\
H_W &= \begin{bmatrix} 0 & 0 & 0 \\ 0 & H_c^W & 0 \\ 0 & 0 & 0 \end{bmatrix} \begin{bmatrix} m_x^W \\ m_y^W \\ m_z^W \end{bmatrix} + \frac{V_R}{V_W} M_s^R \begin{bmatrix} D_{xx} & 0 & 0 \\ 0 & -2D_{xx} & 0 \\ 0 & 0 & D_{xx} \end{bmatrix} \begin{bmatrix} m_x^R \\ m_y^R \\ m_z^R \end{bmatrix}
\end{aligned} \tag{3.8}$$

Similar to the in-plane magnets, by analyzing the eigenvalues of Jacobian at fix points of the coupled LLG equations, we derive the general stability criteria of the system (appendix C). In general, one can numerically evaluate the signs of elements of the first column of Routh's table to determine the stability of $\{m_y^W, m_y^R\}$ state. However, when the Read and Write units having the same damping coefficient ($\alpha_R = \alpha_W = \alpha \ll 1$), the stability conditions are:

- Stability of dipolar coupled magnets without spin current: the state $\{m_z^W, m_z^R\}$ is unstable when $RT_{51}^{ip} < 0$ where:

$$\begin{aligned}
RT_{51}^{PMA} &= [(1 - 2m_y^R m_y^W d_{xx}) + (h_c^W - 2m_y^R m_y^W V_{rw} d_{xx})] \\
&\quad \times [(1 - 2m_y^R m_y^W d_{xx}) (h_c^W - 2m_y^R m_y^W V_{rw} d_{xx}) - V_{rw} d_{xx}^2]
\end{aligned} \tag{3.9}$$

- In *equilibrium*, a parallel *stable* state, $m_y^W m_y^R = 1$, could be unstable in the presence of a spin current $\vec{i}_s = i_s \hat{y}$. In particular, the system will be unstable when $RT_{41}^{PMA} < 0$:

$$\begin{aligned}
RT_{41}^{PMA} &= -4V_{rw}^2 \alpha^2 d_{xx}^4 + \alpha (h_{yr} - h_{yw})^2 \left[h_{yr} (m_y^W i_s + i_{sc}^{W'}) - \alpha V_{rw} d_{xx}^2 \right] \\
&\quad + \left[4\alpha h_{yr} (m_y^W i_s + i_{sc}^{W'}) + i_s^2 \right] \left[\alpha h_{yr} (m_y^W i_s + i_{sc}^{W'}) + V_{rw} d_{xx}^2 \right]
\end{aligned} \tag{3.10}$$

and

$$\begin{aligned}
h_{yw} &= h_c^W - 2V_{rw} d_{xx} m_y^W m_y^R; \quad h_{yr} = h_c^R - 2d_{xx} m_y^W m_y^R \\
i_{sc}^{W'} &= \alpha_W (h_c^W - 2V_{rw} d_{xx} m_y^W m_y^R)
\end{aligned}$$

3.2 Modeling magnetic coupling fields

General properties of magnetic coupling tensors

Now we would like to establish the numerical framework to calculate magnetic coupling field between W and R magnets. The method described in this section is applied for both in-plane and PMA magnets. For a system of two magnets such as Write and Read, the total energy of the system is:

$$E = \frac{-\mu_0}{2} \left[M_W([\tilde{N}]^W + [\tilde{H}_k]^W)M_W + M_R([\tilde{N}]^R + [\tilde{H}_k]^R)M_R + 2M_R[\tilde{D}]M_W + 2\vec{m}_R[\tilde{J}_{int}]\vec{m}_W \right] \quad (3.11)$$

where $\vec{M}_W = M_s^W \vec{m}_W$ and $\vec{M}_R = M_s^R \vec{m}_R$ (M_s is the magnetization saturation). The first two terms in Eq.(3.11) represent the internal energies of Read and Write. The last two terms are the dipolar and **interface** exchange energy respectively. $H_k^{W,R}$ is the uniaxial tensor for W or R:

$$\text{For In-plane: } [\tilde{H}_k]^{W,R} = \begin{bmatrix} 0 & 0 & 0 \\ 0 & 0 & 0 \\ 0 & 0 & H_k^{W,R}V_{W,R} \end{bmatrix} \quad (3.12)$$

$$\text{For PMA: } [\tilde{H}_k]^{W,R} = \begin{bmatrix} 0 & 0 & 0 \\ 0 & H_k^{W,R}V_{W,R} & 0 \\ 0 & 0 & 0 \end{bmatrix} \quad (3.13)$$

$[\tilde{J}_{int}]$ is the (a function depending on volumes of both W and R) exchange interaction between two magnets. Note that, we take into account the geometry factors of both W and R for $[\tilde{J}]$. In general, the exchange tensor could have the diagonal form for both in-plane and PMA magnets [42]:

$$[\tilde{J}^{int}] = \begin{bmatrix} \tilde{J}_{xx} & 0 & 0 \\ 0 & \tilde{J}_{yy} & 0 \\ 0 & 0 & \tilde{J}_{zz} \end{bmatrix} \quad (3.14)$$

Those values could be obtained from the experiments as well as first principle calculations.

On the other hand, $[\tilde{N}]^{W,R}$ are the demagnetization tensors of Write (or Read) magnets and $[H_k]^{W,R}$ are uniaxial tensors of the magnets. In general, for **any shape** of W and R magnets, the volume dependent demagnetization tensors and dipolar tensors can be defined as [43]:

$$[\tilde{N}]_{ij}^{W,R} = \frac{1}{4\pi} \int_{V_{W,R}} \nabla_i \left(\int_{V_{W,R}} \nabla_j \left(\frac{1}{|\vec{r} - \vec{r}'|} \right) d\vec{r}' \right) d\vec{r} \quad (3.15)$$

$$[\tilde{D}]_{ij} = \frac{1}{4\pi} \int_{V_R} \nabla_i \left(\int_{V_W} \nabla_j \left(\frac{1}{|\vec{r} - \vec{r}'|} \right) d\vec{r}' \right) d\vec{r} \quad (3.16)$$

where $i, j = x, y, z$. The $[\tilde{N}]^W$, $[\tilde{N}]^R$ and $[\tilde{D}]$ tensors can be calculated as:

$$\tilde{d}_{ij}(\vec{r}') = \frac{1}{4\pi} \int_V \nabla_i \nabla_j \left(\frac{1}{|\vec{r} - \vec{r}'|} \right) d\vec{r} = \int_V dV \frac{3(r_i - r'_i)(r_j - r'_j) - R^2 \delta_{ij}}{R^2} \quad (3.17)$$

where $R^2 = \sum_i (r_i - r'_i)^2$. Physically, $\tilde{d}_{ij}(\vec{r}')$ represents the strength of the dipolar field (at the point \vec{r}') in the j direction due to a magnet pointing in the i direction. From Eq.(3.15) and Eq.(3.16), the demagnetization tensors of W (or R) are obtained by integrating the dipolar fields of W (or R) magnet within **itself** while the dipolar tensors of $W - R$ pair magnets are obtained by integrating dipolar fields of W at R or vice versa.

For in-plane magnets having bar shapes, one can derive the analytical expressions for \tilde{d}_{ij} and the details can be found in the appendix B. However, at the moment, we would like to consider the general properties of the \tilde{d}_{ij} . We can always easily prove from Eq.(3.17) that:

- The off-diagonal terms $\tilde{d}_{ij}(\vec{r}')$ are odd functions in the i AND j direction, namely: $\tilde{d}_{ij}(r'_i) = -\tilde{d}_{ij}(-r'_i)$; $\tilde{d}_{ij}(r'_j) = -\tilde{d}_{ij}(-r'_j)$
- The diagonal terms $\tilde{d}_{ii}(\vec{r}')$ are even functions in the i direction: $\tilde{d}_{ii}(r'_i) = \tilde{d}_{ii}(-r'_i)$

Therefore, the demagnetization tensors of bar magnets having dimension $2x_b \times 2y_b \times 2z_b$ have only the diagonal terms:

$$\begin{aligned} [\tilde{N}]_{ij} &= \int_V \tilde{d}_{ij}(\vec{r}') dV' = \int_{-x_b}^{x_b} \int_{-y_b}^{y_b} \int_{-z_b}^{z_b} \tilde{d}_{ij}(x', y', z') dV' \\ &= \begin{bmatrix} \tilde{N}_{xx} & 0 & 0 \\ 0 & \tilde{N}_{yy} & 0 \\ 0 & 0 & \tilde{N}_{zz} \end{bmatrix} \end{aligned} \quad (3.18)$$

On top of that, as shown in [43], the trace of \tilde{N} is the negative of the volume of the magnet while the trace of the \tilde{D} is zero.

$$\sum_i \tilde{N}_{ii} = -V \quad (3.19)$$

$$\sum_i \tilde{D}_{ii} = 0 \quad (3.20)$$

From the total energy Eq.(3.11), one can obtain the fields acting on W and R magnets:

$$\vec{H}_W = -\nabla_{\hat{M}_W} \left(\frac{E/\mu_0}{V_W} \right) = ([N]^W + [H_k]^W) M_W + ([D]^{WR} + [J]_{int}^{WR}) M^R \quad (3.21)$$

$$\vec{H}_R = -\nabla_{\hat{M}_R} \left(\frac{E/\mu_0}{V_R} \right) = ([N]^R + [H_k]^R) M_R + ([D]^{RW} + [J]_{int}^{RW}) M^W \quad (3.22)$$

where the volume normalized tensors are defined as:

$$[N]^{W,R} = [\tilde{N}]^{W,R}/V^{W,R}; [H]^{W,R} = [\tilde{H}]^{W,R}/V^{W,R} \quad (3.23)$$

$$[D]^{WR} = [\tilde{D}]/V_W; [D]^{RW} = [\tilde{D}]/V_R \quad (3.24)$$

$$[J]_{int}^{WR} = [\tilde{J}_{int}]/(M_s^R M_s^W V_W); [J]_{int}^{RW} = [\tilde{J}_{int}]/(M_s^R M_s^W V_R) \quad (3.25)$$

Physically, the $[D]^{RW}$ is the dipolar tensor at Read due to Write and $[D]^{WR}$ is dipolar tensor at Write due to Read. And

$$[D]^{WR} = \frac{V_R}{V_W} [D]^{RW} \quad (3.26)$$

Similarly, one can have

$$[J]_{int}^{WR} = \frac{V_R}{V_W} [J]_{int}^{RW} \quad (3.27)$$

which is in agreement with [40]. Note that in a simple case where W and R have the same overlap area, our J_{int} is inversely proportional to the thickness of W and R magnet since $[\tilde{J}_{int}]$ is proportional to the area of W or R.

From Eq.(3.21) and Eq.(3.22), the dipolar and exchange interactions can be treated on an equal footing. Therefore, from now on we mainly focus on the dipolar coupling part.

3.3 Stability considerations for spin current interacting with *in-plane* dipolar coupled magnets

3.3.1 Key parameters describing the dipolar and demagnetization fields

Next we would like to establish key parameters describing the internal and dipolar fields assuming that there is no exchange interaction between magnets $[\tilde{J}] = 0_{3 \times 3}$. Note that $\hat{m} \times [N]\hat{m} = \hat{m} \times ([N] - N_{xx}I_{3 \times 3})\hat{m}$ in the LLG equation (Eq.(3.1)). Therefore, one can rewrite the demagnetization tensor in the following form:

$$[N]^{W,R} \equiv \begin{bmatrix} 0 & 0 & 0 \\ 0 & N_{yy} - N_{xx} & 0 \\ 0 & 0 & N_{zz} - N_{xx} \end{bmatrix}^{W,R} \quad (3.28)$$

This will lead to estimation of the coercive field of Read and Write magnets (without dipolar field):

$$H_c^{W,R} = (N_{zz}^{W,R} - N_{xx}^{W,R}) M_s^{W,R} + H_k^{W,R}.$$

However, this theoretical calculations usually overestimate the coercive fields in comparison to the experimental values. It could be due to multi-domains comprising the magnet or/and other effects which usually result in lower switching fields. For that reason, we introduce an effective field for W or R magnet $H_{eff}^{W,R}$ so that

$$H_c^{W,R} = (N_{zz}^{W,R} - N_{xx}^{W,R}) M_s^{W,R} + H_k^{W,R} + H_{eff}^{W,R}.$$

are the same as the reported experimental values. Therefore the total effective internal field tensors can be written as:

$$[N]^{W,R} + [H_k]^{W,R} = \begin{bmatrix} 0 & 0 & 0 \\ 0 & -H_d^{W,R}/M_s^{W,R} & 0 \\ 0 & 0 & H_c^{W,R}/M_s^{W,R} \end{bmatrix} \quad (3.29)$$

where we define the demagnetization fields $H_d^{W,R} = (N_{xx}^{W,R} - N_{yy}^{W,R})M_s^{W,R}$. For this, we have proved the first terms of the fields \vec{H}_W and \vec{H}_R defined in Eq.(3.2) and Eq.(3.3). On the other hand, the dipolar $[D]$ tensor of $W - R$ pair in general has five independent variables:

$$D^{RW} = \begin{bmatrix} D_{xx} & D_{xy} & D_{xz} \\ D_{xy} & D_{yy} = -(D_{xx} + D_{zz}) & D_{yz} \\ D_{xz} & D_{yz} & D_{zz} \end{bmatrix} \quad (3.30)$$

and one can now analyze the stability of the system numerically by solving the coupled LLG Eq.(3.1) with the fields \vec{H}_W and \vec{H}_R defined in Eq.(3.21), Eq.(3.22), Eq.(3.29) and Eq.(3.30)

However, for the analytical purpose, we assume that the R magnet is placed symmetrically in the width direction (x) with respect to the W magnet. Since d_{xy} and d_{xz} are odd functions in the x direction,

$$[D]_{xj}^{RW} = \int_{V_R} d_{ij}(\vec{r}') dV_R = \int_{-x_R}^{x_R} \int \int d_{xj}(x', y', z') dV_R = 0 \quad (3.31)$$

with $j = y, z$. Hence, we have the following form of the dipolar tensor stated earlier in Eq.(3.2) and Eq.(3.3) :

$$[D]^{RW} = \begin{bmatrix} D_{xx} & 0 & 0 \\ 0 & -(D_{xx} + D_{zz}) & D_{yz} \\ 0 & D_{yz} & D_{zz} \end{bmatrix} \quad (3.32)$$

In all simulations, we assume that the demagnetization field is the dominant one $H_d \gg D_{ij}M_s$. Therefore, one can approximate $D_{yy} = 0$. Next, we will show that

the D_{yz} has a minor contribution to the stability of the system so that one can approximate $D_{yz} = 0$ in the calculations. Using the normalized fields:

$$\begin{aligned} h_d^{W,R} &= H_d^{W,R}/H_c^R, h_c^R = 1, h_c^W = H_c^W/H_c^R \\ d_{ij} &= D_{ij}M_s^W/H_c^R, V_{rw} = M_s^R V_R/M_s^W V_W \end{aligned} \quad (3.33)$$

One can approximate the total energy as:

$$\begin{aligned} E \approx & -\frac{\mu_0}{2} V_W M_s^W H_c^R \left[(-h_d^W m_y^W m_y^W + h_c^W m_z^W m_z^W) \right. \\ & \left. + (-h_d^R m_y^R m_y^R + m_z^R m_z^R) V_{rw} + 2d_{xx} m_x^W m_x^R + d_{zz} m_z^W m_z^R V_{rw} \right] \end{aligned} \quad (3.34)$$

Therefore, the key parameters to describe dipolar coupled magnets are d_{xx}, d_{zz}, h_d, h_c and V_{rw} .

Up to now, we have proven the internal and dipolar fields of coupled W-R magnets \vec{H}_W and \vec{H}_R having the forms defined in Eq.(3.2) and Eq.(3.3). Those fields now can be used to solve the coupled LLG Eq.(3.1) to study the system of two coupled magnets interacting with spin current.

3.3.2 Stability condition for in-plane coupled magnets

Fig.3.2(a) shows the numerical simulations of the system of $W - R$ magnets having dipolar coupling energy by solving coupled LLG Eq.(3.1) to determine stable/unstable regimes of the parallel states $m_z^W m_z^R = 1$ as a function of normalized d_{zz} and d_{xx} (both are negative). The simulations were done for different values of the magnetic moment ratio $V_{rw} = 1, 0.7, 0.5, 0.3$. For a given V_{rw} , d_{zz} and d_{xx} , the LLG simulations can determine the **stable** (black) and **unstable** regimes of the initial parallel state. As one reduces the magnetic moment ratio V_{rw} , the stable (black) regimes follow the arrows in the figure and extend their areas. For a given value of d_{zz} , reducing the magnetic moment ratio V_{rw} will require larger d_{xx} to make the system unstable. In other words, reducing the V_{rw} makes the dipolar coupling between W and R magnet weaker since:

$$[d]^{WR} = V_{rw}[d]^{RW} = V_{rw}[d]$$

R/W: In-plane

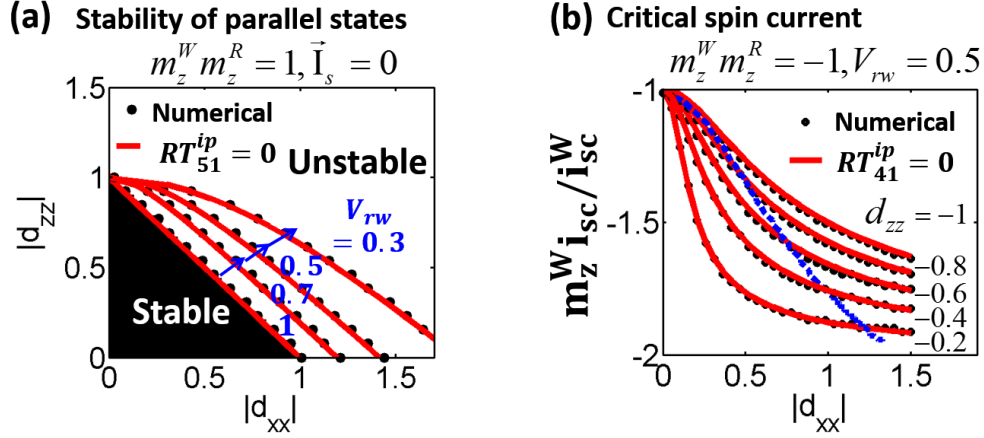


Fig. 3.2. Stability consideration of the system in Fig.3.1(a) where Read and Write are in-plane magnets a) Numerical LLG simulations show the stable/unstable regimes of a parallel state $m_z^W m_z^R = 1$ (without spin current) as a function of normalized dipolar coupling strength d_{zz} and d_{xx} (All the fields are normalized to the coercive field of the Read and $H_c^R = 1$). The red line separating the two regimes is the analytical solution of $RT_{51}^{ip} = 0$ in Eq.(3.5). b) LLG simulations of the required critical spin currents (normalized by the critical spin current of the isolated Write magnet i_{sc}^W) to make the anti-parallel state $m_z^W m_z^R = -1$ unstable as a function of d_{xx} for different values of d_{zz} . Here the spin current is polarized in the z direction and the analytical red lines are obtained by solving $RT_{41}^{ip} = 0$ (Eq.(3.7)). The dash blue line is used to determine the smallest $|d_{xx}|$ (for a given d_{zz}) such that above this value, the dipolar coupling is strong enough to make parallel states unstable. Parameters: $h_d^W = h_d^R = 100$; $h_c^R = h_c^W = 1$; $V_{rw} = V_R M_s^R / V_W M_s^W = 0.5$.

Therefore, working with small V_{rw} is preferable if one wants to minimize the effects of dipolar coupling. On the other hand, it is interesting to note that the parallel states could be unstable even when $d_{zz} < 1$. This implies that one can switch the Read magnet by having the dipolar field along the easy axis (z) from the Write and this field is smaller than the coercive field of Read. We will confirm this observation with experiment described later on.

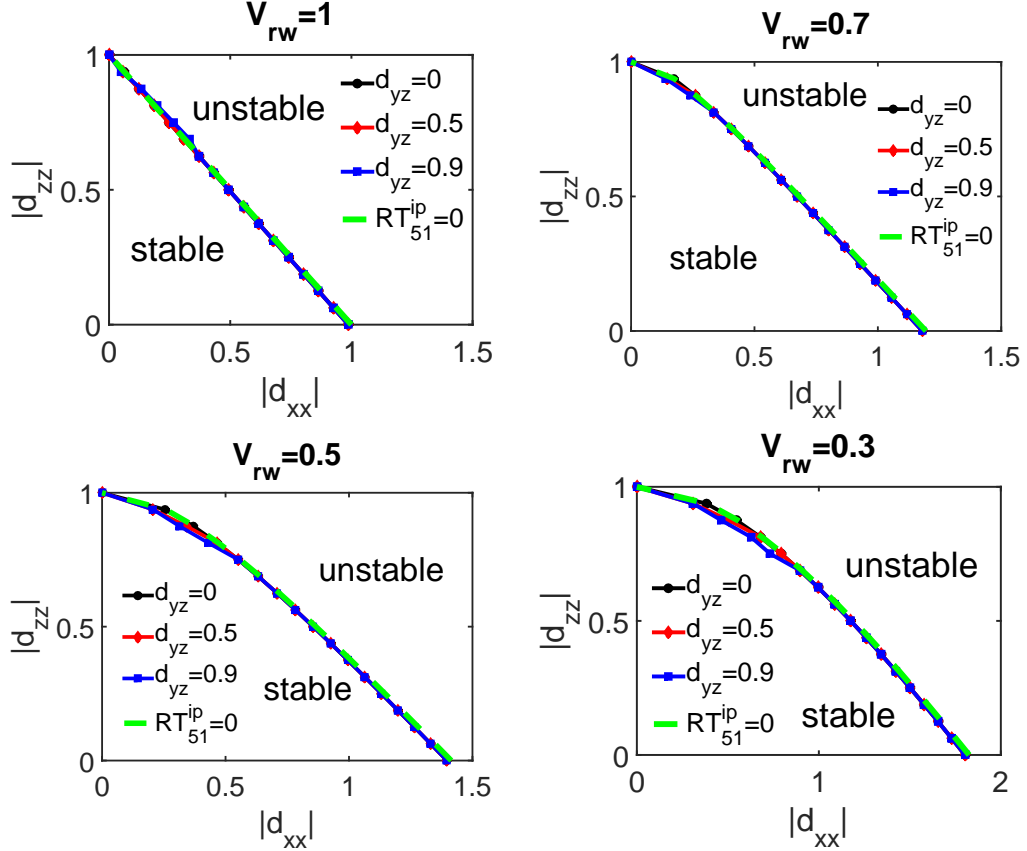


Fig. 3.3. Numerical LLG simulations show the stable/unstable regimes of a parallel state $m_z^W m_z^R = 1$ as a function of normalized dipolar coupling strength d_{zz} , d_{xx} and d_{yz} . Here all the fields are normalized to the coercive field of the Read H_c^R . The lines separating the stable and unstable regimes are almost independent from the values of d_{yz} . Note that $RT_{51}^{ip} = 0$ is the **analytical** solution of Eq.(3.5) or Eq.(3.36).

Note that the simulations in Fig.3.2(a) were done by setting $d_{yz} = 0$ in the Eq.(3.2) and Eq.(3.3). We will argue that d_{yz} will play a minor role in determining the stability of the system. In Fig.3.3, we recalculated Fig.3.2(a) with different values of d_{yz} . As one can see, the lines separating the stable from unstable regimes are almost independent from the values of d_{yz} .

By analyzing the eigenvalues of Jacobian at fix points of the LLG equations describing the coupled system, we obtained the general stability criteria of the system

(appendix C). However, for the system having $h_d^W = h_d^R$ and the damping coefficient $\alpha_W = \alpha_R$, the state $\{m_z^W, m_z^R\}$ will be unstable when either $RT_{31}^{ip} < 0$ or $RT_{51}^{ip} < 0$ in Eq.(3.36) which is the same as in Eq.(3.5).

$$RT_{31}^{ip} = h_c^W + 1 + m_z^R m_z^W (1 + V_{rw} d_{zz}) \quad (3.35)$$

$$RT_{51}^{ip} = (1 + m_z^R m_z^W d_{zz})(h_c^W + m_z^R m_z^W V_{rw} d_{zz}) - V_{rw} d_{xx}^2 \quad (3.36)$$

For the range of d_{xx} and d_{zz} as in Fig.3.2(a), one can analyze the stability of the system basing on the sign of RT_{51}^{ip} only. As one can see our analytical model agrees well with the LLG simulation results. The lines separating stable from unstable regimes in Fig.3.2(a) were obtained via LLG simulations as well as by analytically solving $RT_{51}^{ip} = 0$ in Eq.(3.36). The analytical model also implies that, in the presence of d_{xx} , the system could be unstable ($RT_{51}^{ip} < 0$) for $|d_{zz}| < 1$.

3.3.3 Critical spin current for in-plane coupled magnets

Fig.3.2(b), on the other hand, shows LLG simulations of the required critical spin currents i_{sc} to make the dipolar stable (anti-parallel) $W - R$ magnets to be unstable as a function of dipolar coupling strength: d_{xx} and d_{zz} . The normalized spin current is defined as:

$$i_s = \frac{\vec{I}_s \cdot \hat{z}}{(2q/\hbar)\mu_0 H_c^R M_s^W V_W} \quad (3.37)$$

Note that, the system is initially in an anti-parallel *stable* configuration. When $d_{xx} = 0$, the critical spin currents are the same as $i_{sc}^W = \alpha_W(h_c^W + h_d^W/2)$ which is the normalized critical spin current of an isolated Write magnet and it is Sun's criteria [21] if one converts it back to the real unit by a factor $2q/\hbar\mu_0 H_c^R M_s^W V_W$. This is understandable since spin current basically tries to switch only the Write magnet and the dipolar field at Write to due Read ($V_{rw} d_{zz} \ll h_d$) acts as a small external magnetic field which should not affect the critical spin current. However, the non-trivial thing is that when $d_{xx} \neq 0$, spin current now starts to see a coupled Read-Write magnet, resulting in a higher switching spin current. Note that, unstable states such

as oscillations or any deviations from the initial state will be labeled as unstable in the LLG simulations.

By analyzing the eigenvalues of Jacobian at fix points, we obtain the general stability criteria which give the required critical spin currents I_{sc} to make the coupled $W - R$ magnets to be unstable. However, for a simple case where $h_d^W = h_d^R = h_d$, $\alpha_W = \alpha_R = \alpha$ as in Fig.3.2(b), the state $\{m_z^W, m_z^R\}$ will be unstable when either $RT_{21}^{ip} < 0$ or $RT_{41}^{ip} < 0$ in Eq.(3.39), which is the same as the one defined in Eq.(3.7).

$$RT_{21}^{ip} = m_z^W i_s + 2i_{sc}^W + \alpha m_z^W m_z^R (1 + V_{rw}) d_{zz} \quad (3.38)$$

$$\begin{aligned} RT_{41}^{ip} = & 4V_{rw} \left[\alpha m_z^W i_s (h_z^R - h_z^W) + (m_z^W i_s + 2I_{sc}^W)^2 \right] d_{xx}^2 \\ & + \alpha (m_z^W i_s + I_{sc}^W) \left[(h_z^R - h_z^W)^2 h_d \right. \\ & \left. + 4(m_z^W i_s + I_{sc}^W) [(m_z^W i_s + I_{sc}^W) h_z^R + I_{sc}^W h_z^W] \right] \end{aligned} \quad (3.39)$$

where

$$\begin{aligned} h_z^W &= h_c^W + V_{rw} d_{zz} m_z^W m_z^R \\ h_z^R &= h_c^R + d_{zz} m_z^W m_z^R \end{aligned}$$

For the range of d_{xx} and i_s as in Fig.3.2(b), the critical spin currents i_{sc} can be obtained by solving $RT_{41}^{ip} = 0$ and one can see that our analytical model agrees with the LLG simulation results. It also implies that when $d_{xx} = 0$, $|i_s| = i_{sc}^W$ is the solution of $RT_{41}^{ip} = 0$ and for large d_{xx} , the solution is $|i_s| = -2i_{sc}^W$. The dash blue line in Fig.3.2(b) is used to determine the smallest $|d_{xx}|$ (for a given d_{zz}) such that above this value, the dipolar coupling is strong enough to make the parallel state unstable.

3.3.4 Benchmark against experiments

We would like to benchmark our theory with the experimental results for dipolar coupling between two permalloy magnets (Read and Write). Fig.3.4(a) shows the experimental setup where Read magnet ($120nm \times 100nm \times 10nm$) and Write magnet ($600nm \times 140nm \times 10nm$) are stacked vertically and separated by $15nm$ Al_2O_3

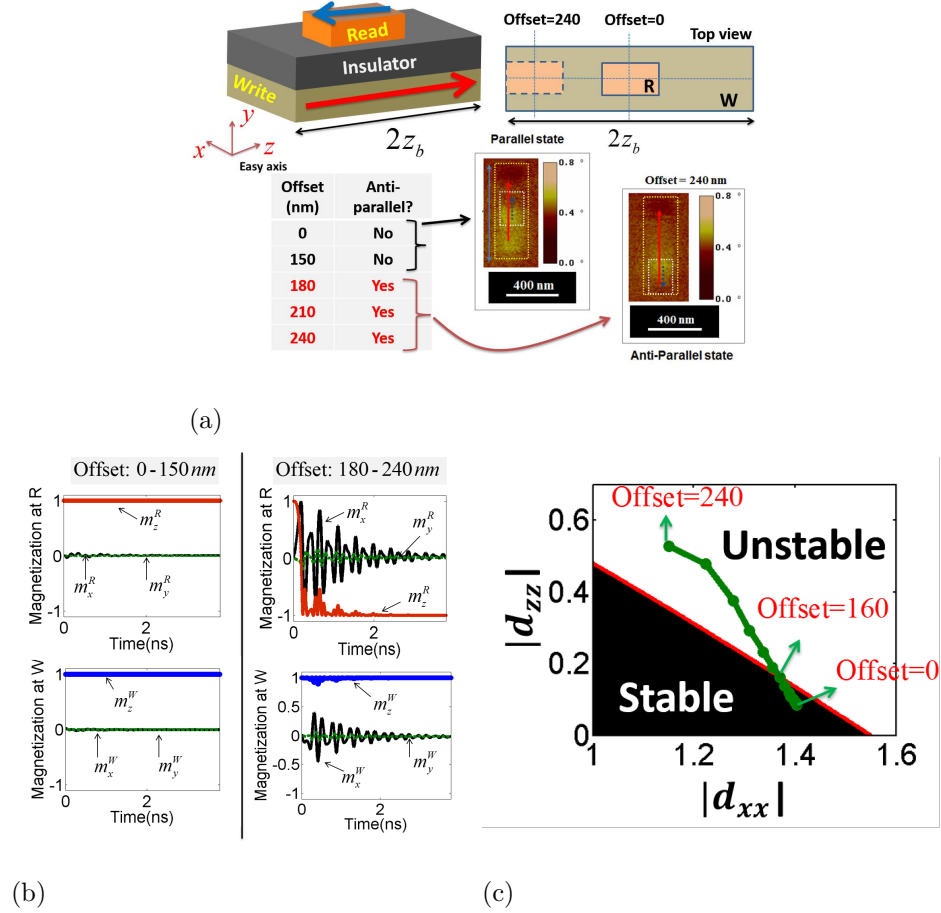


Fig. 3.4. a) Experimental setups to detect the anti-parallel states between the Read and Write magnets as a function of offsets (distance from center to center in the easy axis of two magnets). They are initially aligned by an external magnetic field, the field is then removed and MFM scan is followed. Read: $120\text{nm} \times 100\text{nm} \times 10\text{nm}$, Write: $600\text{nm} \times 140\text{nm} \times 10\text{nm}$ and they are separated by 15nm insulator. b) LLG simulations show the switching of Read magnet m_z^R when offsets are greater than 150nm . c) The stability phase diagram obtained from determining the sign of RT_{51}^{ip} and the calculations of d_{xx} and d_{zz} as a function of offset (dot line) for the experiment. The system enters the unstable regime when offsets are greater than 150nm , which also agrees with both numerical and experimental results.

insulator. Magnetic Force Microscopy (MFM) is used to detect their magnetizations and determine if the two develop an anti-parallel state starting from a parallel state

(initially both Read and Write are aligned by an external magnetic field, the field is removed and MFM scan is followed). In the experiment, the saturation magnetizations are $M_s^R = M_s^W = 0.86 \times 10^6 A/m$ and the coercive fields of Read and Write magnets are $H_c^R = 32mT$ and $H_c^W = 15mT$ respectively. As shown in Fig.3.4(a), the anti-parallel states are detected only when the offsets (distance from center to center in the easy axis of two magnets) are greater than $150nm$.

To compare our numerical and analytical simulations with the experimental results, we first calculate the internal fields by evaluating the demagnetization tensors $[N]^{W,R}$ (Eq.(3.18)) for given dimensions of W and R magnets. For every offset, the dipolar tensor $[D]$ was re-evaluated (for the details of calculations of $[N],[D]$, see the appendix B). Those tensors together with the coercive fields of W and R provided by experiments will be used to solve the coupled LLG equations (Eq.(3.1)) to determine final states of the two magnets. Fig.3.4(b) shows the LLG simulations of $W - R$ magnets which initially were set in a parallel state $m_z^W = 1; m_z^R = 1$ as a function of offsets. The final states are *quantitatively* in agreement with experiment in the sense that Read is switched when the offsets are greater than $150nm$. Note that the simulations were done by using the full normalized $[D]$ (or normalized $[d]$) tensor with 3 independent variables, namely $d_{xx}, d_{yy} = -d_{xx} - d_{zz}, d_{zz}$ and d_{yz} since the Read was put symmetrically in the width direction (x) with respect to the Write magnet.

We further analyzed the analytical stability condition for this system based on RT_{51}^{ip} in Eq.(3.36). For every offset in Fig.3.4(a), the normalized dipolar tensor components $d_{zz} = D_{zz}M_s^W/H_c^R; d_{xx} = D_{xx}M_s^W/H_c^R$ were calculated and plotted as a dot line in Fig.3.4(c). To determine the stability of the system, we also plotted the phase diagram obtained by evaluating the sign of RT_{51}^{ip} in Eq.(3.36). It clearly shows that the system enters the unstable regime as offsets are greater than $150nm$, which agrees with both numerical and experimental results. Note that, in all range of offset, the d_{zz} is always smaller than the coercive field of the Read magnet ($H_c^R = 1$) and yet the switching can happen due to the presence of d_{xx} .

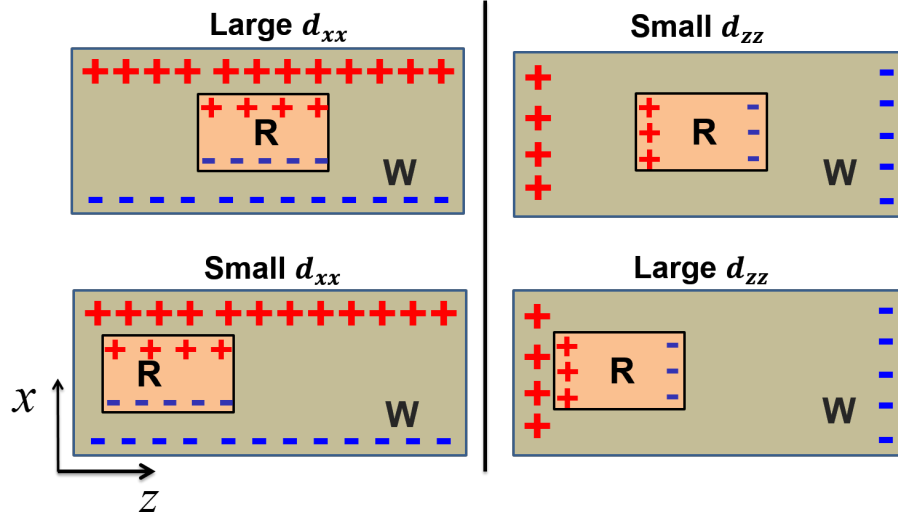


Fig. 3.5. The trends of d_{zz} and d_{xx} as a function of offsets can be captured by the charge model mentioned in appendix B.

On the other hand, we can qualitatively explain the behavior of d_{xx} and d_{zz} as a function of offsets (Fig.3.4(c)) based on the charge model of a magnet explained in appendix B. The bottom line is that, the dipolar fields coming out from a bar magnet \vec{M} can be viewed as the electric fields coming out from the two sheets of charge having the charge density $\rho = -\nabla \cdot \vec{M}$. Therefore, d_{xx} is large for small offset since the charges in the Read magnet are now surround by many charges from the Write magnet. However, d_{zz} is small in this case since the charges in the Read and Write magnets are far away from each other. For large offsets, similarly one can explain why d_{zz} is large and d_{xx} is small.

3.4 Stability considerations for spin current interacting with PMA dipolar coupled magnets

3.4.1 Key parameters describing the dipolar and demagnetization fields

In this section, we extend our results discussed for in-plane magnets in the previous section to PMA magnets. Fig.3.1(b) describes the system that we are studying here where Read and Write are now PMA magnets. In principle, the calculations of the dipolar and demagnetization tensors can be done by integrating Eq.(3.15) and Eq.(3.16) over the volumes of cylindrical magnets. When those tensors are known, one can proceed to test the stability of the systems. In particular, we assume:

$$\begin{aligned}
 H_R &= \begin{bmatrix} 0 & 0 & 0 \\ 0 & H_c^R & 0 \\ 0 & 0 & 0 \end{bmatrix} \begin{bmatrix} m_x^R \\ m_y^R \\ m_z^R \end{bmatrix} + M_s^W \begin{bmatrix} D_{xx} & 0 & 0 \\ 0 & -2D_{xx} & 0 \\ 0 & 0 & D_{xx} \end{bmatrix} \begin{bmatrix} m_x^W \\ m_y^W \\ m_z^W \end{bmatrix} \\
 H_W &= \begin{bmatrix} 0 & 0 & 0 \\ 0 & H_c^W & 0 \\ 0 & 0 & 0 \end{bmatrix} \begin{bmatrix} m_x^W \\ m_y^W \\ m_z^W \end{bmatrix} + \frac{V_R}{V_W} M_s^R \begin{bmatrix} D_{xx} & 0 & 0 \\ 0 & -2D_{xx} & 0 \\ 0 & 0 & D_{xx} \end{bmatrix} \begin{bmatrix} m_x^R \\ m_y^R \\ m_z^R \end{bmatrix}
 \end{aligned} \tag{3.40}$$

which can be justified by the following arguments:

- Since there is no difference between x and z for PMA magnets, the demagnetization tensors have the following form:

$$[N]^{W,R} = \begin{bmatrix} N_{xx} & 0 & 0 \\ 0 & N_{yy} = -1 - 2N_{xx} & 0 \\ 0 & 0 & N_{xx} \end{bmatrix}^{W,R} \tag{3.41}$$

By noting that $\hat{m} \times [N]\hat{m} = \hat{m} \times ([N] - N_{xx}I_{3 \times 3})\hat{m}$ in the LLG equations and one can add effective fields $H_{eff}^{W,R}$ so that coercive fields are the same with the

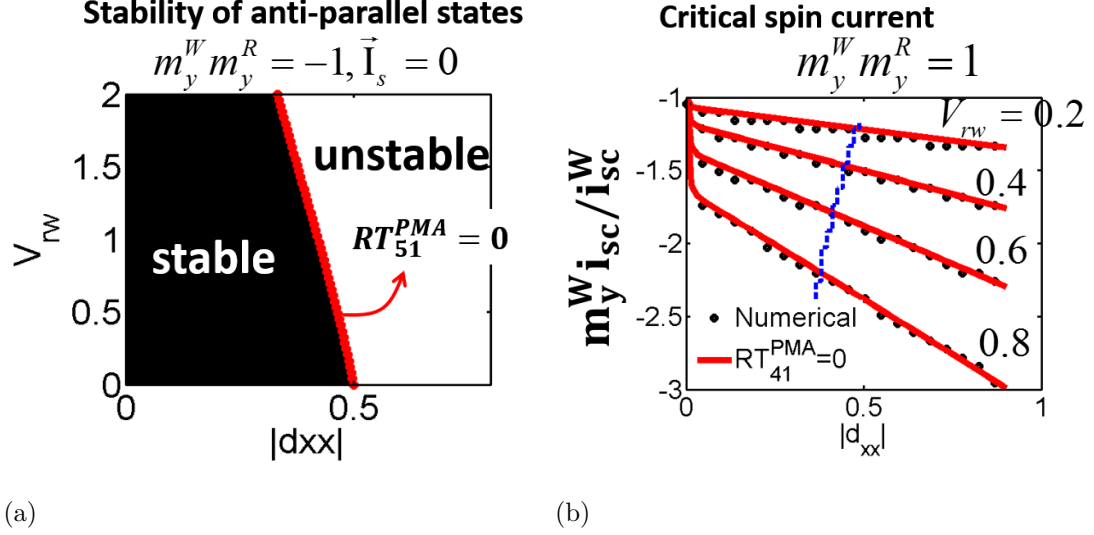


Fig. 3.6. Stability consideration of the system where Read and Write are PMA magnets. (a) LLG simulations and analytical results show the stable/unstable regimes of anti-parallel states $m_y^W m_y^R = -1$ (without spin current) as a function of normalized d_{xx} and $V_{rw} = V_R M_s^R / V_W M_s^W$ (all the fields are normalized to the coercive field of the Read: H_c^R). (b) LLG and analytical results for required critical spin current (normalized by the critical spin current of the isolated Write magnet i_{sc}^W) to make the parallel state $m_y^W m_y^R = 1$ unstable as a function of d_{xx} for different values of V_{rw} . The dash blue line is used to determine smallest $|d_{xx}|$ (for a given V_{rw}) such that above this value, the dipolar coupling is strong enough to make anti-parallel state unstable. Here $h_c^R = h_c^W = 1$.

experimental values, the internal fields of W, R magnets will have the following form:

$$\begin{aligned}
 [N]^{W,R} M_s^{W,R} + [H_k]^{W,R} &= \begin{bmatrix} 0 & 0 & 0 \\ 0 & (N_{yy} - N_{xx})M_s + H_k + H_{eff} & 0 \\ 0 & 0 & 0 \end{bmatrix}^{W,R} \\
 &= \begin{bmatrix} 0 & 0 & 0 \\ 0 & H_c^{W,R} & 0 \\ 0 & 0 & 0 \end{bmatrix}
 \end{aligned} \tag{3.42}$$

where $H_c^{W,R} = (N_{yy} - N_{xx})M_s^{W,R} + H_k^{W,R} + H_{eff}^{W,R}$.

- Since both W and R have cylindrical shapes, one can always choose the coordinates in that R magnet is placed symmetrically in either x or z directions (note that we have proved that \tilde{d}_{ij} in Eq.(3.17) is odd function in i and j directions). This results in the diagonal form of the dipolar tensor:

$$[D]^{RW} = [D] = \begin{bmatrix} D_{xx} & 0 & 0 \\ 0 & -2D_{xx} & 0 \\ 0 & 0 & D_{xx} \end{bmatrix} \quad (3.43)$$

and the total energy of system in terms of the normalized variables is :

$$E = -\frac{\mu_0}{2} V_W M_s^W H_c^R \left[h_c^W m_y^W m_y^W + (m_y^R m_y^R - 4d_{xx} m_y^W m_y^R) V_{rw} \right. \\ \left. + 2d_{xx} (m_x^W m_x^R + m_z^W m_z^R) V_{rw} \right] \quad (3.44)$$

Hence the key parameters to describe the fields of two PMA dipolar coupled magnets are $d_{xx} = d_{zz}$, h_c and V_{rw} .

3.4.2 Stability condition for PMA coupled magnets

Fig.3.6(a) shows the LLG simulations to determine the stability (without spin current) of the anti-parallel states $m_y^W m_y^R = -1$ as a function of normalized dipolar field d_{xx} and the magnetic moment ratio $V_{rw} = V_R M_s^R / V_W M_s^W$ of the two PMA magnets. Firstly, similar to the in-plane magnets, the anti-parallel states could be unstable even when $|d_{xx}| < 0.5$ which is equivalent to $d_{yy} = -2d_{xx} < 1$ (where $H_c^R = 1$ is the coercive field of the Read magnet). Secondly, for a given value of d_{xx} , reducing V_{rw} could make the system go from unstable to stable state. Hence, similar to in-plane magnets in Fig.3.1(a), working with small V_{rw} is preferable if one wants to minimize the effects of dipolar coupling for PMA magnets. This also is in agreement with previous studies [44, 45].

Basing on the Jacobian analysis (appendix C), we obtain the general stability criteria of the system. However, for the system with the same damping coefficient

$\alpha_W = \alpha_R = \alpha$, as in LLG simulations for Fig.3.6(a), one can obtain the line separating stable from unstable regimes by solving $RT_{51}^{PMA} = 0$ where:

$$\begin{aligned} RT_{51}^{PMA} = & [(1 - 2m_y^R m_y^W d_{xx}) + (h_c^W - 2m_y^R m_y^W V_{rw} d_{xx})] \\ & \times [(1 - 2m_y^R m_y^W d_{xx}) (h_c^W - 2m_y^R m_y^W V_{rw} d_{xx}) - V_{rw} d_{xx}^2] \end{aligned} \quad (3.45)$$

3.4.3 Critical spin current for PMA coupled magnets

Fig.3.6(b) shows LLG simulations of the required critical spin currents i_{sc} to make the parallel W/R magnets unstable as a function of d_{xx} for different values of V_{rw} . When $d_{xx} = 0$, there is no coupling between the two magnets and the critical spin currents are the same as the critical spin currents $i_{sc}^W = \alpha h_c^W$ of an isolated Write magnet. An increment of d_{xx} will require more spin current to make the system unstable similar to the in-plane magnets in Fig.3.2(b). Again, unstable states such as oscillations or deviations from the initial state will be counted as unstable in the LLG simulations.

In the appendix C, we show the general stability criteria which give the required critical spin currents i_{sc} to make the coupled W/R magnets to be unstable. However, for a simple case where $\alpha_W = \alpha_R$ as in Fig.3.6(b), the analytical lines can be obtained by solving $RT_{41}^{PMA} = 0$ where:

$$\begin{aligned} RT_{41}^{PMA} = & -4V_{rw}^2 \alpha^2 d_{xx}^4 + \alpha (h_{yr} - h_{yw})^2 \left[h_{yr} (m_y^W i_s + i_{sc}^{W'}) - \alpha V_{rw} d_{xx}^2 \right] \\ & + \left[4\alpha h_{yr} (m_y^W i_s + i_{sc}^{W'}) + i_s^2 \right] \left[\alpha h_{yr} (m_y^W i_s + i_{sc}^{W'}) + V_{rw} d_{xx}^2 \right] \end{aligned} \quad (3.46)$$

and

$$\begin{aligned} h_{yw} &= h_c^W - 2V_{rw} d_{xx} m_y^W m_y^R; h_{yr} = h_c^R - 2d_{xx} m_y^W m_y^R \\ i_{sc}^{W'} &= \alpha_W (h_c^W - 2V_{rw} d_{xx} m_y^W m_y^R) \end{aligned}$$

3.5 Dipolar coupling designs in Spin Switches

Finally in this chapter, we would like to mention the behavior of dipolar tensors as a function of geometries of in-plane magnets and it could help to design Spin Switch

(SS) [17] which is a transistor like device having input-output isolation and gain. SS (Fig.3.7(a)) allows one to store information in the magnet and transfer the information in terms of charge current $\vec{I}_{in} \rightarrow \hat{m} \rightarrow \vec{I}_{out}$. The magnetization (information) of Write is determined by the spin current \vec{I}_s generated from charge current \vec{I}_{in} flowing through Giant Spin Hall materials such as: Ta, W, CuBi [13,46,47]. Based on the direction of Write, the Read magnet is switched via the dipolar coupling which provides a way to achieve input-output isolation [7, 17] and allows information to be transmitted from the input to the output without the need of external magnetic field for clocking.

Fig.3.7(a) also shows the schematic setups in searching for strong (switching) dipolar coupling between Read and Write in SS. In all simulations, we scaled the dimensions of both magnets to, for example, the thickness of bottom magnet y_b . The Read and Write magnets have a fix thickness $y_t = y_b$ and aspect ratio $z_t/x_t = z_b/x_b$. However, we varied the length of both Write and Read to find the strong dipolar coupling regime. In all cases, the Read is always put close to the edge (or poles) of the Write to maximize the dipolar coupling and the distance between closest edges δ is fixed $\delta/y_b = 10$. Fig.3.7(b) shows the calculations of the two main components of dipolar tensor at Read due to Write, $[D]^{RW} = [D]$, as a function of z_t and z_b . Although the calculations are general, one should pay attention to the regime below the dash line where Write volume is greater than the Read so that the Write can control the Read and ensure the directionality. Fig.3.7(c) shows the simulation results of switching diagram by using full $[D]$ with 4 independent variables D_{xx}, D_{zz}, D_{yy} and D_{yz} to solve coupled LLG for configurations below the dash line in Fig.3.7(b). For a given ratio of the coercive field and the saturation magnetization H_c^R/M_s^W , the LLG simulations will determine the critical line separating the switched (white) or not switched (black region in Fig.3.7(c)). As the coercive fields increase, the critical lines follow the green arrows and the switched regions are reduced. On the other hand, the analytical lines are obtained by solving the equation $RT_5 1^{ip} = 0$ (Eq.(3.36)) for each value of H_c^R/M_s^W . As one can see, the analytical results quantitatively agree with the numerical simulations.

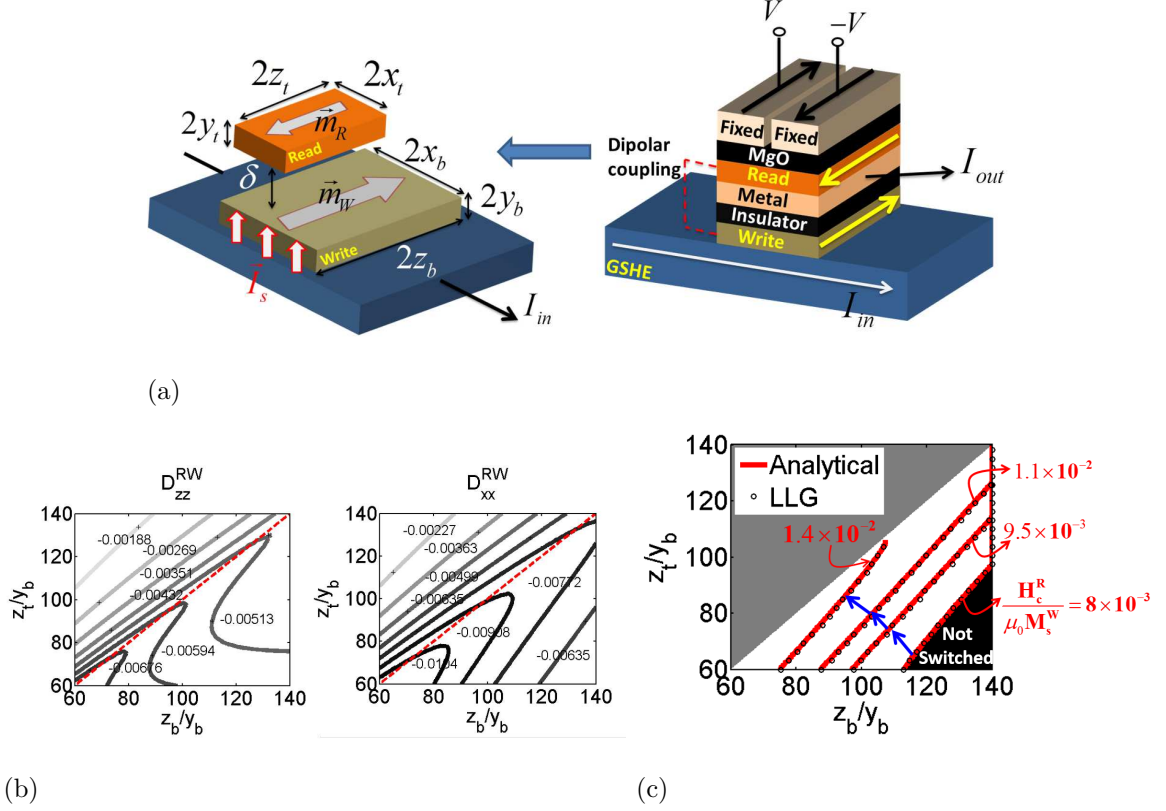


Fig. 3.7. (a) Schematic of spin switch device and the dipolar coupling between Write and Read magnets in SS. b) The two components of $D^{RW} = [D]$ as a function of the lengths of Write and Read having fixed aspect ratio $z_b/x_b = z_t/x_t = 1.5$, same thicknesses $y_b = y_t$ and the fixed distance between nearest edges $\delta/y_b = 10$. In all cases, the Read was always put close to the edge of the Write. c) The numerical LLG simulation lines separating the switched (white) and not switched (black) regimes starting from parallel states of $m_z^W m_z^R = 1$ as a function of $H_c^R/\mu_0 M_s^W$. The analytical red lines were obtained by solving $RT_{51}^{ip} = 0$. Here we assumed $H_c^W = H_c^R = 1$ and $M_s^W = M_s^R = 10^6 A/m$ and restricted ourselves to the case where $V_W \leq V_R$.

The general trend of switching is also in agreement with the trend of $[D]^{RW}$ tensor in the sense that having $z_b \gg z_t$ is good for minimizing the dipolar field while $z_b \approx z_t$ (the region near the diagonal) is preferred for maximizing the dipolar coupling. For each value of the coercive field, we assume $H_c^R = H_c^W$ and they do not dramatically change as a function of widths and lengths of Read and Write. This is a crude

approximation but can be justified as we mainly focus on comparing the numerical simulations with analytical switching conditions.

3.6 Summary

In summary, we have presented a macro-spin model (at zero temperature) to study a system of two magnets, which could be either in-plane or PMA, having magnetic coupling (could be exchange or dipolar coupling) and one of them could interact with spin current I_s . We analytically focus on the stability of the system where magnets are stacked vertically (along their smallest thicknesses) and the stability criteria are obtained directly from the LLG equations through a Jacobian analysis. Our key results are 1) the stability condition of Read and Write magnets due to magnetic coupling with/without spin current and 2) the required critical spin current to make magnetic coupling magnets unstable. The latter is essentially an extension of Sun's criteria for coupled magnets. Our analytical results are benchmarked against the LLG numerical simulations for both in-plane and PMA magnets. In addition, for in-plane magnets, the switching criteria due to dipolar coupling are in agreement with experiments.

The matlab codes used to generate the figures can be found at:

<https://drive.google.com/open?id=0B9ggzdMPbfz4VDdld0xPc19ldm8&authuser=0>

4. DIPOLAR FIELDS IN PERPENDICULAR MAGNETIC TUNNEL JUNCTIONS (pMTJ)

The contents of this chapter would be submitted for review, ‘Modeling stray fields in scaled perpendicular magnetic tunnel junction: a macro-spin approach’, V. Diep, , B. Behin-Aein and S. Datta.

4.1 Dipolar fields and their effects on Magnetic Tunnel Junctions

Magnetic tunnel junction (MTJ) has been an important and well-known device for Reading and Writing information in magnetic devices. It has been used as the main component of spin transfer torque magnetic random access memory (STT-MRAM) [18, 48, 49].

In the early time, magnets with in-plane anisotropy are implemented for free layer (FL) and reference layer (RL) in MTJ. However, these in-plane magnets require high spin current density ($J \sim 10^7 A/cm^2$) to be switched while maintaining thermal stability [50]. On the other hand, it has been known that perpendicular magnetic anisotropy (PMA) [51–53] could provide lower critical currents and allow one to scale the MTJ devices implemented with PMA magnets to small (tens of nm in diameter) dimensions without suffering the thermal stability.

Figure 4.1 shows a schematic structure of a pMTJ consisting of a storage layer or FL, a reference layer and synthetic anti-ferromagnetic (SAF) layers: SAF1 and SAF2. The reference layer, whose thickness is in the order of 1-2nm, on its own is not stable enough so it needs reinforcement by attaching to a SAF1 layer which is basically multi-magnetic layer. However, both reference and SAF1 layers exert magnetic fields or dipolar fields on the FL. This is unwanted since energy barriers for the two stable states of the free magnets 1 and 0 (or up and down) are now asymmetric. In other

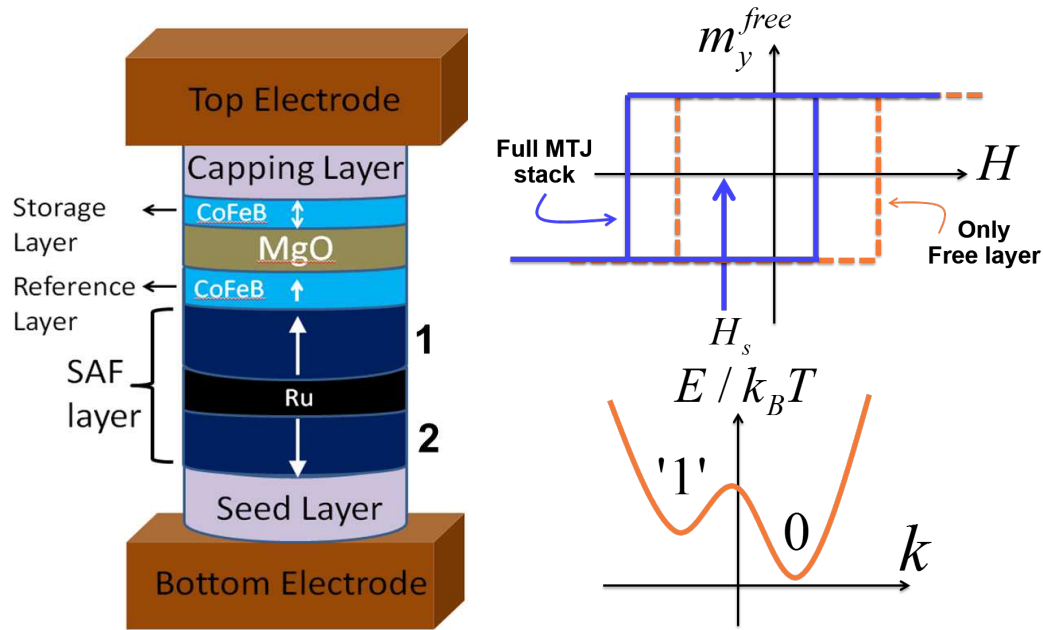


Fig. 4.1. A schematic structure of a full pMTJ stack. Because of the dipolar fields coming from the Ref and SAF layers, the hysteresis of the Free layer magnet does not center at 0 and the strength of the dipolar coupling can be measured via the shift of the hysteresis or H_s . Dipolar field also results in the energy difference for state 1 and 0.

words, the retention times for state 1 and state 0 are now different because of the dipolar fields. One way to measure the strength of the total dipolar fields at FL is to measure the shifting in the hysteresis switching loop of the FL.

In order to eliminate any magnetic field on the FL, SAF2 layer is added into the structure to compensate the effects of the reference layer and SAF1. For this reason, various design scenarios and situations have been developed to fully or partially compensate the dipolar due to reference + SAF1 layer stacks. Therefore, a good command on what happens to the stray fields under various design scenarios is called for.

Even in the presence of SAF2, the stray fields or dipolar fields at FL are still important problems in scaled pMTJs [44, 45, 54], making it very hard to design the pMTJ stack. In the scaled pMTJ, it has been reported that the dipolar fields are

comparable or even exceed the coercive fields of the FL [54]. This is unacceptable since we will completely lose the information stored in the magnet.

Our objective in this paper is to present a numerical and analytical macro-spin model to analyze the dipolar fields in systems having multi-magnetic layers as in the pMTJ devices. Our model is benchmarked against the micro-magnetic simulations as well as experiments. Therefore, the model can be used to design devices with symmetric retention time for various technology nodes. Finally, our model can also be coupled to spin transports to find out the impacts of stray fields on switching dynamics of pMTJ devices.

4.2 General numerical framework for calculating dipolar fields in pMTJs

4.2.1 Dipolar fields of a perpendicular magnetic anisotropy (PMA) magnet

We now want to calculate the dipolar fields between two pMTJ magnets (RL and FL). The general approach to calculate the dipolar field is to obtain the dipolar tensor by integrating the Eq.(3.16) which is rewritten here for the sake of clarity:

$$[\tilde{D}]_{ij} = \frac{1}{4\pi} \int_{V_{FL}} \nabla_i \left(\int_{V_{RL}} \nabla_j \left(\frac{1}{|\vec{r} - \vec{r}'|} \right) d\vec{r}' \right) d\vec{r} \quad (4.1)$$

where $i, j = x, y, z$. This, in turn, requires the calculations of the dipolar tensor at a *point in space* \vec{r}' due to the RL magnet:

$$\tilde{d}_{ij}(\vec{r}') = \frac{1}{4\pi} \int_{V_{RL}} \nabla_i \nabla_j \left(\frac{1}{|\vec{r} - \vec{r}'|} \right) d\vec{r} = \int_{V_{RL}} dV \frac{3(r_i - r'_i)(r_j - r'_j) - R^2 \delta_{ij}}{R^2} \quad (4.2)$$

Before going to the details of the calculations, we would like to know the general properties of the dipolar tensor in PMA magnets. Suppose we have a PMA magnet having cylindrical shape with x, z as the polar axis and y as the longitude axis. In principle, one should evaluate all 5 independent variables $\tilde{d}_{xx}, \tilde{d}_{zz}, \tilde{d}_{xy}, \tilde{d}_{xz}, \tilde{d}_{yz}$ and find out the stray fields. However, in vertical stacks of a FL and RL system, we can always choose a coordinate in that FL is put symmetrically in the x and z direction,

which leads to $\tilde{D}_{xz} = \tilde{D}_{xy} = \tilde{D}_{yz} = 0$ (since \tilde{d}_{ij} where $i \neq j$ is an odd function in i and j direction and note that $[\tilde{D}] = \int[\tilde{d}]dV$). If we focus on the case where FL and RL have the same longitude axis, then there is no difference between x and z , which results in the only important parameter for the dipolar tensor $\tilde{D}_{zz} = \tilde{D}_{xx} = -1/2\tilde{D}_{yy}$.

Therefore, \tilde{d}_{yy} is an important parameter and it is the dipolar field in the y direction coming out from a cylindrical magnet when its magnetization is in the y direction. Following Derby *et. al.* [55], one can calculate the \tilde{d}_{yy} via the calculations of the magnetic field of a cylindrical magnet with radius R and thickness t at a point $\vec{r}(y, \rho = \sqrt{x^2 + z^2})$:

$$\tilde{d}_{yy}M_s^{ref} = H_y(y, \rho) = \frac{M_s^{Ref} R}{\pi(R + \rho)} \left[\beta_+ C(k_+, \gamma^2, 1, \gamma) - \beta_- C(k_-, \gamma^2, 1, \gamma) \right] \quad (4.3)$$

$$y_{\pm} = y \pm t \quad (4.4)$$

$$\beta_{\pm} = \frac{y_{\pm}}{\sqrt{y_{\pm}^2 + (\rho + R)^2}} \quad (4.5)$$

$$\gamma = \frac{R - \rho}{R + \rho} \quad (4.6)$$

$$k_{\pm} = \sqrt{\frac{y_{\pm}^2 + (R - \rho)^2}{y_{\pm}^2 + (R + \rho)^2}} \quad (4.7)$$

$$C(k_c, p, c, s) = \int_0^{\pi/2} \frac{c \cos^2 \phi + s \sin^2 \phi}{(\cos^2 \phi + p \sin^2 \phi) \sqrt{\cos^2 \phi + k_c^2 \sin^2 \phi}} d\phi \quad (4.8)$$

Note that, at $\rho = 0$, the field can be expressed as in standard textbooks formula:

$$H_y(y, 0) = \frac{M_s}{2} \left[\frac{y + t/2}{\sqrt{(y + t/2)^2 + R^2}} - \frac{y - t/2}{\sqrt{(y - t/2)^2 + R^2}} \right] \quad (4.9)$$

$$\approx \frac{M_s}{2} \frac{tR^2}{\sqrt{y^2 + R^2}} \quad \text{in the limit } t \ll R \quad (4.10)$$

Figure 4.2 shows the calculations of the fields coming out from a PMA magnet whose thickness is $t = 2nm$, at a distance $\delta = 5nm$ as a function of offset (or ρ).

- The fields are strongest near the boundaries of the RL where $Offset \approx R_{ref}$ and smallest at the center where $Offset = 0$. This explains why the effects of dipolar fields on stepped structure (they put the free magnet at $Offset=0$) proposed by Tohoku's University are small [44].

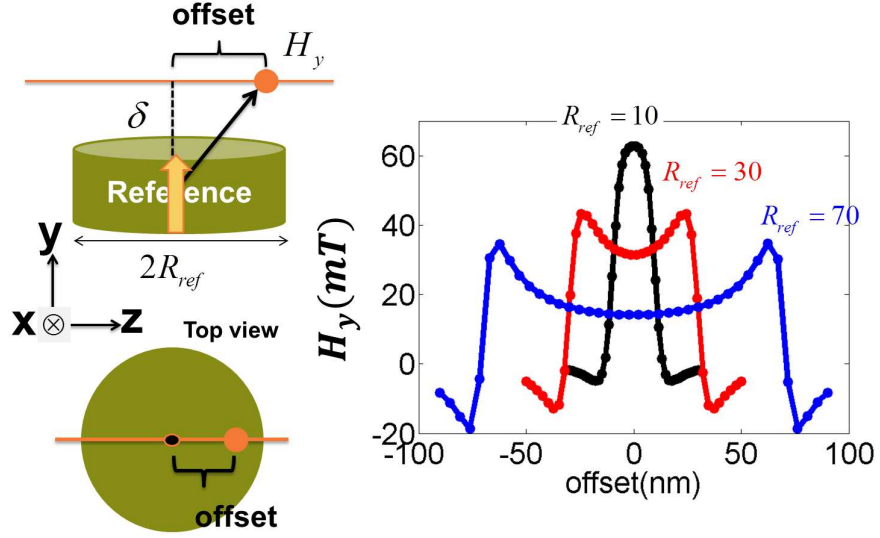


Fig. 4.2. Dipolar fields of a PMA magnet calculated by Eq.(4.3). The fields are strongest near the boundaries of the Ref magnet where $Offset \approx R_{ref}$ and smallest at the center where $Offset = 0$. Note that at $Offset = 0$, the fields can be analytically described by Eq.(4.10). In the simulation, $t = 2nm$, $\delta = 3nm$, $M_s = 10^6 A/m$.

- Note that at $Offset = 0$, the fields can be analytically described by Eq.(4.10). Also, the dipolar field increases as one reduces the magnet diameters, which explains the IBM's experiment showing the increasing of dipolar field by reducing the size of the full MTJ stack [54].

In the next section, we would like to benchmark our model with micro-magnetic simulation (OOMMF) and experiments for dipolar field between two magnets.

4.3 Benchmarking the framework

4.3.1 Compare to micromagnetic simulation: OOMMF

Now we want to validate our macro-spin approach with the micro-magnetic simulation like OOMMF. We now consider a system of two magnets RL and FL as in

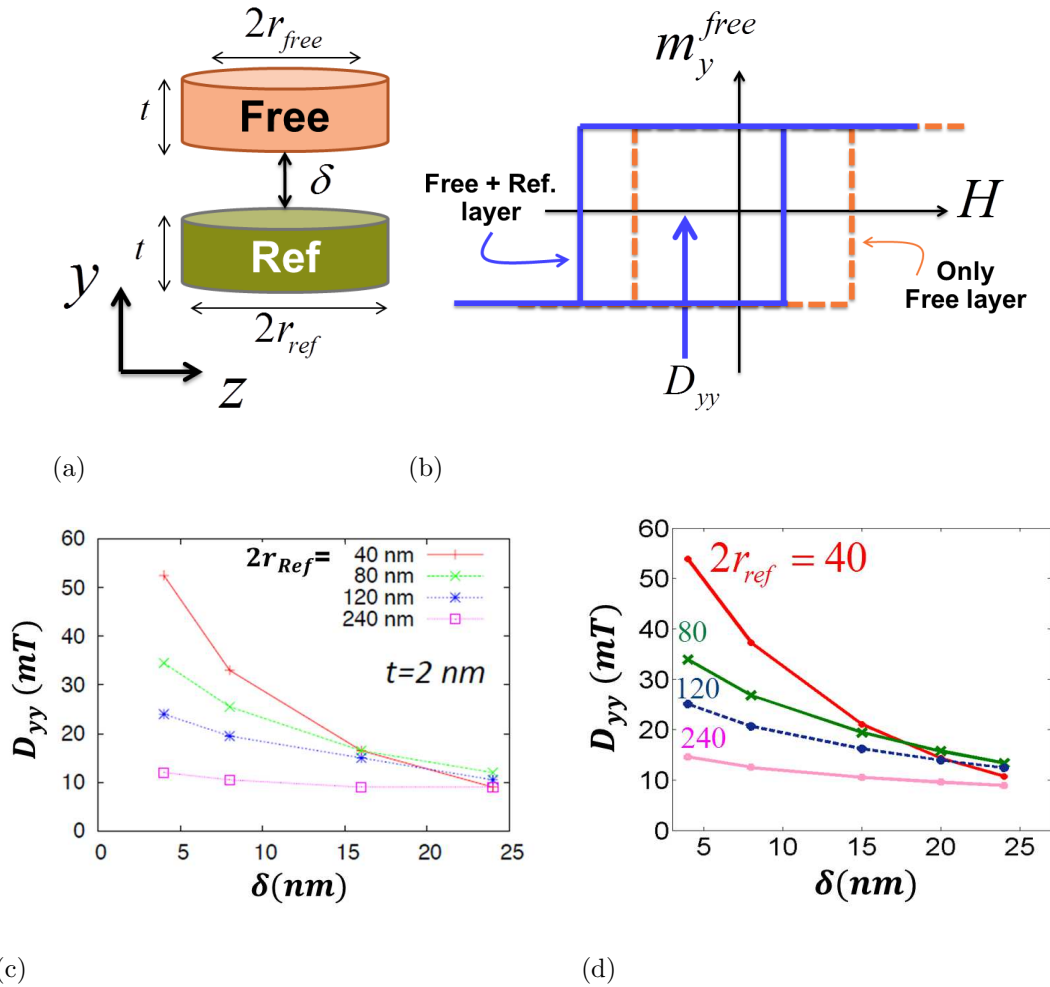


Fig. 4.3. a) A schematic setup for the calculating of the dipolar strength (D_{yy}) at Free magnet due to Reference magnet (both have the same diameters). b) D_{yy} could be measured via the shift in hysteresis of the Free magnet due to the dipolar field of Reference magnet. c) OOMMF simulations (reproduced by permission from Professor A. D. Kent at New York University) of D_{yy} as a function of diameters of Ref layer and the distances between Ref and Free layers. d) Macro-spin model calculations of D_{yy} by integrating Eq.(4.11) and using $M_s^{ref} = 0.86 \times 10^6$.

Fig.4.3(a) and would like to calculate the strength of the dipolar coupling at FL due to the RL. In OOMMF or in the experiments, this can be done by first calculating/measuring the hysteresis loop of an **isolated** FL magnet and then calculating/measuring

the shift in the hysteresis of the FL in the presence of the RL indicated in Fig.4.3(b). In our language, the shift in the hysteresis can be approximately estimated as:

$$D_{yy} = \frac{M_s^{Ref}}{V_{FL}} \int_{V_{FL}} d\vec{r}' \tilde{d}_{yy}(\vec{r}') \quad (4.11)$$

which physically is the average dipolar field at FL due to the RL. Figure 4.3(c) shows the calculations (done by A. D. Kent's group at NYU) of D_{yy} obtained via micro-magnetic simulation (OOMMF) for different diameters of the Ref layer and distances δ (noted that the $r_{free} = r_{Ref}$ in all calculations). Using the same parameters in OOMMF simulations such as $M_s^{ref} = 0.86 \times 10^6 A/m$ and the same geometric parameters, we calculated the values of D_{yy} by evaluating the Eq.(4.11) and showed the results in Fig.4.3(d).

It is clear that our simulations are in excellent agreement with the micro-magnetic simulations. Two key points are observed:

- At a given distance δ , the smaller the radius, the larger the dipolar fields. This is also one of the main issues in scaled pMTJ reported in IBM's experiment [54].
- The smaller the radius, the faster the decay of dipolar field as a function of distances. Therefore, it is very hard to eliminate the dipolar fields in scaled pMTJ even with the careful designs of SAF2 layer, simply because they are far away from the FL.

4.3.2 Compare to Tohoku's Experiments

In the conventional MTJ structures, the RL and FL normally have the same diameters. However, this may not be a good choice in terms of the dipolar field as inferred from Fig.4.2. Experimentally, it has been shown that the stepped structure in Fig.4.4 could significantly reduce the dipolar field at FL due to RL [44]. In the experimental setup (Fig.4.4), both FL and RL have the same diameters $2R = 100nm$ in the conventional structure while they have different diameters in the stepped structure $2R_{RL} = 300nm$ and $2R_{FL} = 100nm$. The strengths of the dipolar coupling were

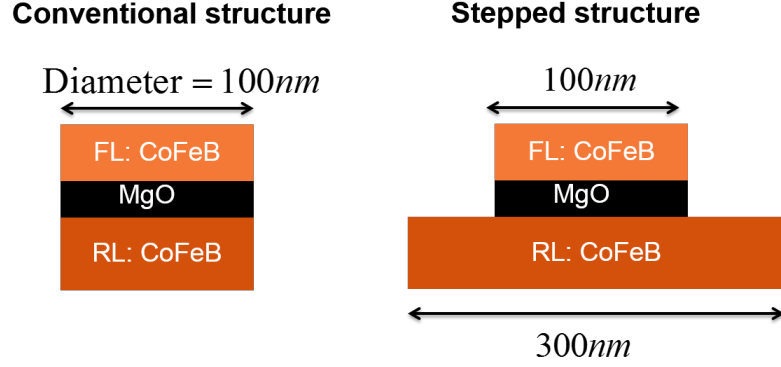


Fig. 4.4. Schematic setups for conventional and stepped structures in Tohoku's experiment [44]. $t_{ref} = 1nm$, $t_{free} = 1.7nm$, $MgO = 1nm$, $M_s^{RL} = 10^6 A/m$.

reported by measuring the shifts in the hysteresis of both stepped and conventional structures. It is clearly shown that (table 4.1) the stepped structure has much less dipolar field at the FL as compared to the conventional structure.

Physically, can we understand why stepped structures are better than conventional ones in terms of dipolar field? The answer is yes and it can simply be inferred from Fig.4.2. For a given distance δ above the RL, the dipolar fields coming out from the RL are strongest near the edges and smallest at the center (offset=0), for example:

$$H_y(\text{Offset} \approx R_{RL}) > H_y(\text{Offset} \approx 0)$$

And the total dipolar field at FL is the average dipolar field at FL, namely:

$$D_{yy} = \frac{1}{V_{RL}} \int H_y(\vec{r}) dV_{FL}$$

Therefore, if FL has the same size as RL in the conventional structure, the average dipolar field at FL should be large due to contributions from the edges, namely $H_y(\text{Offset} \approx R_{RL})$. However, in the stepped structure, most of contributions are coming from $H_y(\text{Offset} \approx 0)$ and there is no contribution of dipolar fields from the edges. Hence the dipolar field should be small in the stepped structure.

Table 4.1
Experimental data and simulation results for the shift in hysteresis of the FL (D_{yy}) for both conventional and stepped structures.

	Conventional Structure	Stepped Structure
D_{yy} : Tohoku's Experiment	$22mT$	$5mT$
D_{yy} : Theory	$20.5mT$	$4.5mT$

Using the **same** experimental parameters such as the diameters, thicknesses t_{RL} , t_{FL} , t_{MgO} and saturation magnetization M_s of both magnets, we evaluate the total dipolar fields D_{yy} at FL for both conventional and stepped structures and compare them with the experimental data. It is clear that our model is in good agreement with the experimental results as shown in table 4.1.

We then now would like to extend the results to a range of RL and FL diameters shown in Figure 4.5. Here we calculate D_{yy} as a function of RL diameters (or radius) for given sizes of FL. Here are some key observations:

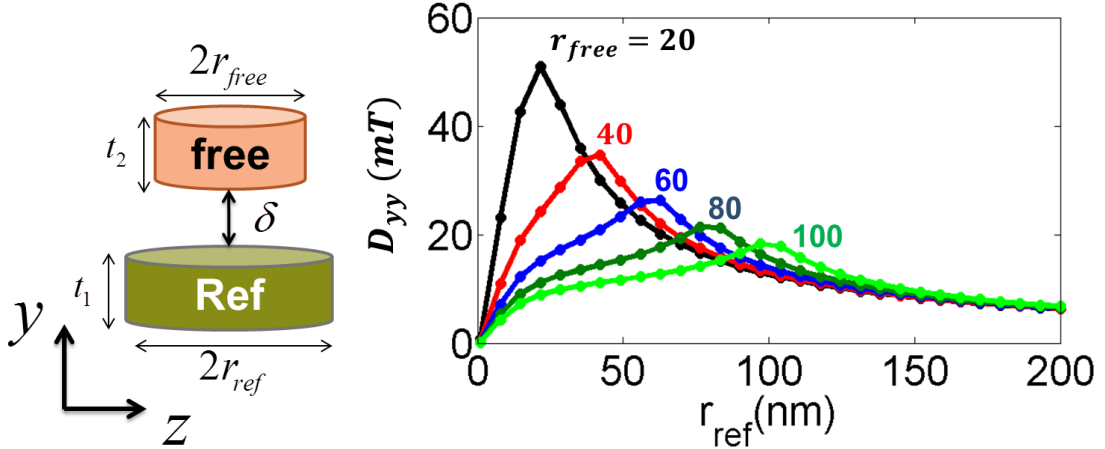


Fig. 4.5. D_{yy} : the strength of dipolar field at FL due to RL, as a function of radius of the RL and for a given size of FL. $t_{ref} = 2nm$, $t_{free} = 2nm$, $\delta = 4nm$, $M_s = 10^6 A/m$

- D_{yy} is strongest in the conventional structures where the diameters of FL and RL are equal.
- D_{yy} is small in asymmetric structures with $r_{free} < r_{ref}$ or $r_{free} > r_{ref}$. The stepped structures fall into this category.
- D_{yy} for conventional structures ($r_{free} = r_{Ref}$) increases as one reduces the sizes of FL and RL. This is one of the main difficulties in scaling MTJ devices.

4.4 Modeling dipolar fields of full MTJ stacks including Synthetic Anti-Ferromagnetic (SAF) layers

So far we have shown that dipolar couplings at FL increase dramatically as one scales down the diameter of the MTJ in Fig.4.5. One of the direct way to reduce the dipolar field is to use a material with low M_s [56]. Another common way is to use the synthetic anti-ferromagnetic (SAF) layer as mentioned in the introduction. SAF1 layer is used to reinforce the RL layer so that its magnetization can be pinned while SAF2 (which has the magnetization opposite to the one of the SAF1) is used to reduce the dipolar fields at the FL [57,58]. Basically, SAF layers are Cobalt based multi-layers such as: $[Co/Pt]$, $[Co/Pd]$ or $[Co/Ni]$ [59,60].

In this section, we would like to describe the modeling of the full pMTJ stack including the SAF layer. Fig.4.6 shows an example of a full pMTJ stack [54] where SAF1 and SAF2 consist of $[Co/Pd]_n$ multi-layers (n represents the number of repetition of the $[Co/Pd]$ layer). The SAF1 and SAF2 are separated by the Ru layer whose thickness is well chosen so that the SAF1 and SAF2 to be in the *anti-parallel* configuration due to the Ruderman-Kittel-Kasuya-Yosida (RKKY) interaction. The total dipolar field at the FL is simply the summation of all dipolar fields coming from: Ref, SAF1 and SAF2 layers. Then one of the very first questions in calculating the dipolar fields at FL is how to calculate the saturation magnetization of the *Cobalt* based magnetic multi-layers in the SAF1 and SAF2.

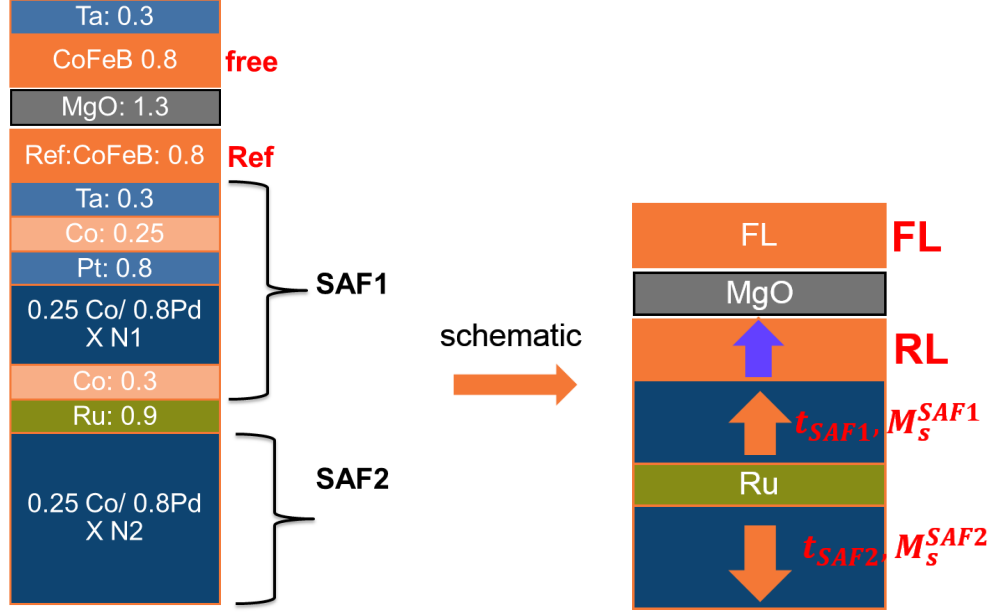


Fig. 4.6. An example of a full pMTJ stack [54] and its schematic representation. The SAF1 and SAF2 layers are $[Co/Pd]$ multi-layers where $N1$ and $N2$ represent the number of repetition of the layers. Note that the SAF1 and SAF2 are separated by the Ru layer whose thickness is well chosen so that the SAF1 and SAF2 to be in the *anti-parallel* configuration due to the Ruderman-Kittel-Kasuya-Yosida (RKKY) interaction.

Saturation magnetization of *Cobalt* based multilayers

In the full pMTJ stack (Fig.4.6) one needs to know the saturation magnetization of $[Co/X]$ layer (where X could be $Pd, Pt, Ni\dots$). Note that, even though X by itself is not a magnetic material, it could have induced magnetization when it is in contact with Co material [61,62]. Experimentally, $M_s^{[Co/X]}$ of the composite layer is measured for the entire layer. Therefore, we can also treat the composite layer $[Co/X]$ as a single magnet with an average magnetization taken from the experimental values. In some cases, we can treat the $[Co/X]$ as a single magnet having thickness $t_{Co/X} = t_{Co} + t_X$ and the average saturation magnetization $M_s^{Co/X}$ as [63]:

$$M_s^{Co/X} = \frac{M_s^{Co-bulk}t_{Co} + M_s^{X-induced}t_X}{t_{Co} + t_X} \quad (4.12)$$

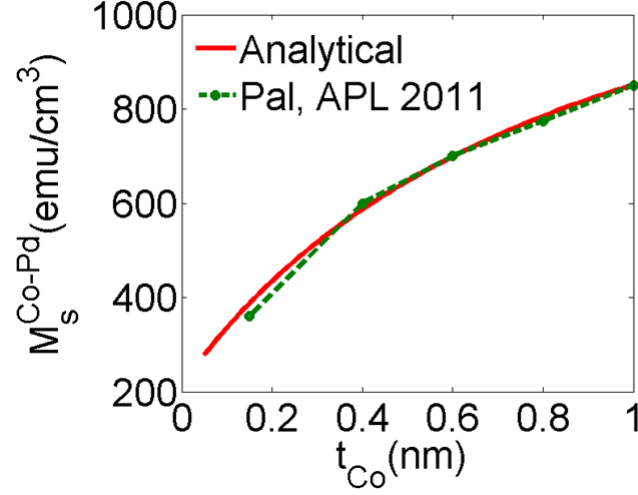


Fig. 4.7. $M_s^{Co/Pd}$ of composite $[Co(t_{Co})/Pd(0.9nm)]$ layer. The dotted circle line is the experimental data [63]. The analytical line is obtained by using Eq.(4.12) with $M_s^{Pd-induced} = 210emu/cm^3$

where $M_s^{X-induced}$ (can be measured experimentally) is the induced magnetization of X (could be non-magnetic material) when it is in contact with Co . Figure 4.7 shows the experimental data on the magnetization of $Co(t_{Co})/Pd(0.9nm)$ system as a function of t_{Co} thickness. The magnetization of the composite layer as a function of Co thickness can be well described by Eq.(4.12). In the calculations, $M_s^{Pd-induced} = 210emu/cm^3$ was taken from the experimental measurements [63].

However, it should be noticed that the M_s of $[Co/X]_n$ could depend on the number of layer as reported in [60] which is shown in Fig.4.8.

Therefore, in our simulations, we treat the multi-layer cobalt based $[Co/X]_n$ as a single magnet whose thickness is $t_{tot} = (t_{Co} + t_X) \cdot n$ and the saturation magnetization of the composite system $M_s^{[Co/X]_n}$ as a fitting parameter taken from experiment.

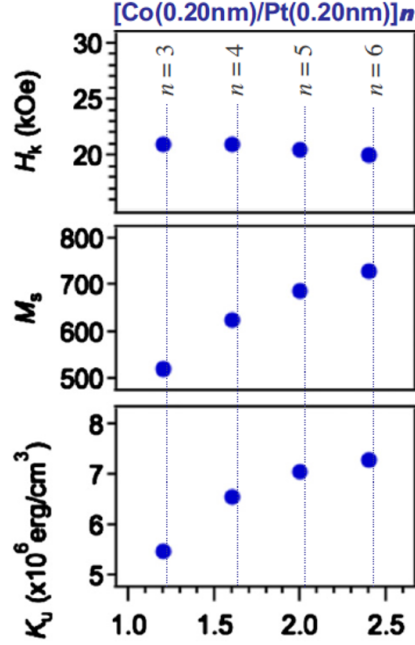


Fig. 4.8. Experimental data on the magnetic properties of composite $[Co/Pt]_n$ as a function of the repetition number n . Reprinted with permission from [60]. Copyright 2010, AIP Publishing LLC.

4.4.1 Benchmark against experiments

We now can calculate the total dipolar at FL in a full pMTJ stacking including RL, SAF1 and SAF2. Figure 4.9 shows the experimental data [54] of coercive fields H_c and the shifts in the hysteresis of the FL $H_{\text{offset}} = D_{yy}$ as a function of the diameters of a pMJ stack: $0.85 \text{ CoFeB}/1.4 \text{ MgO}/0.8 \text{ CoFeB}/0.3 \text{ Ta}/0.25 \text{ Co}/0.8 \text{ Pt}/[0.25 \text{ Co}/0.8 \text{ Pd}]_4/0.3 \text{ Co}/0.9 \text{ Ru}/[0.25 \text{ Co}/0.8 \text{ Pd}]_8$ where the thicknesses are in nm . As mentioned before, the dipolar fields increase dramatically as one reduces the diameters of the stack even in the presence of the SAF2 layer. On top of that, at small diameters, the dipolar fields are comparable to the coercive fields H_c of the FL, which means we completely lose information stored in the FL magnet. Since now the FL always points in the direction of the total dipolar fields at FL.

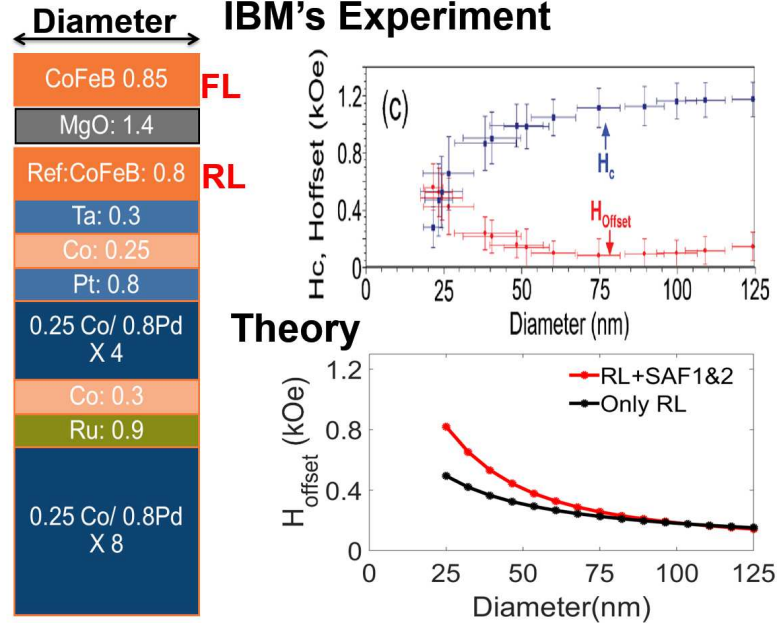


Fig. 4.9. Comparison between theory and experimental data (Reprinted with permission from [54]. Copyright 2012, AIP Publishing LLC) for the *total* dipolar fields H_{offset} at the Free layer as a function of the diameters of the stack (H_{offset} was extracted from the shifts of the hysteresis). For theoretical calculation, the black dot curve calculates the dipolar field at FL due to only the RL. Here $M_s(Co/Pt) = M_s(Co/Pd) = 0.4$, $M_s(RL) = 1$ (in the unit of $10^6 A/m$).

Using the same parameters such as geometries for each magnetic layer used in the experiment and the saturation magnetizations for composite magnetic layer $M_s[Co/Pt] = M_s[Co/Pd] = 0.4 \times 10^6 A/m$ fitted using Eq.(4.12) with $M_s^{induced} = 210 emu/cm^3$, we calculate the $H_{offset} = D_{yy}$ at the FL by summing all the dipolar field contributions of RL, SAF1 and SAF2 at the FL. Note that, in this calculation, non-magnetic materials such as *MgO*, *Ta* and *Ru* will not have any contributions and they act as spacers in the simulations. The numerical results are in good agreement with the experimental data as shown in Fig.4.9. It is also noted that, the main contributions to the dipolar fields at the FL are from the RL. At small diameters, SAF2 layer does not sufficiently cancel the total dipolar due to RL and SAF1. Since SAF2 is far away from the FL,

the dipolar fields decay much faster than the SAF1 and RL (see for example the calculations in Fig.4.3(d)). This is one of the reasons making designs of scaled pMTJ difficult.

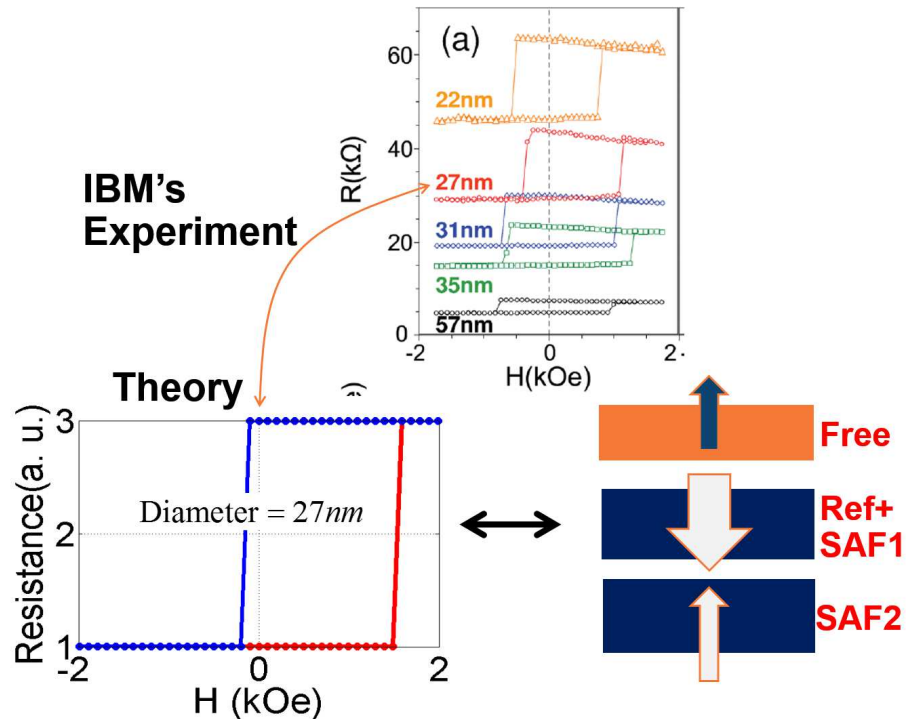


Fig. 4.10. The hysteresis shifts as a function of diameters for the structure in Fig.4.9. The theoretical calculations imply that the dipolar fields at Free layer are dominated by the RL and SAF1 layers. Reprinted with permission from [54]. Copyright 2012, AIP Publishing LLC.

The numerical simulations in Fig.4.9 agree not only with the experiment in terms of the absolute values of the shift in the hysteresis but also with the signs of the shifts. This is confirmed in the Fig.4.10 where it shows the details of the experimental hysteresis shifts of the FL for different diameters as well as the numerical simulations done by coupling the dipolar fields with coupled LLG equations. As depicted in the schematic, the results imply that the total dipolar field at FL is dominated by the contributions from the RL and SAF1 since the Free layer needs large (positive)

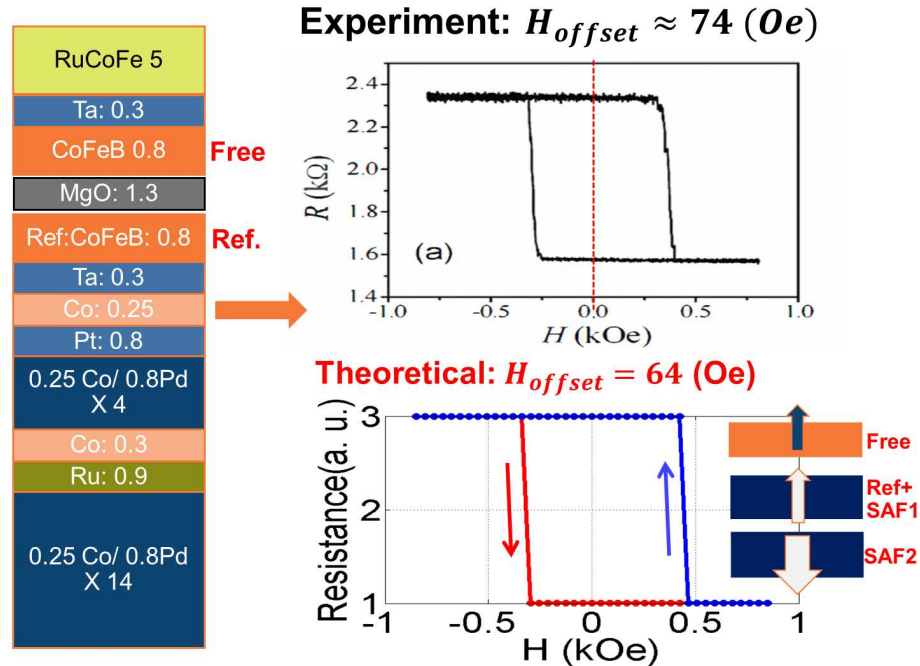


Fig. 4.11. A hysteresis of the free layer in an IBM's MTJ stack [64]. The theoretical calculations agree with experiment about the magnitude of the H_{offset} and suggest that the main contribution is from SAF2. Reprinted figure with permission from [64] Copyright 2011 by the American Physical Society.

magnetic field to be in the anti-parallel state (with the RL) and small (negative) magnetic field to be in the parallel state.

However, for another structure [64] such as the one in Fig.4.11, the dipolar field at the Free layer is dominated by the SAF2 layer where it needs larger magnetic field in order to be in the parallel states than in the anti-parallel states. Note that in this case, we have a very thick SAF2 and the device diameter is quite large (120nm).

4.5 From multi-layer model to three magnet model

Up to now, we have constructed a numerical framework to analyze the dipolar field for any given structure of a pMTJ. In this section, however, we want to know

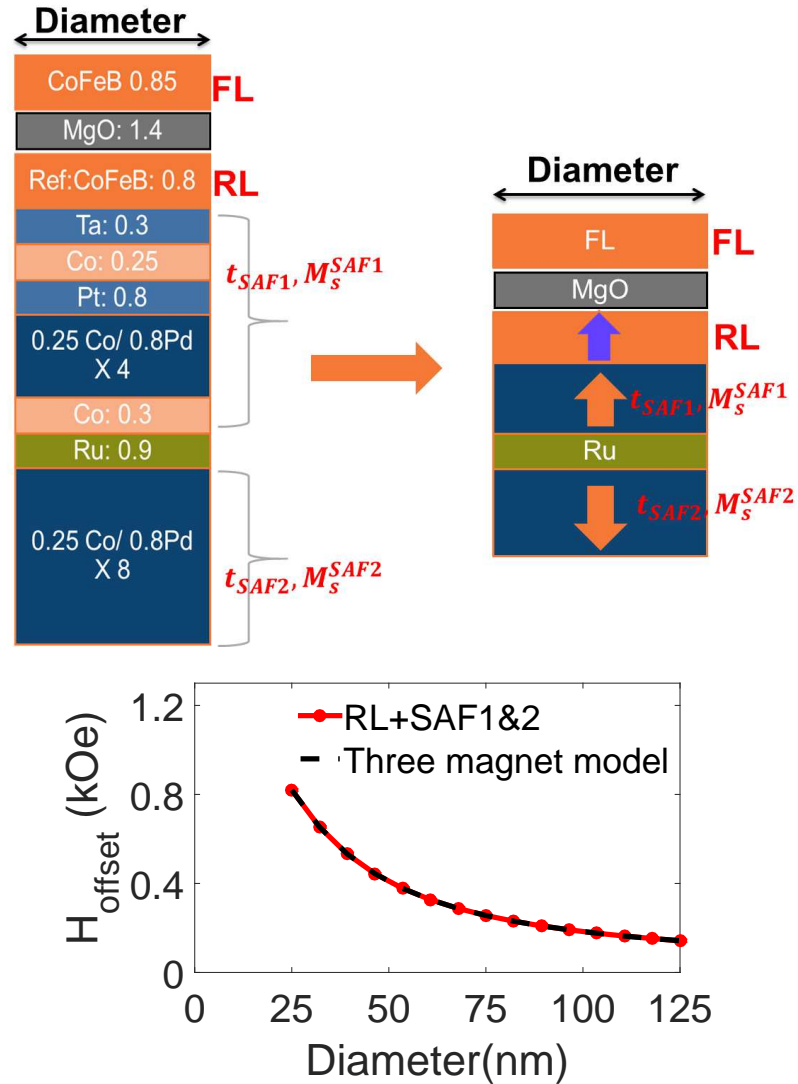


Fig. 4.12. The complex pMTJ structure can be understood in terms of a system of three magnets. The simulations for the full stack are the same as the simulations in Fig.4.9.

what are the key parameters that govern the dipolar fields at the FL because this kind of understanding will help in designing the stray fields in pMTJ at various technology nodes. We start with an observation that, the complex pMTJ can be simplified into a system of just three magnets: RL, SAF1 and SAF2 where SAF1 and SAF2 are not multi-layer magnets but instead are just one-layer *fictitious* magnets depicted in

Fig.4.12. In the three magnet model, the thickness of the fictitious SAF1 or SAF2 magnet is simply the total thickness of the original multi-layer SAF1 and SAF2. The magnetization M_s^{SAF} , on the other hand, could be calculated by equating the average dipolar field at FL due to the multilayer SAF to the average dipolar field at FL due to the fictitious magnet whose thickness is t_{SAF} :

$$\sum_{layer Y} M_s(Y) D_{yy}^{Y,FL}(t_Y) = M_s^{SAF} D_{yy}^{SAF}(t = t_{SAF}) \quad (4.13)$$

here the summation is evaluated for all layers within the *SAF*. Note that each layer *Y* could have difference $M_s(Y)$.

Fig.4.12 confirms the validity of the three magnet model by recalculating the H_{offset} for the experiments shown in Fig.4.9. The model agrees well with the simulations for the complex multi-layer pMTJ.

Given the validity of the model of three magnets, we now can identify the key parameters governing the dipolar field in pMTJ. Clearly, the model suggests that the key parameters are thicknesses: $t_{RL}, t_{SAF1}, t_{SAF2}, R$ (geometry) and saturation magnetizations of RL, SAF1 and SAF2 layers $M_s^{RL}, M_s^{SAF1}, M_s^{SAF2}$ (material). However, even with the simplification used in the three-magnet model, it is still very hard to analytically calculate the average dipolar field at the FL. Therefore, instead of averaging the dipolar fields at the FL, we only calculate the dipolar fields at the center of the FL magnets, which can be evaluated analytically. Note that, the fields at $\vec{r} = \{x = 0, y, z = 0\}$ of a cylindrical magnet:

$$H_y^0(y, t) = \frac{M_s}{2} \left[\frac{y}{\sqrt{y^2 + R^2}} - \frac{y - t}{\sqrt{(y - t)^2 + R^2}} \right] \quad (4.14)$$

Note that y is the distance from top edge of the magnet. Therefore, *for a very crude approximation*, the total dipolar field at FL can be approximated as the total dipolar field at the center of the FL coming from the RL, SAF1 and SAF2 layers:

$$H_{Offset}^0 = D_{yy} \approx H_y^0(y_{RL}, t_{RL}) + H_y^0(y_{SAF1}, t_{SAF1}) - H_y^0(y_{SAF2}, t_{SAF2}) \quad (4.15)$$

where y_{RL}, y_{SAF1} and y_{SAF2} are the distances from the top edges of RL, SAF1 and SAF2 layers to the center position of the FL respectively.

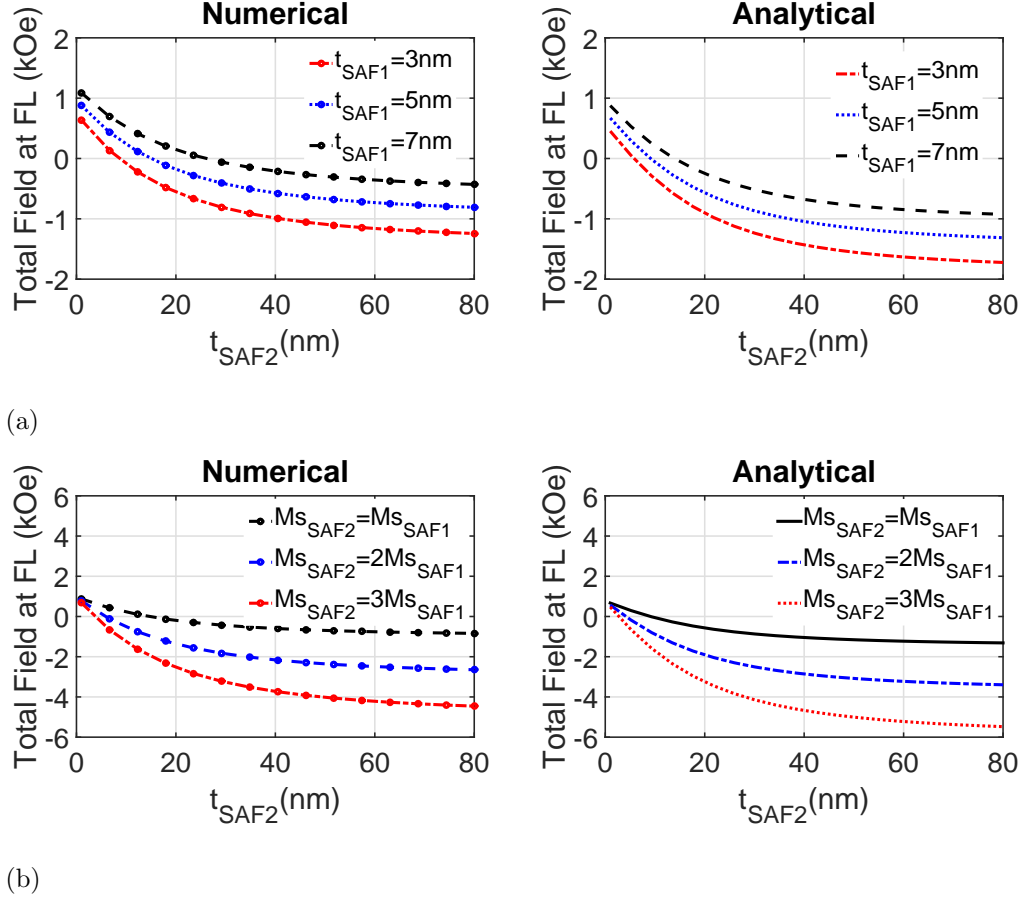


Fig. 4.13. Numerical (averaging the dipolar field over the FL) and analytical (only dipolar field at the center of FL) simulations for the total field at the FL: a) Geometry factors. The parameters used in the simulations: diameter of the pMTJ stack = $55nm$, $M_s^{RL} = 10^6 A/m$, $M_s^{SAF1} = M_s^{SAF2} = 0.5 \times 10^6 A/m$, $t_{MgO} = t_{FL} = 1nm$, $t_{Ru} = 0.9nm$. b) Material factors. The parameters used in the simulations: diameter of the pMTJ stack = $55nm$, $M_s^{RL} = 10^6 A/m$, $M_s^{SAF1} = 0.5 \times 10^6 A/m$, $t_{SAF1} = 5nm$, $t_{MgO} = t_{FL} = 1nm$, $t_{Ru} = 0.9nm$. In both a) and b) the analytical results are obtained via Eq.(4.15) and Eq.(4.14)

It turns out that the analytical equation (Eq.(4.15)) or total dipolar field at the center of FL, *qualitatively* captures the physics and the behavior of the total **averaging** dipolar field at the FL (numerical). In particular, it captures the behaviors of the dipolar field as a function of geometry and material parameters as shown in

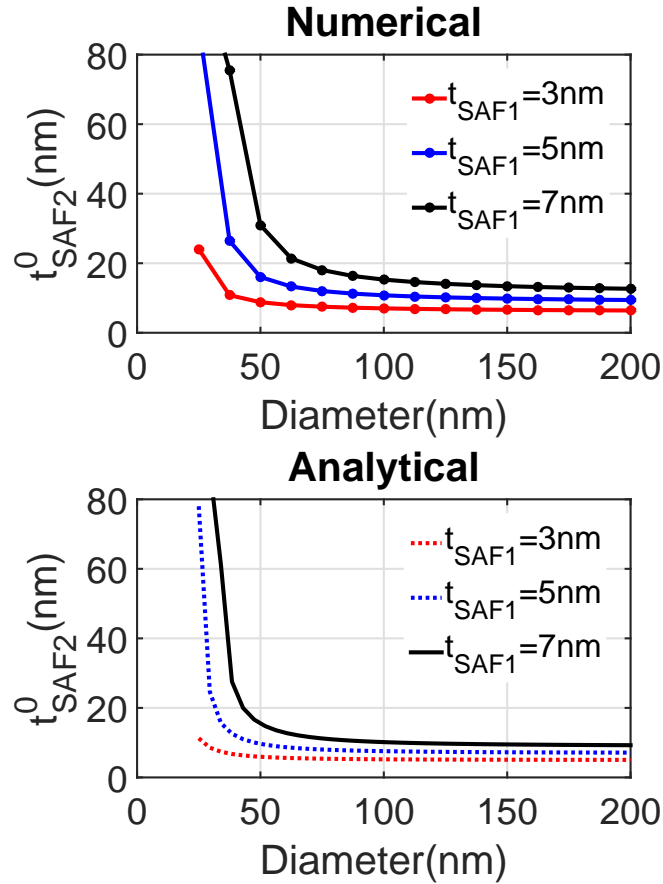


Fig. 4.14. Numerical (averaging the dipolar field over the FL) and analytical (only dipolar field at the center of FL) calculations for the critical thickness of SAF2, t_{SAF2}^0 (needed in order to have the total zero dipolar field at FL) as a function of the diameters of the pMTJ for different values of SAF1 thicknesses. Here $M_s^{SAF1} = M_s^{SAF2} = 0.5 \times 10^6 A/m$ and $M_s^{RL} = 10^6 A/m$, $t_{RL} = t_{LF} = t_{MgO} = 1nm$. The analytical results are obtained via Eq.(4.15) and Eq.(4.14).

Fig.4.13(a) and Fig.4.13(b) respectively. It also captures the behavior of dipolar field as a function of diameter as shown in Fig.4.14.

In Fig.4.13(a), the total fields at FL are calculated as a function of the geometric parameters such as t_{SAF1} and t_{SAF2} . Both the numerical and analytical results capture the fact that a small increase in the thickness of SAF1 will result in a very thick SAF2 layer to compensate the dipolar field at FL. On the other hand, Fig.4.13(b) shows

the calculations of the total fields at FL as a function of the material parameters such as M_s^{SAF1} and M_s^{SAF2} . The analytical results qualitatively agree with the numerical simulations and directly imply the dependence of the dipolar field on material choice.

Fig.4.14 shows the numerical calculations of the critical thickness of SAF2 t_{SAF2}^0 needed in order to have zero total field at the FL as a function of the diameters of the pMTJ stack. In order to calculate t_{SAF2}^0 , for a given diameter and thickness of t_{SAF1} , many different values of t_{SAF2} have been tried before finding out the one that gives the total zero dipolar field at FL. The analytical calculations qualitatively agree with the numerical simulations which in turns shed light on the dependence of the dipolar field on diameters. This is helpful in designing scaled pMTJ.

4.6 Summary

In this chapter:

- We have created an experimentally validated tool that can calculate the stray fields in pMTJ stack for arbitrary geometries and materials.
- This tool can be used to design devices having small dipolar fields so that one can have symmetric retention time for various technology nodes.
- We have introduced the three-magnet model that can be used to study the complex pMTJ stacks. On top of that, we have provided a simple analytical equation that qualitatively captures the (complex) physics of dipolar fields in pMTJ. We, therefore, identify the key parameters and their dependence on dipolar fields.
- The model can be coupled with spin transport and magnet dynamics to find out the impacts of stray fields on switching dynamics.

5. SPIN SWITCH OSCILLATOR: A NEW APPROACH BASED ON GAIN AND FEEDBACK

Copyright 2014 IEEE. Reprinted, with permission, from [14]. Most of the material in this chapter have been extracted verbatim from the paper: "The spin switch oscillator: A new approach based on gain and feedback", Vinh Diep and Supriyo Datta, 72nd Annual Device Research Conference (DRC), 2014.

5.1 Motivation and Key Results

Since devices with gain and directionality can be used to build oscillators, in this chapter, we will describe a spin switch oscillator based on the standard principle of incorporating feedback into a device with gain.

The traditional spin transfer nano-oscillator (STNO) utilizes spin current as an anti-damping mechanism to cancel the damping related to the motion of magnet to generate persistent oscillations of nano-magnets. However, at present STNO has very low output power ($\ll \mu W$) and usually requires external magnet field to operate [65–67]. Here, we propose a new kind of **nano**-oscillator based on the standard principle of incorporating feedback into a device with gain, which should exhibit a high tunable output power ($0-30\mu W$) without external magnetic fields. The gain is provided by the recently proposed spin switch (SS) device [7] which combines a Giant Spin Hall Effect (GSHE)-based Write device and a magnetic tunnel junction (MTJ)-based Read device in a unique configuration that provides a transistor-like electrical isolation between input and output.

Fig.5.1(a) and Fig.5.1(b) show the schematic and basic principle operation of a spin switch oscillator (SSO): input voltage $V_{in} > V_{th}$ (V_{th} is a threshold voltage)

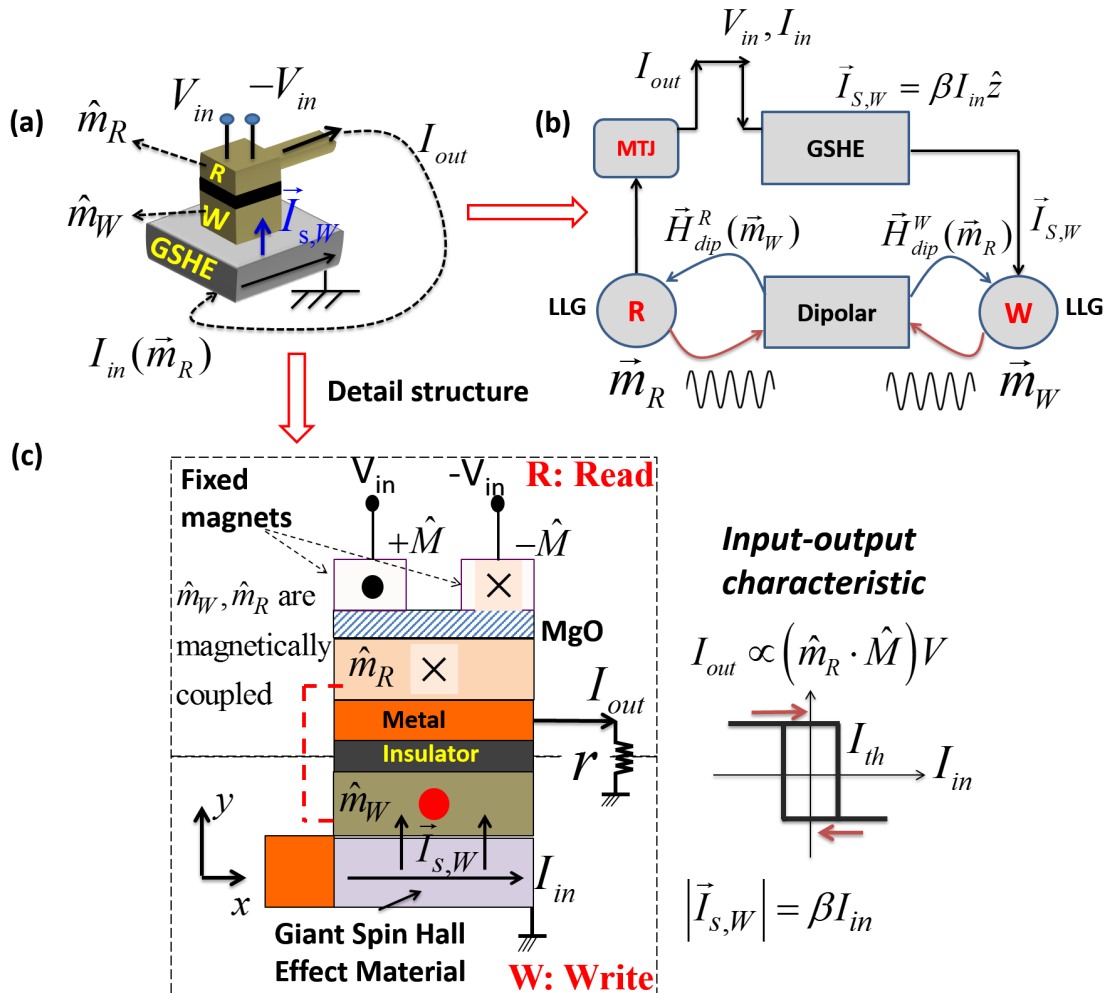


Fig. 5.1. (a) The schematic and (b) the operational principle of Spin Switch Oscillator (SSO) is similar to the feedback oscillator: for a given voltage V_{in} , input magnet \hat{m}_R gives rise to the charge current $I_{in} \sim m_{R,z} V_{in}$ (z is the easy axis) and the amplified spin current $\vec{I}_{s,W}$ forces the output \hat{m}_W to be parallel to $m_{R,z} \hat{z}$. Because of dipolar coupling, \hat{m}_R wants to anti-parallel to \hat{m}_W . As a result, there are no stable configurations in SSO. When oscillation occurs, both \hat{m}_W and \hat{m}_R will move in-phase (Barkhausen criterion). (c) Detailed structure of spin switch, adapted from [7], and it behaves as an (hysteresis) inverter. Copyright 2014 IEEE. Reprinted, with permission, from [14].

and magnet direction \hat{m}_R will give rise to a charge current I_{out} which becomes the

input current to the giant spin hall effect (GSHE) $I_{in} \sim \hat{m}_R \cdot \hat{M} V_{in}$ (where \hat{M} is the direction of fix magnet in the MTJ stack) which in turns results in a spin current $\vec{I}_{s,W} = \beta I_{in} \hat{z}$ discussed in previous chapters. This spin current forces the output \hat{m}_W of Write unit (W) to be parallel to $m_{R,z} \hat{z}$ (\hat{z} is easy axis). Because of dipolar coupling fields, $\vec{H}_{dip}^W, \vec{H}_{dip}^R$, \hat{m}_R want to anti-parallel to \hat{m}_W . As a result, there are no stable configurations in SSO. Oscillation can occur when both \hat{m}_W and \hat{m}_R move in-phase in accordance with the textbook Barkhausen criterion for oscillation in feedback circuit. Fig.5.1(c) shows the physical structure of SS (adapted from [7]) and its input-output characteristic. The SS consists of a Write (W) unit and a Read (R) unit with free \hat{m}_R, \hat{m}_W magnetic layers coupled via dipolar coupling. This setup allows information to propagate from the Write to the Read unit while maintaining their electrical isolation. The threshold current/voltage needed to drive the Write unit were estimated in previous study [7] : $I_{th} \sim 30\mu A, V_{th} \sim 150mV$ for magnets with volume $V_W = 80nm \times 110nm \times 2nm$.

Our objective in this chapter is to establish the operational properties of SSO based on numerical and analytical results.

5.2 Modeling spin switch oscillator

We start with the coupled LLG equations, Eq.(3.1) describing the SS mentioned in chapter 3 (which I re-write here for the purpose of clarity):

$$\begin{aligned}
(1 + \alpha_W^2) \frac{d\hat{m}_W}{dt} &= -\gamma \hat{m}_W \times \vec{H}_W(\hat{m}_W, \hat{m}_R) - \alpha_W \gamma \hat{m}_W \times \hat{m}_W \times \vec{H}_W(\hat{m}_W, \hat{m}_R) \\
&\quad - \hat{m}_W \times \hat{m}_W \times \frac{\hat{I}_s}{qM_s^W V_W} + \alpha_W \hat{m}_W \times \frac{\hat{I}_s}{qM_s^W V_W} \\
(1 + \alpha_R^2) \frac{d\hat{m}_R}{dt} &= -\gamma \hat{m}_R \times \vec{H}_R(\hat{m}_W, \hat{m}_R) - \alpha_R \gamma \hat{m}_R \times \hat{m}_R \times \vec{H}_R(\hat{m}_W, \hat{m}_R)
\end{aligned} \tag{5.1}$$

where we use the fields as in Eq.(5.2) (same as Eq.(3.2) and Eq.(3.3)):

$$\begin{aligned}
H_W &= \begin{bmatrix} 0 & 0 & 0 \\ 0 & -H_d^W & 0 \\ 0 & 0 & H_c^W \end{bmatrix} \begin{bmatrix} m_x^W \\ m_y^W \\ m_z^W \end{bmatrix} + \frac{V_R}{V_W} M_s^R \begin{bmatrix} D_{xx} & 0 & 0 \\ 0 & D_{yy} & D_{yz} \\ 0 & D_{yz} & D_{zz} \end{bmatrix} \begin{bmatrix} m_x^R \\ m_y^R \\ m_z^R \end{bmatrix} \\
H_R &= \begin{bmatrix} 0 & 0 & 0 \\ 0 & -H_d^R & 0 \\ 0 & 0 & H_c^R \end{bmatrix} \begin{bmatrix} m_x^R \\ m_y^R \\ m_z^R \end{bmatrix} + M_s^W \begin{bmatrix} D_{xx} & 0 & 0 \\ 0 & D_{yy} & D_{yz} \\ 0 & D_{yz} & D_{zz} \end{bmatrix} \begin{bmatrix} m_x^W \\ m_y^W \\ m_z^W \end{bmatrix}
\end{aligned} \tag{5.2}$$

which could be written in the dimensionless variables:

$$\begin{aligned}
\frac{d\hat{m}_W}{d\tau} &= -\hat{m}_W \times \vec{h}_W - \alpha_W \hat{m}_W \times \hat{m}_W \times \vec{h}_W \\
&\quad - \hat{m}_W \times \hat{m}_W \times \vec{i}_{s,W} + \alpha_W \hat{m}_W \times \vec{i}_{s,W} \\
\frac{1 + \alpha_R^2}{1 + \alpha_W^2} \frac{d\hat{m}_R}{d\tau} &= -\hat{m}_R \times \vec{h}_R - \alpha_R \hat{m}_R \times \hat{m}_R \times \vec{h}_R
\end{aligned} \tag{5.3}$$

where we normalized the fields and time as in:

$$\tau = (\gamma\mu_0 H_k t) / (1 + \alpha_W^2); \quad \vec{h}_{W,R} = \vec{H}_{W,R} / H_k$$

The dipolar tensor and demagnetization fields can be calculated via Eq.(3.15) and Eq.(3.16).

5.2.1 Oscillator: parallel or anti-parallel?

GSHE block: parallel

Using the coupled LLG Eq.(5.3), one can now numerically analyze the SSO. First, we would like to understand the role of the GSHE block which acts as gain in the feedback oscillator. Fig.5.2 shows the simulation results of the states of \hat{m}_R and \hat{m}_W as a function of time when we turn on the voltage $V_{in} > V_{th}$ but "disconnect" the dipolar coupling between \hat{m}_W and \hat{m}_R . This can be done by setting the dipolar tensor $[D] = [0]_{3 \times 3}$ in Eq.(5.2). Starting from any initial configuration of $\{\hat{m}_W, \hat{m}_R\}$, one can see that the final states are always parallel states. On top of that, the \hat{m}_W wants to

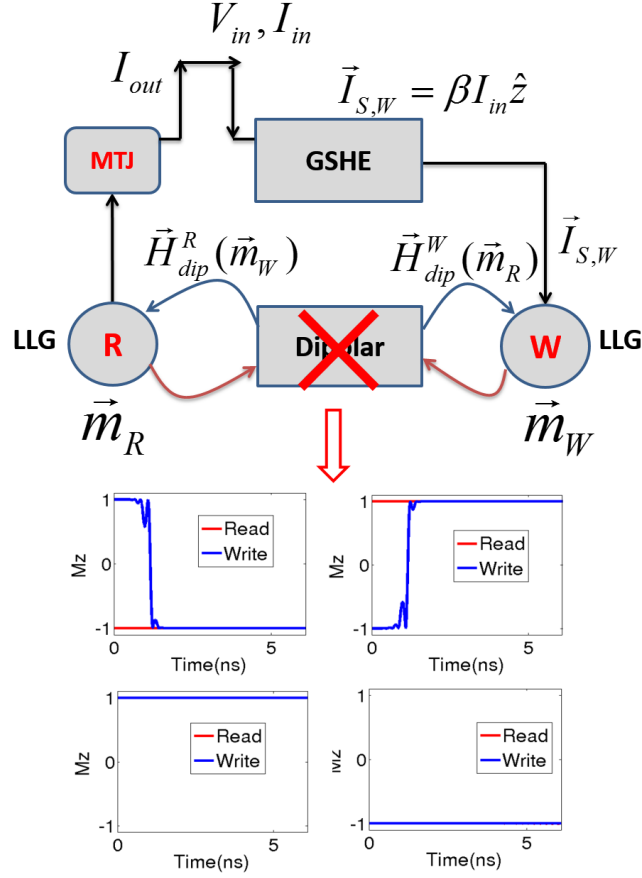


Fig. 5.2. The role of GSHE block in SSO: \hat{m}_W wants to be parallel to \hat{m}_R

follow the \hat{m}_R state. This can be easily understood in the sense that the spin current $\vec{I}_{s,W}$ that goes into the LLG block for W magnets carries the direction of \hat{m}_R [7]:

$$\hat{I}_{s,W} = \beta I_{in} \hat{z} = \beta \frac{V_{in} P m_z^R}{1 + G r_{gshe}} \quad (5.4)$$

where $P = (G_P - G_{AP})/G$ is the polarization and $G = (G_P + G_{AP})$ is the total conduction of the MTJ. r_{gshe} is the resistance of the GSHE material. Since the spin current acting on \hat{m}_W is polarized in the direction of m_z^R , $\vec{I}_{s,W} \sim m_z^R$, the W magnet wants to follow the R magnet.

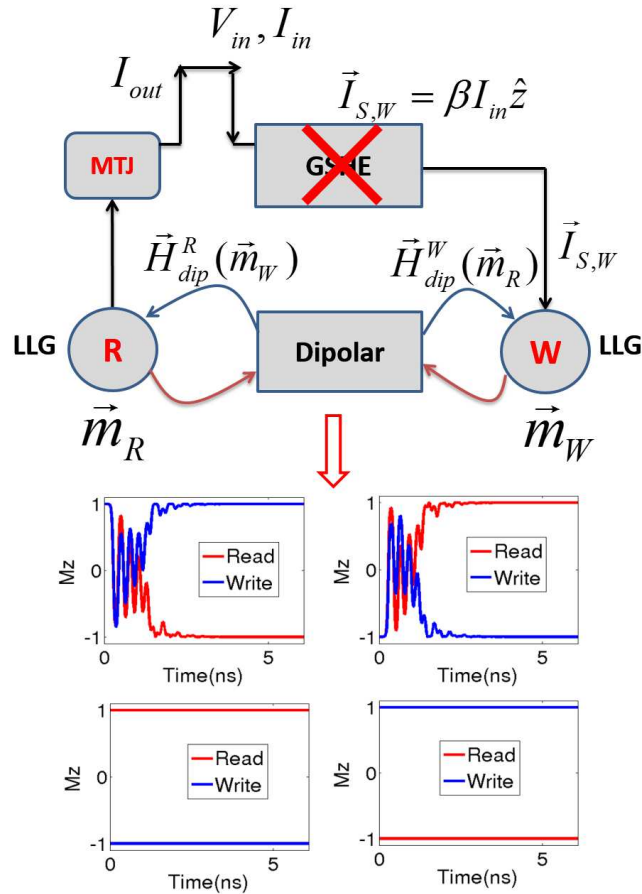


Fig. 5.3. The role of dipolar coupling block in SSO: \hat{m}_R and \hat{m}_W want to be in anti-parallel states.

Dipolar coupling block: anti-parallel

On the other hand, as shown in Fig. 5.3, the role of the dipolar coupling block is just opposite to the role of the GSHE block in the sense that both \hat{m}_R and \hat{m}_W want to be in anti-parallel states. This can be done by turning off the GSHE block via setting the spin current $\vec{I}_{s,W} = 0$ in the coupled LLG equation (Eq.(5.3)). This can be justified in the sense that dipolar coupling between in-plane magnets wants them to be anti-parallel states, provided that they are stacked along their smallest

dimension (thickness of the magnets). This way of stacking makes the anti-parallel states lower energy than the parallel states.

5.2.2 Spin Switch Oscillator

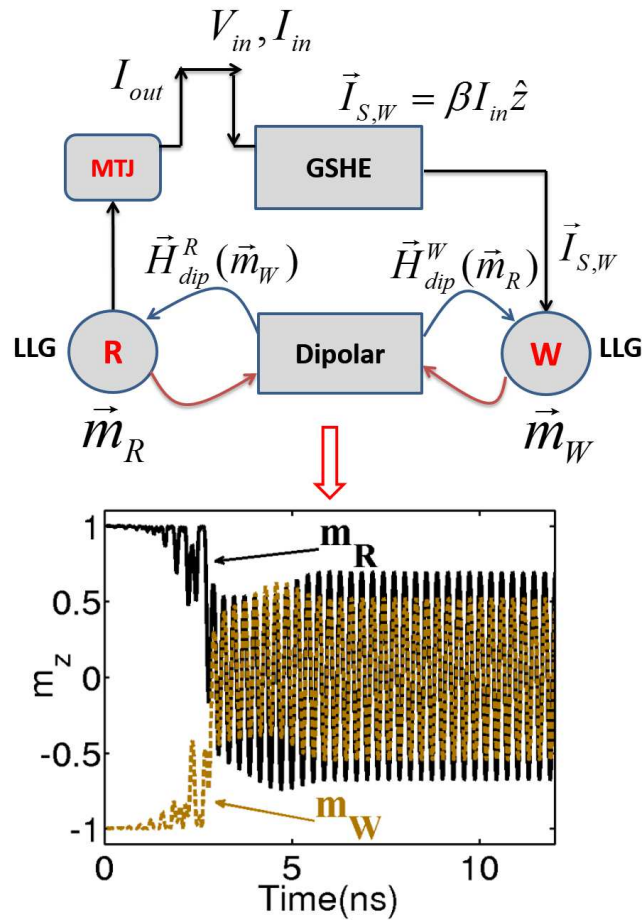


Fig. 5.4. By combining the GSHE and Dipolar block, one can obtain the oscillation of \hat{m}_W and \hat{m}_R magnets. Note that both magnets are moving in-phase.

In the previous sections, we mentioned that the GSHE block wants \hat{m}_W and \hat{m}_R to be in *parallel* states while the dipolar coupling block wants \hat{m}_W and \hat{m}_R to be in *anti-parallel* states. As a result, one can achieve the spin switch oscillator by simply

turning on both GSHE and dipolar coupling blocks. Fig.5.4 shows the oscillation of both \hat{m}_W and \hat{m}_R by solving the coupled LLG equations using the dipolar tensor calculated for two magnets having dimensions: $80nm \times 2nm \times 110nm$ for Read and $90nm \times 2nm \times 130nm$ for Write. They are stacked vertically and the distance from edge to edge between two magnets is $\delta = 10nm$. In this simulation, we assume the switching fields of both magnets are the same: $H_c^W = H_c^R = 10mT$ [68] and $M_s^W = M_s^R = 10^6 A/m$. This gives rise to the following dipolar tensor value (in the unit of H_c):

$$[D]M_s/H_c = \begin{bmatrix} -2.1 & 0 & 0 \\ 0 & -3.4 & 0.47 \\ 0 & 0.47 & -1.3 \end{bmatrix} \quad (5.5)$$

Next, we would like to argue that, the main components responsible for the oscillations are d_{xx} and d_{zz} . In other words, one can always approximate:

$$[D]M_s/H_c = \begin{bmatrix} -2.1 & 0 & 0 \\ 0 & 0 & 0 \\ 0 & 0 & -1.3 \end{bmatrix} \quad (5.6)$$

In Fig.5.5, we show the oscillation patterns of SSO for different values of the dipolar tensor. As one can see, using the full dipolar tensor as in Eq.(5.5) or using just d_{xx} and d_{zz} as in Fig.5.5(b), the results are almost identical. However, there will be no oscillations if one sets $d_{xx} = 0$ in the dipolar tensor as in Fig.5.5(c). Therefore, we would like to analytically derive frequency of the SSO based on the dipolar tensor having d_{xx} and d_{zz} only.

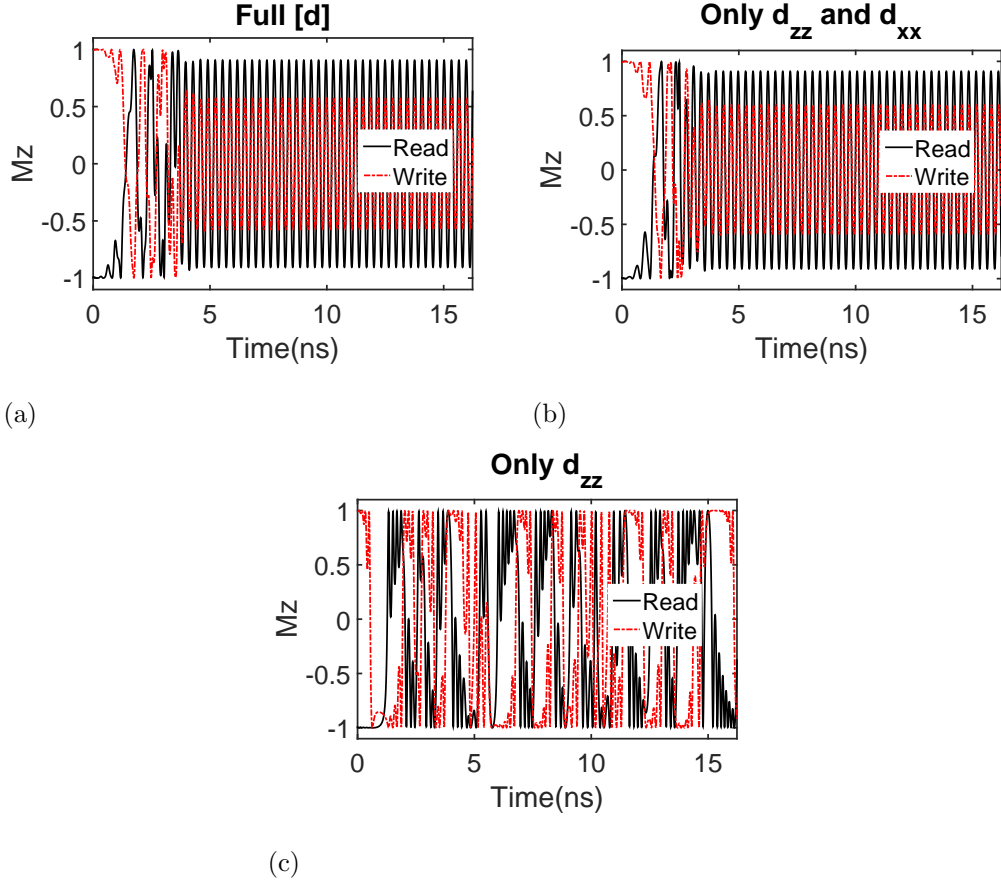


Fig. 5.5. SSO oscillators for different values of dipolar tensors.(a) Full dipolar tensor as in Eq.(5.5). (b) Only d_{xx} and d_{zz} are presented in the D tensor and (c) Only d_{zz} is presented in the D tensor.

5.3 SSO frequency: analytical model

In this section, we want to derive the analytical expressions for the frequency of SSO. From now on, we simplify the notations as in the following: $\hat{m}_W = \hat{W}$, $\hat{m}_R = \hat{R}$. Therefore, the coupled LLG for Read and Write magnets:

$$\begin{aligned} d\hat{W}/d\tau &= -\hat{W} \times \hat{h}_W - \alpha \times \hat{W} \times \hat{W} \times \hat{h}_W - \hat{W} \times \hat{W} \times \vec{i}_s + \alpha \hat{W} \times \vec{i}_s \\ d\hat{R}/d\tau &= -\hat{R} \times \hat{h}_R - \alpha \times \hat{R} \times \hat{R} \times \hat{h}_R \end{aligned} \quad (5.7)$$

Since there are only d_{xx} and d_{zz} , the fields will be:

$$\hat{h}_W = \begin{bmatrix} d_{xx}R_x \\ -h_dW_y \\ W_z + d_{zz}R_z \end{bmatrix} \quad \hat{h}_R = \begin{bmatrix} V_{rw}d_{xx}W_x \\ -h_dR_y \\ R_z + V_{rw}d_{zz}W_z \end{bmatrix} \quad (5.8)$$

where $V_{rw} = V_R/V_W$ because we assume $M_s^R = M_s^W$. It is convenient to write the LLG in the spherical coordinates:

$$\begin{aligned} W_x &= \sin(\theta_W) \cos(\varphi_W) & R_x &= \sin(\theta_R) \cos(\varphi_R) \\ W_y &= \sin(\theta_W) \sin(\varphi_W) & R_y &= \sin(\theta_R) \sin(\varphi_R) \\ W_z &= \cos(\theta_W) & R_z &= \cos(\theta_R) \end{aligned} \quad (5.9)$$

We end up the LLG equation for $\theta_{W,R}$ and $\varphi_{R,W}$

$$\begin{aligned} \frac{d\theta_W}{d\tau} &= -\sin(\theta_W) \cos(\varphi_W) \sin(\varphi_W) h_d - \sin(\varphi_W) \sin(\theta_R) \cos(\varphi_R) V_{rw} d_{xx} \\ &\quad - \alpha \sin(\theta_W) \sin(\varphi_W)^2 \cos(\theta_W) h_d - \sin(\theta_W) \cos(\theta_R) V_{rw} d_{zz} \\ &\quad + \alpha \left[\cos(\varphi_W) \cos(\theta_W) \sin(\theta_R) \cos(\varphi_R) V_{rw} d_{xx} - \sin(\theta_W) \cos(\theta_W) \right] \\ &\quad - \sin(\theta_W) \cos(\theta_R) i_z \end{aligned} \quad (5.10)$$

$$\begin{aligned} \frac{d\varphi_W}{d\tau} &= \cos(\theta_W) \left[h_d \sin^2(\varphi_W) + 1 \right] + \cos(\theta_R) V_{rw} d_{zz} \\ &\quad - \frac{\cos(\theta_W) \cos(\varphi_W) \sin(\theta_R) \cos(\varphi_R) V_{rw} d_{xx}}{\sin(\theta_W)} - \alpha h_d \sin(\varphi_W) \cos(\varphi_W) \\ &\quad - \frac{\alpha V_{rw} d_{xx} \sin(\theta_R) \cos(\varphi_R) \sin(\varphi_W)}{\sin(\theta_W)} - \cos(\theta_R) \alpha i_z \end{aligned}$$

Similarly one can write the equation for $d\theta_R/d\tau$ and $d\varphi_R/d\tau$ by replacing doing $W \rightarrow R, R \rightarrow W, i_z = 0$ and $V_{rw} = 1$ in the Eq.(5.10). However, we further assume that the demagnetization fields are the dominant fields, e.g. $h_d \gg d_{xx}, d_{zz}$. Since $i_z \approx \alpha h_d/2$, we can ignore the αi_z term in the $d\varphi/d\tau$. On top of that, we assume that

when oscillation occurs, both \hat{m}_R and \hat{m}_W will move in phase (Barkhausen's criteria) which means $d\theta_W/d\tau = d\theta_R/d\tau$ and $d\varphi_W/d\tau = d\varphi_R/d\tau$, leading to the following:

$$\begin{aligned}\frac{d\theta}{d\tau} &\approx -\sin(\theta)\cos(\varphi)\sin(\varphi)h_d - \alpha\sin(\theta)\sin(\varphi)^2\cos(\theta)h_d \\ &\quad - \sin(\theta)\cos(\theta)(V_{rw}d_{zz} + i_z) \\ \frac{d\varphi}{d\tau} &\approx \cos(\theta)\left[h_d\sin^2(\varphi) + 1\right] + \cos(\theta)V_{rw}d_{zz} \\ &\quad + \cos(\theta)\cos(\varphi)\cos(\varphi)V_{rw}d_{xx} - \alpha h_d\sin(\varphi)\cos(\varphi)\end{aligned}\tag{5.11}$$

here we use the fact that $\theta_W = \theta_R = \theta$ and $\varphi = \varphi_W = \varphi_R + \pi$ in Eq.(5.10). Next, we assume that the magnets are moving in-phase with a very small φ , then $\cos(\varphi)^2 = 1 - \sin^2(\varphi) \approx 1$. Therefore, the simplified LLG equation for the oscillator is:

$$\begin{aligned}\frac{d\theta}{d\tau} &\approx -\sin(\theta)\cos(\varphi)\sin(\varphi)h_d - \sin(\theta)\cos(\theta)(V_{rw}d_{zz} + i_z) \\ \frac{d\varphi}{d\tau} &\approx \cos(\theta)\left[h_d\sin^2(\varphi) + 1\right] + \cos(\theta)V_{rw}(d_{xx} + d_{zz}) - \alpha h_d\sin(\varphi)\cos(\varphi)\end{aligned}\tag{5.12}$$

Using $\sin(\varphi) \approx \varphi$, Eq.(5.12) becomes:

$$\begin{aligned}\frac{d\theta}{d\tau} &\approx -\sin(\theta)\varphi h_d - \sin(\theta)\cos(\theta)(i_z + V_{rw}d_{zz}) \\ \frac{d\varphi}{d\tau} &\approx (1 + d_{zz} + d_{xx})\cos(\theta) - \alpha\varphi h_d\end{aligned}\tag{5.13}$$

Set $u = \cos(\theta)$, we will have

$$\begin{aligned}\frac{du}{d\tau} &\approx (1 - u^2)\left[\varphi h_d + u(i_z + V_{rw}d_{zz})\right] \\ \frac{d\varphi}{d\tau} &\approx (1 + d_{zz} + d_{xx})u - \alpha\varphi h_d\end{aligned}\tag{5.14}$$

Therefore, the frequency could be obtained via the imaginary part of the eigenvalues of the following equations:

$$\begin{aligned}\frac{du}{d\tau} &\approx \varphi h_d + u(i_z + V_{rw}d_{zz}) \\ \frac{d\varphi}{d\tau} &\approx (1 + d_{zz} + d_{xx})u - \alpha\varphi h_d\end{aligned}\tag{5.15}$$

with the eigenvalues:

$$\frac{i_z + V_{rw}d_{zz} - \alpha h_d}{2} \pm \frac{1}{2}\sqrt{(\alpha h_d + i_z + V_{rw}d_{zz})^2 + 4h_d(1 + d_{zz} + d_{xx})}\tag{5.16}$$

Therefore, the frequency is (convert back to the normal unit):

$$f = \frac{\omega}{2\pi} = \frac{\gamma H_k}{4\pi} \sqrt{-(\alpha h_d + i_z + V_{rw} d_{zz})^2 - 4h_d(1 + d_{zz} + d_{xx})} \quad (5.17)$$

$$\approx \frac{\gamma H_k}{4\pi} \sqrt{-4h_d(1 + d_{zz} + d_{xx})}$$

Note that d_{xx} and d_{zz} are both negative. Our frequency formula is accidentally similar to the well known Kitel's formula in literature [65] (if one sets $d_{xx} = d_{zz} = 0$):

$$f = \frac{\gamma H_c}{2\pi} \sqrt{(1 + H_d/H_c)} \approx \frac{\gamma H_c}{2\pi} \sqrt{h_d} \quad (5.18)$$

Fig.5.6 shows the numerical simulation for the frequencies of SSO as a function of the strength of the dipolar coupling (*scale*) and for different input voltages V_{in} . In

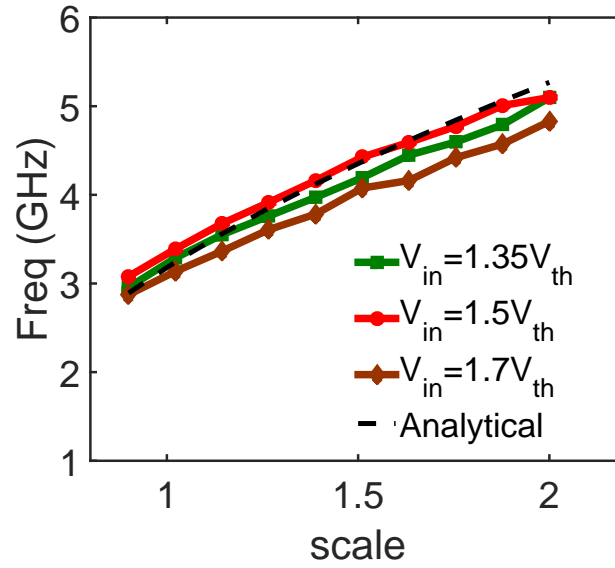


Fig. 5.6. The frequencies of SSO as a function of the strength of the dipolar coupling for different input voltages V_{in} . As one can see, the frequency does not strongly depend on the voltage as long as it is above threshold. The analytical frequency Eq.(5.17) is in good agreement with the numerical results.

this case, we use the dipolar tensor in previous calculations, e.g. Fig.5.4, and assume that one can enhance the dipolar coupling between W and R by:

$$[D]M_s/H_c = scale \times \begin{bmatrix} -2.1 & 0 & 0 \\ 0 & 0 & 0 \\ 0 & 0 & -1.3 \end{bmatrix} \quad (5.19)$$

The analytical frequency turns out to be in a good agreement with the numerical simulations. Moreover, the weak dependence on applied voltage or spin current of the numerical simulations can be understood via Eq.(5.17) due to the very large h_d term, e.g. $h_d \gg i_z$.

Spin Switch Oscillator design

In this section, we would like to discuss the possible designs of SSO as functions of the dipolar coupling strength between (in-plane) W and R. The Fig.5.7 shows the oscillation amplitude of m_r as a function of the aspect ratios and the distances between the R and W magnets. For a given configuration between W and R magnets, the dipolar tensor is evaluated (see appendix B) and coupled LLG equations are solved to get both the frequency and amplitude of the oscillation of the R magnet. From Fig.5.7, it suggests that R and W magnets should have small aspect ratios as well as a small distance to maximize the amplitude of oscillations. This also is in agreement with the previous calculations of the dipolar tensors in Fig.3.7(b) showing the reductions of dipolar couplings for large z_b/x_b .

5.4 SS oscillator with tunable output and power estimations

In the previous sections, we described the basic principle of SSO. Next, we want to discuss why SSO is interesting and how to make SSO having a tunable output. Fig.5.8 shows one example of a SS oscillator where the amplitudes of the signals can be controlled by the voltage V_{out} . Within the device, there are two spin switches: $S1$ and $S2$. The spin switch $S1$ is used to generate the oscillations and so far we have

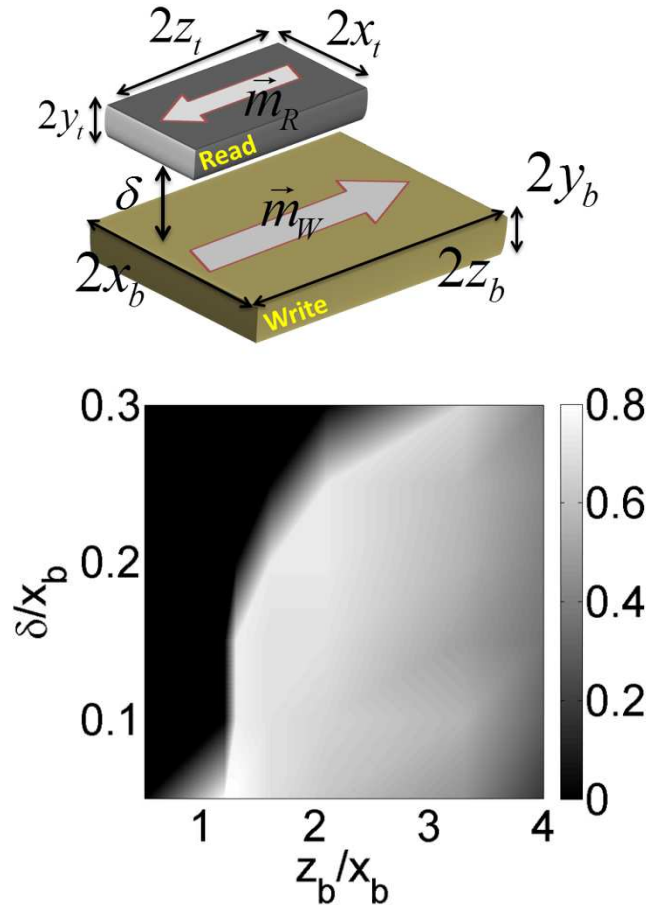


Fig. 5.7. The phase diagram for the frequencies of SS oscillator as a function of dimensions of Write magnet where the gray color is proportional to oscillation amplitude of $m_{r,z}$. In all simulations, we fix the thicknesses of both magnets, $y_t = y_b = 2nm$. While changing the dimensions of Write magnet, we also adjust the dimensions of Read magnet accordingly: $x_t = 0.9x_b$, $z_t = 0.9z_b$. Copyright 2014 IEEE. Reprinted, with permission, from [14].

discussed it. On the other hand, the spin switch $S2$, which is identical to $S1$ except that it has only **one** MTJ at the R unit (see Fig.6.1), allows one to independently control the amplitudes of oscillations by voltage V_{out} . Since both $S1$ and $S2$ share the same GSHE channel and see the same charge currents, their free magnets \hat{m}_W receive the same amount of spin currents which make them oscillate in-phase and so

as the \hat{m}_R at the Read unit of $S2$. The ac output voltage across the load resistance R_L can be estimated from the circuit shown in Fig.5.9.

$$\begin{aligned} R_{MTJ} &= \frac{R_{AP} + R_P}{2} + \frac{R_{AP} - R_P}{2} m_z \cos(\omega t) \\ &= R_{av} (1 + P m_z \cos(\omega t)) \end{aligned} \quad (5.20)$$

and the voltage at Load:

$$V_L = V_{out} \frac{R_L}{R_L + R_{MTJ}} \quad (5.21)$$

The amplitude of oscillations can be calculated as:

$$\langle V_L \rangle_{\text{amplitude}} = V_{L,max} - V_{L,min} \quad (5.22)$$

$$= V_{out} \frac{2R_L R_{av} P m_z}{(R_L + R_{av})^2 - (R_{av} P m_z)^2} \cos(\omega t) \quad (5.23)$$

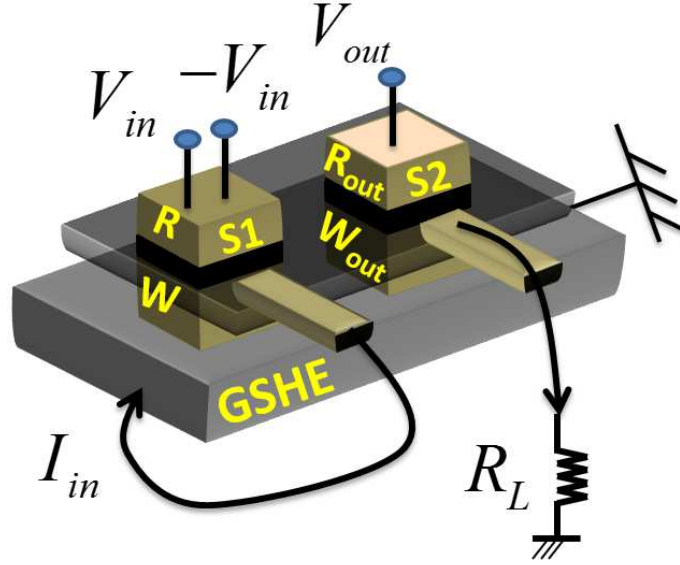


Fig. 5.8. SS oscillator with tunable output: it comprises two spin switches, $S1$ and $S2$. Spin switch $S1$ generates the oscillations and $S2$ duplicates the signals of $S1$ given that \hat{m}_W of both $S1$ and $S2$ see the same (oscillating) charge/spin current. The \hat{m}_W of both $S1$ and $S2$ oscillate in-phase and so as the \hat{m}_R of $S2$. The spin switch $S2$ provides a way to independently control the amplitude of oscillating output via the voltage V_{out} .

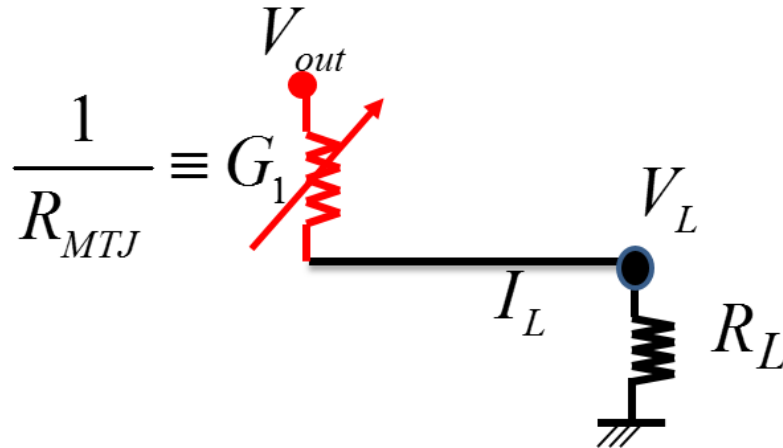


Fig. 5.9. Equivalent circuit for the MTJ at $S2$ unit in Fig.5.8

Note that the output voltage at Load is directly proportional to the V_{out} . This is why SSO can have a tunable output signal. On the other hand, one can estimate the output power of the SSO as:

$$Power = \frac{\langle V_L \rangle_{\text{amplitude}}^2}{R_L} \quad (5.24)$$

Using, for example, the following parameters for the MTJ [65]: $R_L = 50\Omega$; $V_{out} = 0.6V$; $R_{av} = 450\Omega$; $P = 0.4$, one can have $Power \approx 30\mu W$.

5.5 Summary

In this chapter, we have proposed a new kind of oscillator based on incorporating feedback into a transistor-like amplifying device namely the spin switch. Unlike the present-day state-of-the-art spin transfer nano oscillators (STNO) based on the delicate balancing of magnetic fields and spin currents, this spin switch oscillator (SSO) should exhibit high tunable output power without of external magnetic fields.

The matlab codes used to generate the figures can be found at:
<https://drive.google.com/open?id=0B9ggzdMPbfz4VDdld0xPc19ldm8&authuser=0>

6. SPIN SWITCHES FOR COMPACT IMPLEMENTATION OF NEURON AND SYNAPSE

Most of the material in this chapter have been extracted verbatim from the paper: "Spin switches for compact implementation of neuron and synapse", Vinh Diep, Brian Sutton, Behtash Behin-Aein and Supriyo Datta, *Applied Physics Letters* 104 (22), 222405, 2014. Reprinted with permission from [15]. Copyright 2014, AIP Publishing LLC.

6.1 Motivation

Nanomagnets driven by spin currents provide a natural implementation for a neuron and a synapse: currents allow convenient summation of multiple inputs, while the magnet provides the threshold function. The objective of this paper is to explore the possibility of a hardware neural network (HNN) implementation using a spin switch (SS) as its basic building block. SS is a recently proposed device based on established technology with a transistor-like gain and input-output isolation. This allows neural networks to be constructed with purely passive interconnections without intervening clocks or amplifiers. The weights for the neural network are conveniently adjusted through analog voltages that can be stored in a non-volatile manner in an underlying CMOS layer using a floating gate low dropout voltage regulator. The operation of a multi-layer SS neural network designed for character recognition is demonstrated using a standard simulation model based on coupled Landau-Lifshitz-Gilbert (LLG) equations, one for each magnet in the network.

The standard building block for neural networks, Fig.6.1, consists of 1) a synapse that multiplies a number of input signals x_i with appropriate weights w_i and 2) a

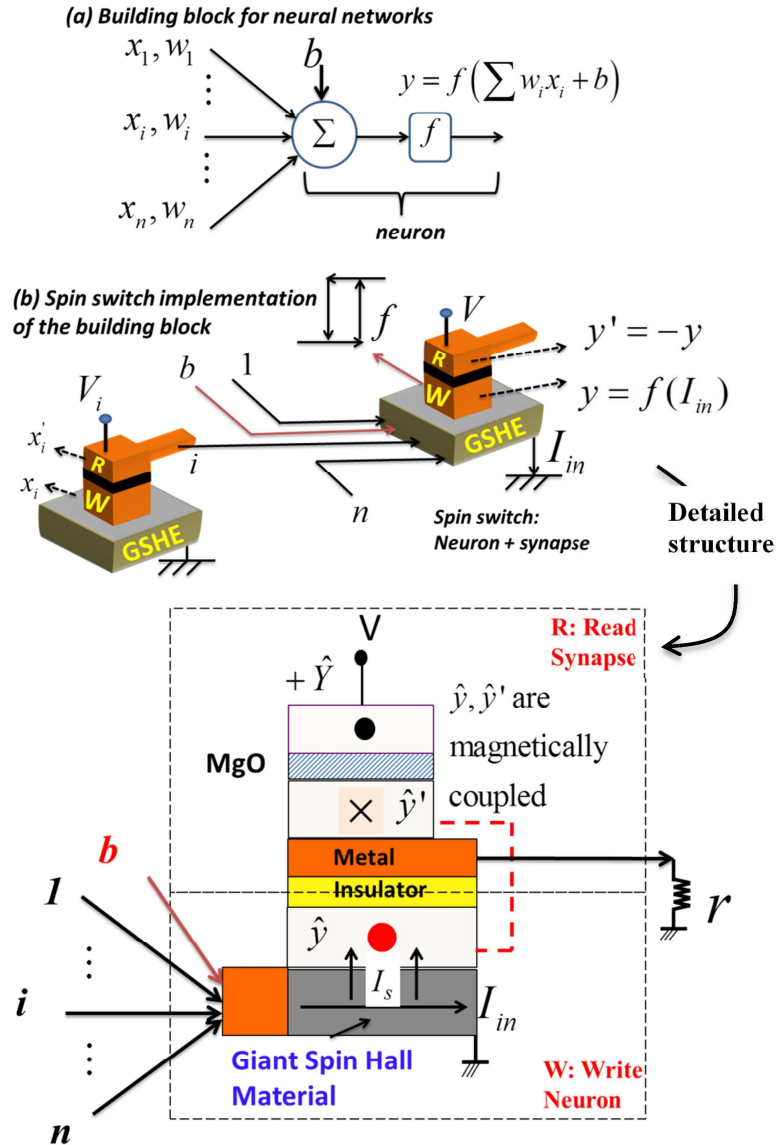


Fig. 6.1. Standard model for the basic building block of neural networks: A neuron sums the incoming signal x_i with weights w_i and generates the output according to the activation function f as expressed by Eq.(6.1). Spin switches can be used to provide a compact implementation of this building block as evident from comparing Eq.(6.4) with Eq.(6.1). Reprinted with permission from [15]. Copyright 2014, AIP Publishing LLC.

neuron that sums all the weighted inputs together with a fixed bias b to produce an output y determined by some nonlinear function f

$$y = f\left(\sum_i w_i x_i + b\right) \quad (6.1)$$

It is well established that multilayer neural networks obtained by interconnecting building blocks of this form can be designed to implement useful functions and powerful algorithms have been developed for choosing the weights w_i and the bias b_i so as to implement a desired overall input-output functionality.

Most neural networks are usually implemented through software although it is recognized that hardware implementation could potentially [69, 70] lead to significant speed, power improvements and massively parallel computation [71]. Different proposals based on spin torque devices, domain wall motions and memristors were previously proposed to implement neurons or/and synapses [72–74]. The objective of this paper is to demonstrate the feasibility of implementing a hardware neural network (HNN) using a spin switch (SS) [17] as the basic building block, by presenting a concrete implementation of a SS neural network for character recognition and establishing its operation through direct simulation using experimentally benchmarked models for SS devices. SS has a gain that gives it a transistor-like character allowing multiple units to be interconnected without intervening CMOS circuitry for clocks or amplifiers: one spin switch can directly drive the next one like ordinary transistors.

6.2 Spin switch as a basic building block for Neural Network

6.2.1 Modified Spin Switch for neural network

Fig.6.1 also shows a schematic representation and a detailed structure of a building block implemented with a spin switch. It consists of a Write (W) unit and a Read (R) unit with free magnetic layers or (y, y') that are dipole coupled to ensure that the two are always anti-parallel $x_i = -x'_i$. This configuration allows information to propagate from the Write to the Read unit of a spin switch while maintaining their electrical

isolation. As we will see, the Write unit functions as a neuron which performs the summation and threshold function f while the Read unit functions as a synapse which provides the weighted output $w_i x_i$.

The Read unit consists of one MTJ whose conductance is

$$G_i = g_i/2(1 + P_i \hat{Y}_i \cdot \hat{y}'_i) = g_i/2(1 - P_i \hat{Y}_i \cdot \hat{y}_i) \quad (6.2)$$

where $P_i = (G_P - G_{AP})/g_i$; $g_i = G_P + G_{AP}$; \hat{Y}_i (or \hat{X}_i) is the magnetization of fixed magnet and \hat{y}_i (or \hat{x}'_i) is the magnetization of free magnet.

The Write unit consists of a giant spin Hall effect (GSHE) metal like Ta [13] or tungsten [46] and a free magnet \hat{x}_i (or \hat{y}_i) which generates a spin current I_s when driven by a charge current $I_{in} : I_s = \beta I_{in}$, $\beta = \theta_{SH}(A_s/A)$ and θ_{SH} being the spin-Hall angle. A_s and A are the cross-sectional areas for the spin and charge currents respectively.

The Read unit functions as a synapse whose output current is weighted by $\sim V_i G_i$ while the Write unit functions as a neuron (see Fig.6.1): it sums weighted inputs from the R units of many spin switches labeled $1, \dots, i, \dots, n$ giving rise to a net current

$$I_{in} = \sum_i V_i \frac{G_i(\hat{x}_i)}{1 + G_{total} r} + I_b \quad \text{where } G_{total} \equiv \sum_i G_i \quad (6.3)$$

(r : resistance of the GSHE metal) and performs a hysteretic threshold function f of the form sketched in the figure to produce the output:

$$y = f(I_{in}) = f\left(\sum_i \frac{V_i g_i}{2(1 + G_{total} r)} (1 - P_i \hat{X}_i \cdot \hat{x}_i) + I_b\right) \quad (6.4)$$

Comparison with Eq.(6.1) suggests that spin switches could provide a possible building block for HNN using V_i to implement the desired weights $w_i = V_i g_i/2(1 + G_{tot} r)$. However, the details are not obvious especially since the function f is hysteretic rather than the usual single-valued function.

In estimating the threshold current/voltage needed to drive the (next) Write unit, we note that a spin current of $2I_{sc}$ (critical spin current required to switch the magnet)

will be needed to flip the Write magnet since it couples to the magnet of the Read unit. Hence:

$$I_{th} \geq \frac{2I_{sc}}{\beta} = \frac{2I_{sc}}{\theta_{SH}(A_s/A)} \quad (6.5)$$

As a result, the threshold voltage

$$V_{th} \geq \frac{2I_{th}}{g_i(1-P)}(1+G_i r) \quad (6.6)$$

Using parameters described in Ref. [17], we have $I_{sc} = 160\mu A$. If $t_{gshc} = 2nm$ and the Hall angle reported experimentally $\theta_{SH} = 0.3$ for tungsten, the threshold current $I_{th} \approx 30\mu A$.

Also assuming TMR of 135% for the MTJ and resistance-area product of $A_s/G_P = 4.3\Omega\mu m^2$ [75], we have $P = 0.4$ and $g_i = (1.1k\Omega)^{-1} - 1$ for $A_s = 80nm \times 30nm$. If we choose other GSHE material [47, 76] with comparable spin hall angle but with low resistivity, then we can assume $G_i r \ll 1$. This will give us $V_{th} \approx 100mV$.

The power consumption of SS can be estimated as $P = I_{th}V_{th} \approx \text{few } \mu W$ along with the switching time of magnet as $\tau \approx 1ns$, resulting in energy consumption for the SS $E \approx \text{few } fJ$ per switch. We should mention, however, that from the point of view of energy and delay, spin switches (or in general beyond-CMOS devices [4]) based on established technology are inferior to a single CMOS transistor, but may still look attractive compared to CMOS based neurons [77], due to the compactness and multi-functionality provided by the SS (note that, the area of a SS is roughly the area of magnet in the Read or Write unit which is typically $\approx 100nm^2$). Moreover, the switching energy of a single SS neuron could be lowered significantly as new phenomena are discovered and developed (see for example [78, 78, 79]).

6.2.2 Composite spin switch neuron with built-in synapses

An important attribute of the SS is the possibility of large fan-out, whereby the output from one spin switch can be used to drive hundreds of other spin switches thus allowing large interconnectivity which is important for implementing neural network functions.

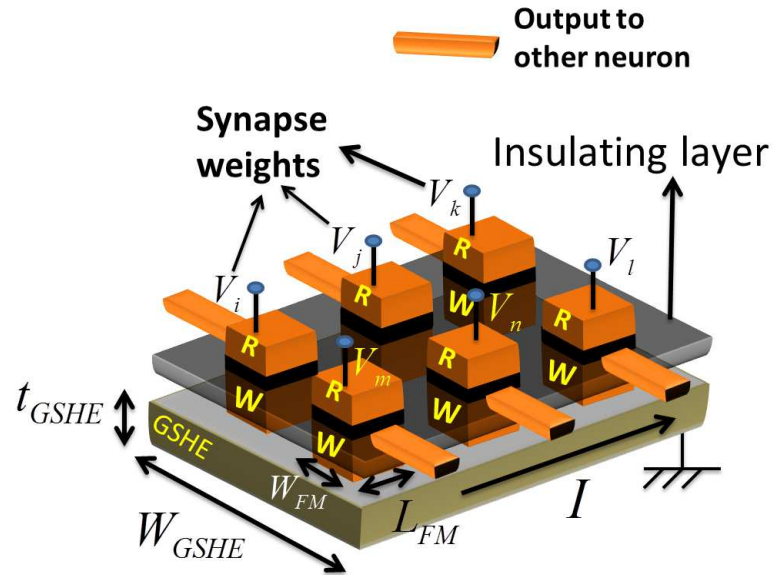


Fig. 6.2. A composite spin switch neuron with built-in synapses. The magnetization of any R unit represents the state of the neuron. The voltages at R units represent the weight of synapses connecting to other neurons. Reprinted with permission from [15]. Copyright 2014, AIP Publishing LLC.

Fig.6.2 shows a SS neuron with multiple outputs where the voltage at each R unit represents the synaptic weight of this neuron in connection with the other neurons. Since each R unit has its own independent power supply, this neuron should be able to drive a large number of outputs. Note that the interconnections between neurons do not require GSHE material. They could be low resistance material (copper wires) with no increase in energy consumption. The only limitation arises from the threshold current/voltage needed to drive such a big neuron. Eq.(6.5) shows that the threshold current is proportional to the area A of GSHE, but independent of its length. Of course the resistance r of the GSHE increases with length but this has a minimal effect on the threshold voltage as long as the factor $(1 + G_i r)$ is not excessive. For example, if $L_{gshe}/L_{FM} = 100$, $W_{gshe}/W_{FM} = 2$, $\rho_{gshe} = 10^{-7} \Omega m$ we have $(1 + G_i r) \approx 3$.

6.2.3 Training methods for hysteresis activation function by back propagation method

We focus on the multi-layer feed-forward NN with training done off-line by smoothing the SS hysteresis function to make it differentiable and adapting the back-propagation method [80]. Other techniques such as the weight perturbation method [81] or the extreme learning machine [82] might also be suitable especially for on-chip training. The key difference with standard neural network design is the hysteresis in the threshold function f which makes the overall design more robust, but requires an extra condition during the training: the currents arriving at each neuron have to be above threshold. In this section, we will focus on how to do the training for NN having hysteresis activation functions as in SS.

Back-Propagation (BP) method: the bottom line

Here we will briefly mention idea behind the BP method: Suppose we have a network as in Fig.6.3 where we want to find the weight ω_{ij} and bias b_i so that the

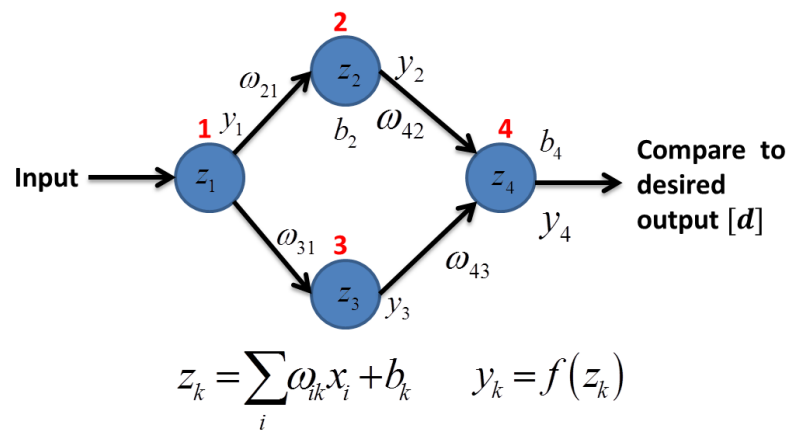


Fig. 6.3. An example of a neural network used to illustrate the idea behind the BP method.

output y_4 will be as close as to the desired output d . This means we want to minimize the error function:

$$\epsilon = \frac{1}{2}(d - y_4)^2 \quad (6.7)$$

Note that the total input at a neuron k is defined as:

$$z_k = \sum_i \omega_{ik}x_i + b_i \quad (6.8)$$

and the neuron k will produce the output according to its activation function f :

$$y_k = f(z_k) \quad (6.9)$$

Starting from the output layer (neuron 4), we note that the change in weights (in this example ω_{42} and ω_{43}) coming to neuron 4 will change the output and hence the error function. Therefore, the update of the weights should be:

$$\begin{aligned} \Delta\omega_{42} &= -\eta \frac{\partial \epsilon}{\partial \omega_{42}} = -\eta \frac{\partial \epsilon}{\partial y_4} \frac{\partial y_4}{\partial z_4} \frac{\partial z_4}{\partial \omega_{42}} \\ &= \eta \left[(d - y_4) f'(z_4) \right] (1 + Py_2) = \eta \phi_4 \end{aligned} \quad (6.10)$$

where $\phi_4 = [(d - y_4) f'(z_4)]$. Using the information of ϕ_4 and ω_{42} , we process to find the update for the weight close to the input layer ω_{21}

$$\begin{aligned} \Delta\omega_{21} &= -\eta \frac{\partial \epsilon}{\partial \omega_{21}} = -\eta \frac{\partial \epsilon}{\partial y_4} \frac{\partial y_4}{\partial z_4} \frac{\partial z_4}{\partial y_2} \frac{\partial y_2}{\partial z_2} \frac{\partial z_2}{\partial \omega_{21}} \\ &= \eta \left[\phi_4 (P\omega_{42}) f'(z_2) \right] (1 + Py_1) = \eta \phi_2 (1 + Py_1) \end{aligned} \quad (6.11)$$

where $\phi_2 = \phi_4 (P\omega_{42}) f'(z_2)$. Similarly we can find the update for Δ_{43} and Δ_{31} . For the update of bias,

$$\begin{aligned} \Delta b_4 &= -\eta \frac{\partial \epsilon}{\partial b_4} = -\eta \frac{\partial \epsilon}{\partial y_4} \frac{\partial y_4}{\partial z_4} \frac{\partial z_4}{\partial b_4} \\ &= \eta \left[(d - y_4) f'(z_4) \right] = \eta \phi_4 \end{aligned} \quad (6.12)$$

and one can easily prove that

$$\Delta b_2 = \eta \phi_2 P \quad (6.13)$$

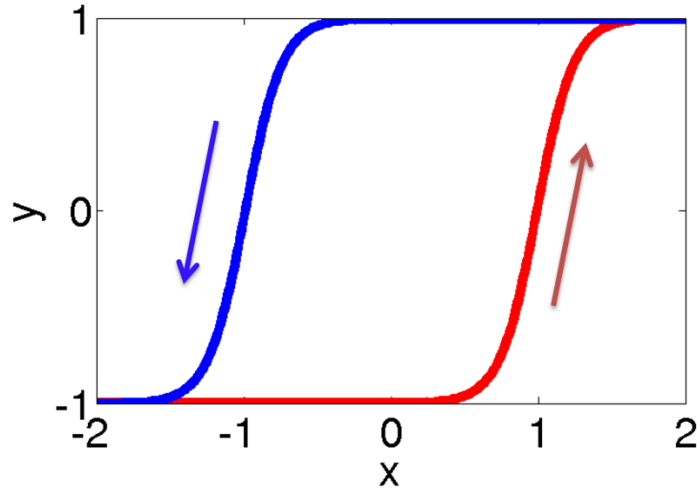


Fig. 6.4. An approximation of hysteresis function ($c = 4$ in Eq.(6.14)) used in the training of hysteretic NN. Reprinted with permission from [15]. Copyright 2014, AIP Publishing LLC.

Since the back propagation (BP) method requires a differentiable activation function, we have to approximate the hysteresis activation of the magnet, for example, in the following way:

$$y = f(x, x_0) = \begin{cases} \tanh(c \cdot (x - 1)) & \text{if } x \geq x_0 \\ \tanh(c \cdot (x + 1)) & \text{if } x \leq x_0 \end{cases} \quad (6.14)$$

where x_0 is the history value of x . For example, the red curve in Fig.6.4 is calculated with large negative x_0 while in the green curve, x_0 is a large positive number. To illustrate the concept, we focus on SS neural network having 3 layers: input, hidden and output as in Fig.6.5 where each neuron is a $W - R$ pair having opposite magnetization. The signals arrive at W units and come out at the R units. Given a set of input $[x]$ (training set) and a desired output $[d]$ vector, the BP method will find weight matrices $[W_1], [W_2]$ and bias $[b_1], [b_2]$ vectors such that the input produces the output. The output of a neuron i is:

$$y_i = f \left(\sum_j W_{ij}(1 \pm P_j x_j) + b_i \right) \quad (6.15)$$

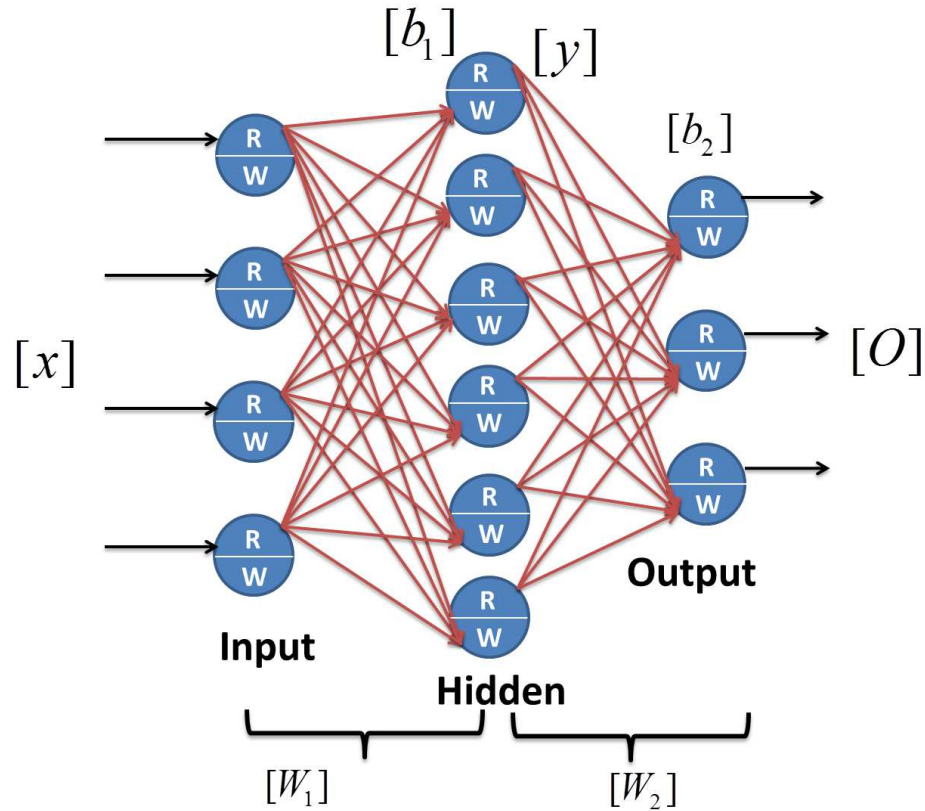


Fig. 6.5. A typical spin switch neural network with 3 layers: input, hidden and output layers. $[x]$ is the input vector, $[b_1]$ and $[y]$ are respectively the bias and output of W neurons in the hidden layer. $[b_2]$ and $[O]$ are bias and output vectors of neurons in the output layer respectively. Reprinted with permission from [15]. Copyright 2014, AIP Publishing LLC.

where x_j is the magnetization of magnet in the W or R unit (they have opposite signs). Therefore, we can follow the BP method in literature [80] with neuron states represented by $1 + Px_j$ or $1 - Px_j$. Here are the steps used in finding the weights for a SS neural network:

For each training (epoch) {

Randomly initialize values of $[W_1], [W_2], [b_1], [b_2]$

and states of neurons in the hidden and output layers.

For each vector in the input set:

```

{
  Feed Forward, calculate updated functions and update the weight
}
}
  Evaluate the total mean square error

```

The Feed Forward, update functions and weigh update are described in the flowing steps:

1. Calculate the outputs of neurons in the hidden layer

$$[y] = f(W_1(1 + P[x]) + [b_1])$$

where f is the activation function. Notice that those are the outputs of the Write units.

2. Calculate the outputs of neurons in the output layer:

$$[O] = f(W_2(1 - P[y]) + [b_2])$$

Notice that the outputs of Read unit are opposite to the outputs $[y]$ of Write unit in step 1.

3. Calculate the update functions:

$$[\Phi_2] = [f']_{\text{at output}} \cdot ([d] - [O])$$

$$[\Phi_1] = [f']_{\text{at hidden}} \cdot [W_2]^T [\Phi_2]$$

Where the derivatives of f are evaluated at output and hidden layer neurons for Φ_2 and Φ_1 respectively. The \cdot means element times element between the two vectors. $[\]^T$ means the transpose of the matrix.

4. Update the weight matrices and bias vectors:

$$\begin{aligned} [b_1] &= [b_1] - \eta P[\Phi_1] \\ [b_2] &= [b_2] + \eta[\Phi_2] \\ [W_1] &= [W_1] - \eta P(1 + P[x])^T[\Phi_1] \\ [W_2] &= [W_2] + \eta(1 - P[y])^T[\Phi_2] \end{aligned}$$

where η is the learning coefficient.

The total mean squared error function can be calculated as:

$$E = 1/2 \left| [d] - [O] \right|^2 \quad (6.16)$$

If E is smaller than a selected criteria, we stop the algorithm, otherwise continue to train the network.

As mentioned before, the hysteresis activation function requires one more condition: the total weighted sum arriving at neurons has to be above threshold. This will make sure that, the mapping from the input to the output is independent of the initial states of the hidden and output neurons. One way to accomplish this is to randomize the states of the neurons before entering for loop of input set in the above scheme. It is also desirable to find weights that have low voltage values to avoid accidental switching of magnets in the Read units. The states of neurons should be determined by the signals arriving at the W units and not by the weight voltages at R units.

6.2.4 Modeling Spin Switches Neural Network(NN)

To model SS devices, it is noticed that each SS with a W/R pair requires a pair of LLG equations for the magnet pair \hat{x}_i (or \hat{y}_i) and \hat{x}'_i (or \hat{y}'_i).

$$\begin{aligned} \frac{d\hat{x}_i}{d\tau} &= -\hat{x}_i \times \vec{h} - \alpha \hat{x}_i \times \hat{x}_i \times \vec{h} - \hat{x}_i \times \hat{x}_i \times \vec{i}_{si} + \alpha \hat{x}_i \times \vec{i}_{si} \\ \frac{1 + \alpha'^2}{1 + \alpha^2} \frac{d\hat{x}'_i}{d\tau} &= -\hat{x}'_i \times \vec{h}'_i - \alpha \hat{x}'_i \times \hat{x}'_i \times \vec{h}'_i - \hat{x}'_i \times \hat{x}'_i \times \vec{i}'_{si} + \alpha \hat{x}'_i \times \vec{i}'_{si} \end{aligned} \quad (6.17)$$

where

$$\tau = (\gamma\mu_0 H_k t)/(1 + \alpha^2); \vec{h} = \vec{H}/H_k; \vec{h}' = \vec{H}'/H_k$$

where H and H' are defined in the previous chapter (Eq.(3.2) and Eq.(3.3)). The dimensionless spin currents in Eq.(6.17) are given by:

$$\vec{i}_{si} = \frac{\vec{I}_{si}}{(2q/\hbar)\mu_0 H_k M_s \Omega} ; \quad \vec{i}'_{si} = \frac{\vec{I}'_{si}}{(2q/\hbar)\mu_0 H_k M_s \Omega} \quad (6.18)$$

The following parameters are used for all magnets:

$$\alpha = 0.01; H_d = 50H_k, D_{zz}M_s = D_{xx}M_s = H_k = 0.02T/\mu_0$$

$$\mu_0 M_s = 1T; \Omega = 80nm \times 100nm \times 1.6nm$$

The spin currents are obtained by summing the inputs from the preceding Read units.

$$\vec{I}_{si} = \beta \left(\sum_j V_j \frac{G_j(\hat{x}_j)}{1 + r_i G_{\text{total}}} + I_{bi} \right) \hat{z}; \quad \vec{I}'_{si} = -P_i V_i G_i \hat{z} \quad (6.19)$$

where V_i are the voltages and I_{bi} are bias currents applied at preceding Read units. Fig.6.6 shows the input-output characteristic of a SS device. Note that at $V = 0$, the switching currents are symmetric but there is a minor shift when $V = V_{th}$. This is due to a (small) spin current I'_s injected by the Read unit making it easier to switch from

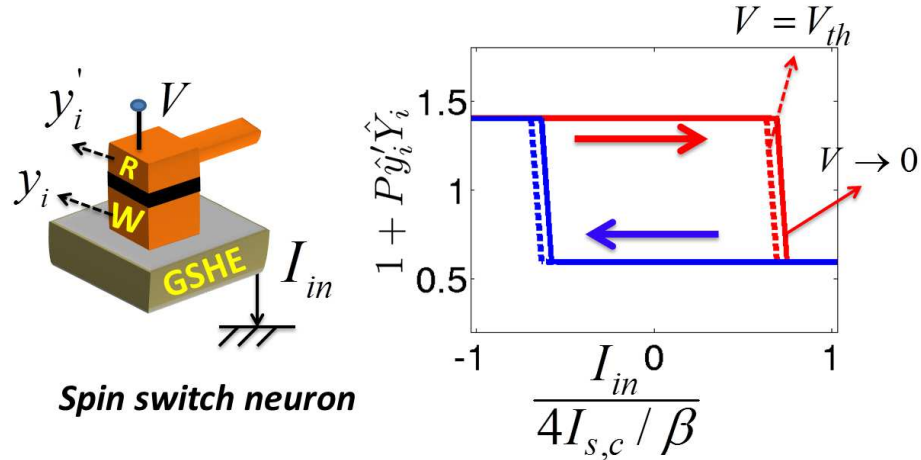


Fig. 6.6. Switching characteristic of Spin Switch (or the activation function): $V = 0$ (solid line) and $V = V_{th}$ (dash line). Reprinted with permission from [15]. Copyright 2014, AIP Publishing LLC.

+1 to -1 than to switch from -1 to +1. This shift is relatively minor ensuring the key property of directionality: the state of the magnet (neuron) is largely determined by the input and not the output current.

6.3 Spin Switch neural network for Exclusive Or

As a simple example of the SS-based implementation of a neural network, we show the layout for a non-linear exclusive or (XOR) gate in Fig.6.7(a). The voltages V applied at Read units represent the weight of synapse connecting neuron i and j while the I_b represents the bias current applied at each neuron. Voltages and currents are obtained via training and their values are normalized to the threshold values.

Fig.6.7(b) shows the simulation results of XOR obtained by solving a set of 30 coupled first-order differential equations (three components of the ten magnets, two per each neuron: A, B, 1, 2, 3) whose solutions are the dynamics of the magnets. For a neuron with many synapses, we assume all the W/R units are identical so that the whole neuron can be modeled as a single W/R unit. It is evident from Fig.6.7(b) that the network behaves as an XOR gate when it responds to inputs A and B. For example, (A,B)=(1,1) and (-1,-1) have the same outputs and similarly for (A,B)=(1,-1) and (-1,1).

The XOR layout in Fig.6.7(a) is quite robust to small variations of voltages, bias currents and is not affected by thermal noise. This can be understood in the following way by defining the dimensionless weighted sum at the W units:

$$Z_W(j) = \sum_i V_{ij}(1 + Pm_z(i)) + I_b(j) \quad (6.20)$$

where V_{ij} is the normalized voltage connecting neuron i and j . $I_b(j)$ is the normalized bias current at neuron j . If $|Z_w(j)| > 1$, this implies that $|I_W(j)| > I_{th}$ and the magnet in W unit will be switched depending on the sign of $Z_W(j)$. Table 6.1 shows the calculation of weighted sum $Z_W(j)$ (Eq.(6.20)) at neuron j in the hidden and output layers (labeled 1,2 and 3) and its corresponding states (at Read unit) for every pair of inputs. As shown, they satisfy the condition $|Z_W(j)| > 1$ at every neuron for $P = 0.4$

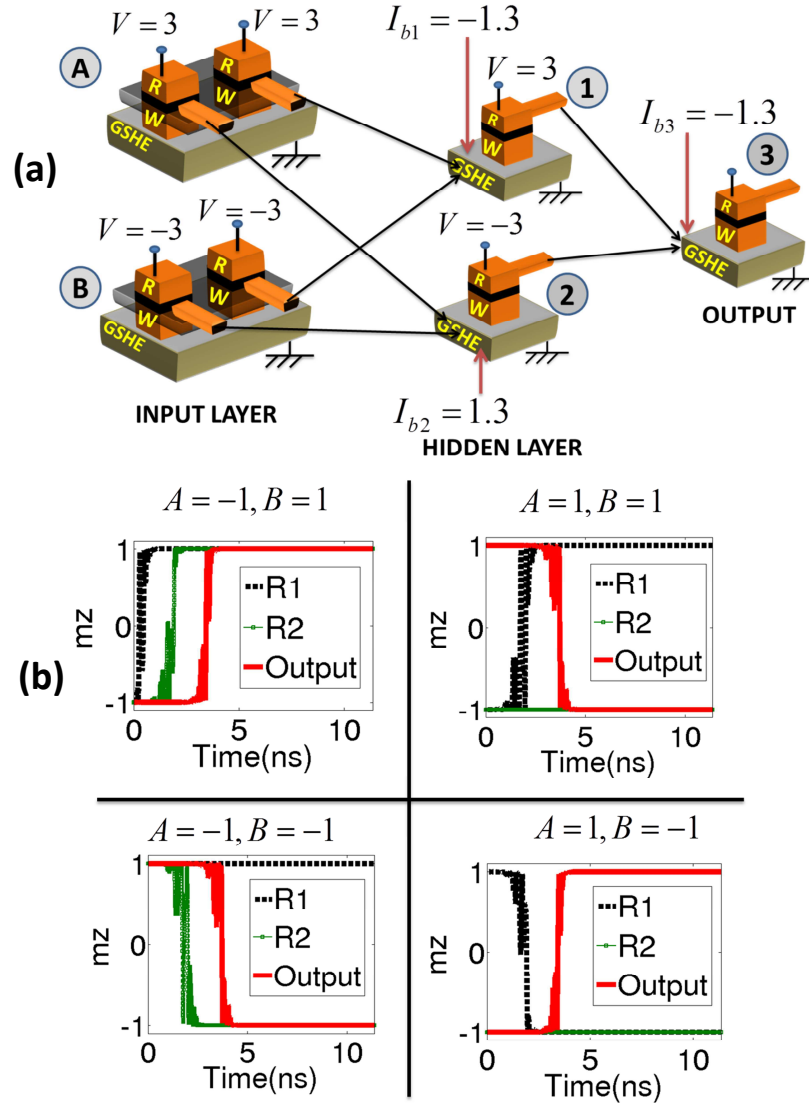


Fig. 6.7. a) Spin switch neural network implementation for exclusive or gate. Here A and B are inputs. Hidden and output neurons are labeled 1, 2 and 3. b) Simulation results of the dynamics of the network responding to inputs. Here R1, R2 and output are the magnetizations (R units) of neuron 1, 2 and 3 respectively. All the neuron states are randomized initially. We assume all magnets have the same polarization and conductance: $P_i = 0.4$, $g_i = (1.1k\Omega)^{-1}$, $\beta = 12$

which means currents arriving at neurons are always above threshold. Because of this, the switching characteristics will not be affected by thermal noise. The table

Table 6.1

Calculating the Weighted sum Z_W and corresponding magnet states at neurons 1,2 and 3 as a function of input magnets for SS XOR problem as in Fig.6.7(a).

Input(R)	$Z_W(1)$	$Z_W(2)$	$m_z(R_1)$	$m_z(R_2)$	$Z_W(3)$	Output(R)
-1/1	-1.3	1.3	1	-1	6P-1.3	-1
-1/1	-6P-1.3	1.3-6P	1	1	-1.3	1
1/-1	6P-1.3	1.3+6P	-1	-1	-1.3	1
1/1	-1.3	1.3	1	-1	6P-1.3	-1

also suggests that a small variation of voltages and currents will not affect the results, making the design quite robust. For example, if we change $|V| = 3$ to $|V| = 3.2$ in the layout (keeping the sign), the network still functions as before.

6.4 Spin Switch Neural Network for character recognition

Now we consider an example of a SS neural network designed for character recognition: it recognizes 8 letters $A, B, C \dots H$ represented by 7×5 matrices or vectors having 35 components (zero or one). Fig.6.8(a) shows the layout of the SS neural network for this pattern recognition with 35 neurons in the input layer, 6 neurons in the hidden and 3 neurons in the output layer (labeled from 1 to 9). Hence each neuron in the input layer has 6 synapses while each neuron in the hidden has 3 synapses. The voltages V applied at Read units represent the weight of synapse in connecting with other neurons while the I_b represents the bias current applied at each neuron. Both voltages and bias currents obtained through the training are shown in Fig.6.8(b) in the form of (35×6) , (6×3) matrices and (1×9) vector. They are all normalized to their threshold values.

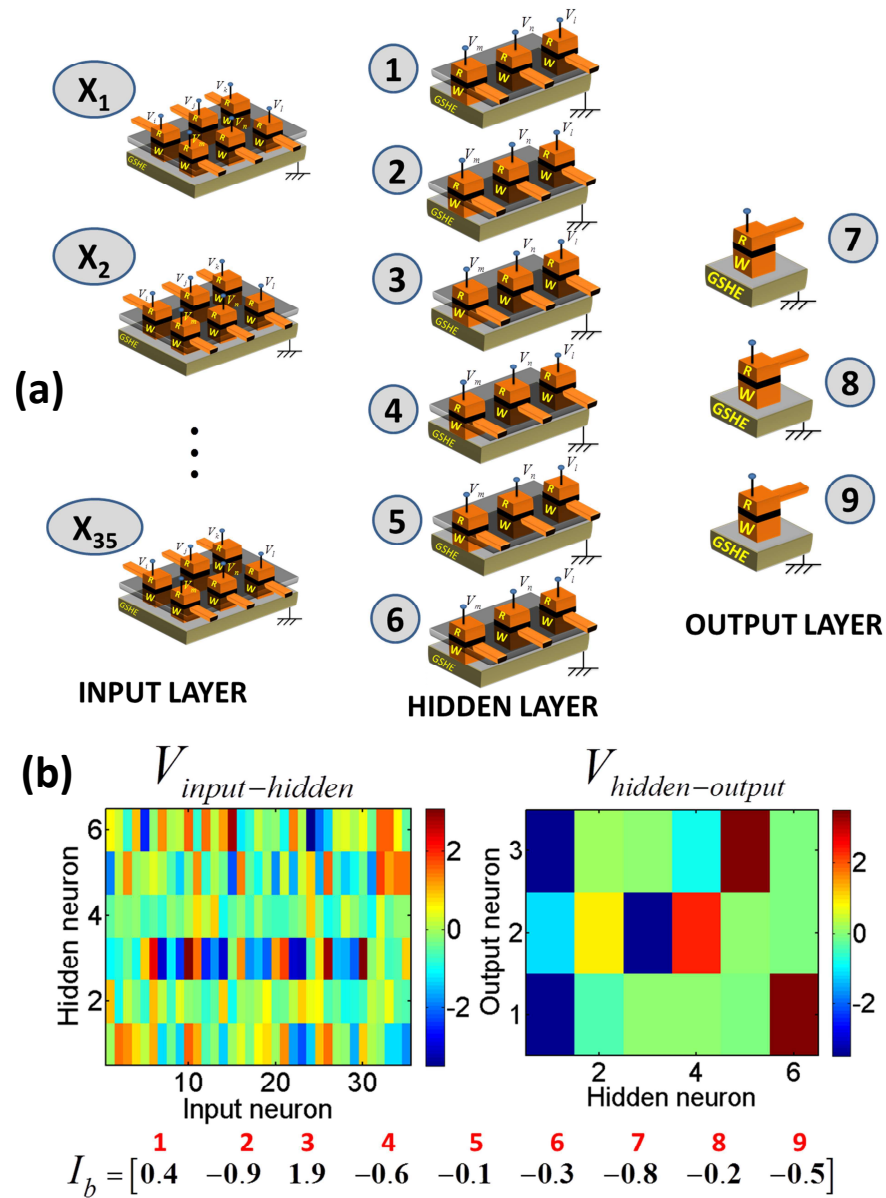


Fig. 6.8. (a) Implementation of spin switch neural network for character recognition: for simplicity the connections (copper wires) between layers are not shown. (b) Matrices of interconnection weight voltages between input and hidden layers (35×6) and between hidden and output layers (6×3) shown by color scale. Reprinted with permission from [15]. Copyright 2014, AIP Publishing LLC.

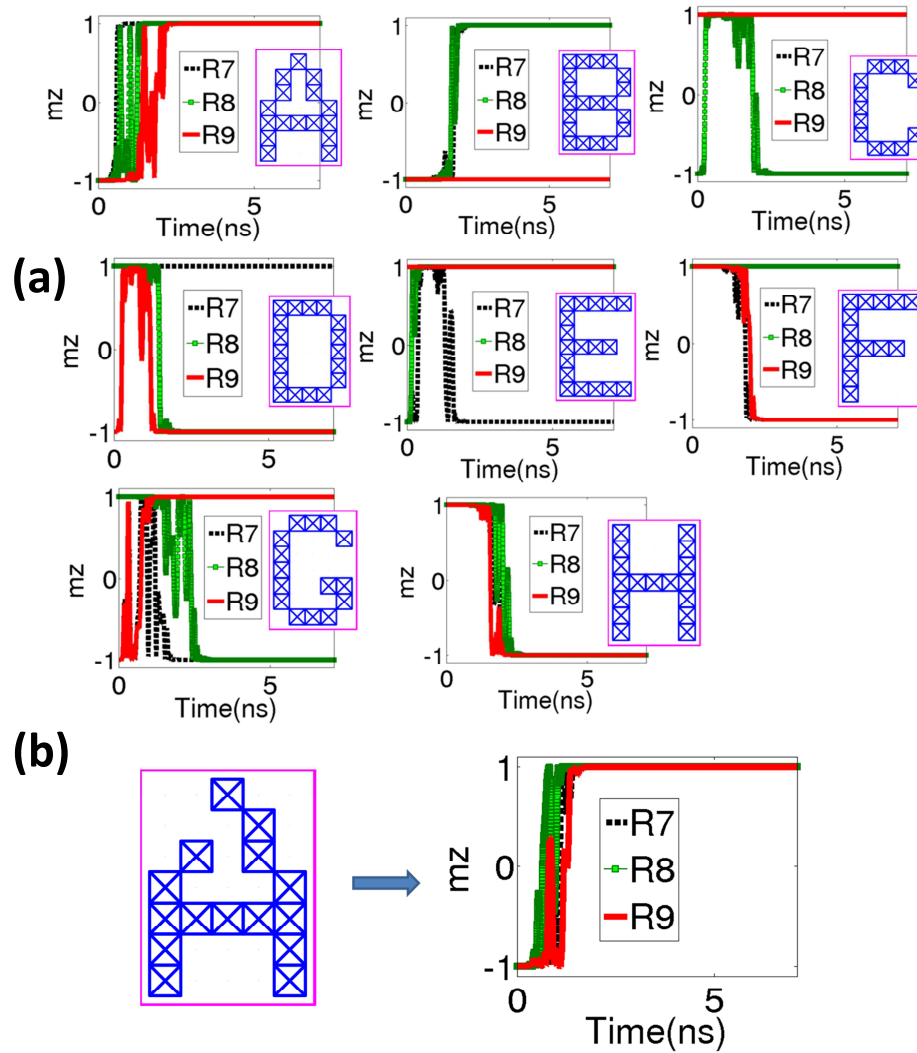


Fig. 6.9. (a) LLG simulations for the output layer of the SS neural network described in Fig.6.8(a) in response to eight input characters: $A, B, C \dots H$. Here $R7, R8$ and $R9$ are the magnetizations of magnets in the R units of neuron 7, 8 and 9 respectively. (b) The network still recognizes a letter that is not in the training set (a random defect). We assume all Read units have the same polarization and conductance: $P_i = 0.4, g_i = (1.1k\Omega)^{-1}, \beta = 12$. Reprinted with permission from [15]. Copyright 2014, AIP Publishing LLC.

Fig.6.9(a) shows simulation results obtained from solving a set of 88 coupled LLG (70 for the input, 12 for the hidden and 6 for the output layer) equations whose

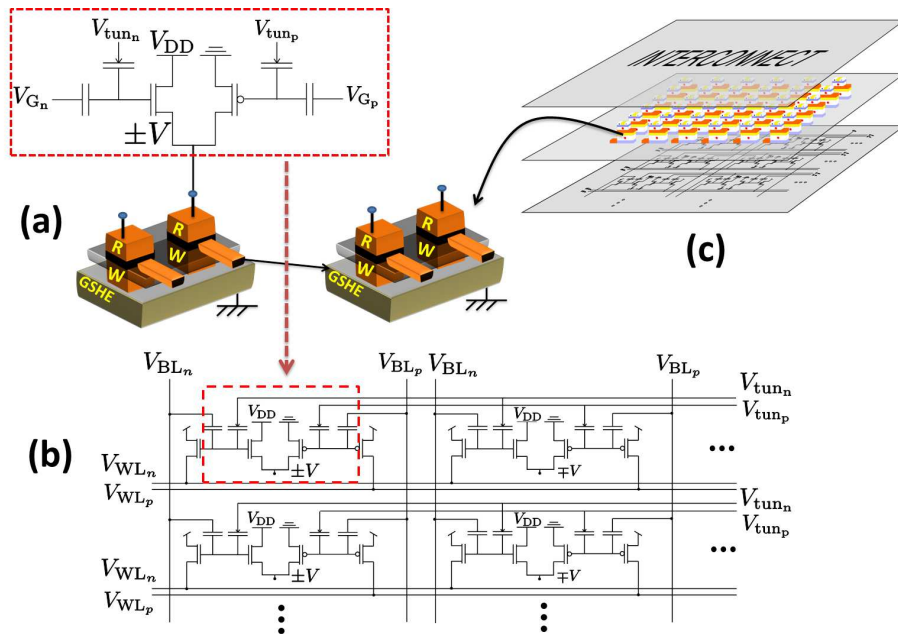


Fig. 6.10. Possible way of supplying/storing long term voltage a) The weights ($+/-V$) of the MTJ stack are provided through the use of tunable complementary floating-gate low dropout voltage regulators. Channel Hot Electron Injection and Fowler-Nordheim tunneling modulated by V_G , V_{tun} can be used to adjust the charge trapped on the floating gate. In turn, those charges adjust the threshold of the nFET/pFET devices giving $+/-V$ at the MTJ of the R unit. b) Each floating-gate may be formed in a bit-addressable array for individual nFET/pFET threshold tuning. c) The spin-switch layer is formed in the metallization above the silicon layer along with the interconnect for the neural network. Reprinted with permission from [15]. Copyright 2014, AIP Publishing LLC.

solutions are the dynamics of the magnets. For a neuron with many synapses, we assume all the W/R units are identical so that the whole neuron can be modeled as a single W/R unit. Fig.6.9(a) illustrates the character recognition function: If the input is A , the output is 000 which can be translated to $\bar{1}\bar{1}\bar{1}$ for magnetizations of W magnets (note $\bar{1}$ means $m_z = -1$). For magnets in the R units the result is 111 . It is interesting to notice that, even there is a (random) defect in the letter, the network is still able to recognize it as shown in Fig.6.9(b).

It is also noticed that the layout for character recognition in Fig.6.8 is quite robust to small variations of voltages and bias currents (see also XOR example in the appendix). Since currents arriving at neurons are always above threshold, the switching characteristics will not be affected by thermal noise.

Finally, we would like to discuss a possible way of storing and adjusting the voltage applied at R units. The use of floating-gate(FG) transistors has been proposed as a mechanism to store tunable analog voltages which can be used for synapse weights [83, 84]. Controlled amounts of charge can be injected and removed from the gate to create a spectrum of gate voltages which is important in the realm of neural networks.

Fig.6.10 shows a possible way to store/adjust the voltages applied at the synapse Read unit MTJs using a FG low drop-out voltage regulator [85]. As depicted, programmatic control of an individual FG charge can be accomplished through an addressable array that selectively controls $(V_{tun,n}, V_{Gn})$ and $(V_{tun,p}, V_{Gp})$. The tunneling voltage can be used to provide a global erase of stored values via Fowler-Nordheim tunneling while the respective gate voltages can be used to inject charge onto the FG with Channel Hot Electron Injection. This charge control in turn modulates the threshold voltage of the nFET/pFET and hence the regulated voltage. As a result, the nFET/pFET can be programmed to provide the desired synapse weights through an active learning process. Once programmed, these FG transistors will retain the voltage for an extended period of time due to their non-volatility.

6.5 Summary

We have demonstrated the possibility of a hardware neural network implementation using a spin switch (SS) as its basic building block. SS is a recently proposed device based on established technology having a transistor-like gain and input-output isolation that allows large circuits to be constructed without intervening clocks or amplifiers. The SS neuron-synapse used in the present paper differs from the SS

proposed in Ref. [7] in the sense that there is only one MTJ stack at the Read unit. Among the three components comprising the SS, so far the GSH material and MTJ stack have been experimentally established. The dipolar coupling has also been well studied in the context of nano-magnet logic [34]. But for SS applications, one needs to show the dipolar coupling between magnets having thicknesses 2-4nm.

We have shown that a SS can be used to build neuron capable of performing summation, multiplication and an activation function which normally requires extra circuitry in other hardware implementations. The SS neurons occupy areas much less than μm^2 , consume femtojoules per switch and operate at room temperature. The weights for the neural network are conveniently adjusted through analog voltages that can be stored in a non-volatile manner in an underlying CMOS layer using a floating gate low dropout voltage regulator. The operation of a multi-layer SS neural network designed for character recognition is demonstrated using a standard simulation model based on coupled Landau-Lifshitz-Gilbert (LLG) equations, one for each magnet in the network.

The matlab codes used to generate the figures can be found at:

<https://drive.google.com/open?id=0B9ggzdMPBfz4VDdld0xPc19ldm8&authuser=0>

7. “TRANSISTOR-LIKE” SPIN SWITCHES FOR HARDWARE NEURAL NETWORK: AN OUTLOOK

Some contents of this section have been extracted verbatim from the following manuscript: ‘Magnet based implementation of a Transynapse’, Behnash Behin-Aein, Vinh Q Diep and Supriyo Datta, in-preparation.

As mentioned in the introduction, for conventional Boolean logic applications, spintronic devices based on established technology are not the drop-in replacement for CMOS transistors. However, this could be changed as new materials and phenomena are discovered to improve Read and Write mechanisms in magnet-based switches. Spintronic-based switches could still look attractive for applications such as hardware implementation of neural networks as discussed in chapter 6. There, we have shown that the spin based magnetic neurons can be very compact compared to other hardware implementation. For example, the neuron operations such as summation, multiplication and activation function can be achieved by a single spin-based magnetic device. To our knowledge, this is the first proposal for a hardware implementation of such functions within a *single device*. However, the networks we implemented in Chapter 6 are the second generation neural networks (will be discussed in section 7.1). In this chapter, we would like to mention the possible hardware implementation of other types of neural networks using transistor-like spin switches.

7.1 A brief-overview of neural network

The Artificial Neural Networks (ANN) are the collections of neurons so that overall they can mimic computations in the brain. After training properly, ANN can figure out by its own the solutions to the problems or it can learn from the experience

which is a form of intelligence. Mathematically, training data can be viewed as in the following [86]:

- For a given input X and an (label) output Y
- Learning (training) is to find a functional relationship between the input and the output

$$f : X \rightarrow Y \quad (7.1)$$

and sometime f is called a classifier.

ANN has been used for various applications such as pattern recognition, machine learning and data mining. Up to now, most of ANN are software-based models and it has been well accepted that hardware implementation of the (artificial) neuron network (NN) could have many advantages compared to software-based ANN [69, 70, 87].

ANN can be categorized into three different generations if one classifies NN basing on the activation function of the neuron [88]. The first generation is based on McCulloch-Pitts neurons (perceptrons or threshold neurons). Usually, the perception network has only one input and one output layer limiting it to only linear problems. Adding more layers (hidden) between input and output layers allows the network to handle non-linear problems such as pattern recognition and non-linear classification. The multi-layer perceptron neural networks include Hopfield nets, Boltzmann machines, etc... which belong to the first generation of neural networks. However, one of the characteristics of perceptron networks is that they only work with digital inputs and outputs. Also, it is very hard to train the step-like activation neurons since it has been known that a small change in the weights between the neurons could cause a big change in the outputs [89].

To overcome this problem, the second generation of NN came up with a smooth function of the activation function: the sigmoid function. The end result is that, a small change in the weights (or biases) will cause a small change in the output. As a result, we could modify the weights and biases so that the network now behaves



Fig. 7.1. Unlabeled data or multi-levels of representation of data. The picture could mean: it is a car, a man, a race, etc... with some probabilities.

the way it is supposed to. Moreover, the second generation NN supports Back-propagation training method [80] mentioned in section 6.2.3.

The third generation of NN, or spiking neural network where one of its main goals is to emulate and shed light on the operations and behaviour of the brain. Experimentally it has been known that the biology neurons fire at frequencies between their minimum and maximum values [90]. Similarly, spiking neurons were designed to produce spikes at various frequencies depending on the input signals. Unlike other types of neurons, spiking neurons store information in the frequencies and/or the time between the spikes. On top of that, the weights of synapses can be adjusted according to the activity of the neurons. This is the so-called spike-timing dependent plasticity (STDP) which is an important feature of the biological neuron.

In terms of computation, spiking neurons have been also used for pattern recognition and classification problems [91]. Until now, there has been a lot of research (most of them from the universities) on the hardware implementation for the spiking networks, where the main focus is the circuit design for producing the spikes and spike-timing dependent plasticity [69, 87, 91, 92].

7.1.1 Deep Belief Network

On the other hand, the importance and success of deep belief networks (DBN) are well established for data mining and machine learning applications [93]. DBN is the extension of the first and second generation of the neuron network where it deals with big data having huge amount of structure. So what is wrong with the second generation NN? First of all, back-propagation does not really work for big data. But a more serious problem is that the network requires the **labeled** training data (for example, letters in the character recognition mentioned in section 6.4). However, in the real world, most of data is **unlabeled** in the sense the data could have multiple meanings (multiple levels of representation). For example, a picture in Fig.7.1 could mean: a car, a man, a race, etc... and there could be more meanings about the picture if we even take into account the background and the context.

In order to train the NN dealing with unlabeled data, so far people have used the so-called deep network. Here deep simply means you have MANY hidden layers in the network compared to SHALLOW networks where they have only few hidden layers in the net. The series layers in deep network are used to break down a very complicated object (as in Fig.7.1) into much easier answerable questions. Before 2006, deep networks had not been very useful since nobody knew how to train them. Since 2006, many training techniques have been developed for the deep networks [94] and they currently are the best choice for pattern recognition, voice recognition, machine learning... [89].

So far we have discussed the deep network, what about the ‘belief’? Here belief simply means certainty or probability. Therefore, the belief network is a network where each neuron has its state as a stochastic or probabilistic variable. The probabilistic neuron allows the network to map an input data into multiple possible (probabilistic) outputs. Vice versa, given the output, the networks with stochastic neurons can construct what is the possibility of the input that causes the output. For example, when we look at a picture of a man driving a car as before, there is a possibility

that it is a race. Or given a patient having a cancer, what are the probabilities of the causes? In general, the belief networks are important for inference problems, making predictions and decisions.

Up to now, DBN are mainly software-based models of interacting networks of nodes (neurons) that have probabilistic logistic transfer function. These probabilistic nodes can also be connected to form directed networks as in Bayesian nets widely used for inference problems that investigate and address causes of observed effects [95]. It is generally accepted that more amenable hardware to these software models could have a significant impact on their widespread use as running such software on CPUs and GPUs is cumbersome and time consuming with some success reported in using FGPAs for such problems as compared to standard CMOS based hardware (see for example [96, 97]). But their use is also limited due to significant circuitry (hence large silicon landscape) needed to execute various essential and elemental functionalities such as emulating the logistic function, multiplication, addition and also circuit generation of uniformly distributed random bits.

Here we would like to establish that transistor-like spin switches can be used to implement the basic building block of deep belief network(DBN). To our knowledge, this is the first ever proposal for a hardware implementation of such a function with a single device, transistor based or otherwise. These active devices can be used as neurons having probabilistic logistic transfer function and possibly having many fan-outs(synapses). The interconnections can be either bidirectional or directional with strengths that can be tuned conveniently without the use of external amplifiers. Such circuits use one device per node for generation of logistic function with multiplication between the weights and internal state of device also done inherently at each device. Furthermore, addition (accumulation) occurs just by summing the currents at intersection of wire interconnect such as Cu. These devices and their circuits do not out-source the generation of random bits to external circuitry since they utilize ambient thermal fluctuations as source of random variations.

7.2 Implementation of the building block of DBN by transistor-like spin switches

7.2.1 Implementation of the stochastic sigmoid function

Given the importance of hardware implementation of the DBN, in this section we would like to propose a hardware implementation of the basic building block of (any) networks or the neurons having stochastic or probabilistic states using simulations based on an experimentally validated model.

Before going to the detail of the implementation, we should mention the main requirements of the hardware implementation of the neurons. As discussed in Chapter 6, the neurons should be able to perform summation, multiplication and activation function which normally requires extra circuitry in other hardware implementations. At the moment, transistor-like SS device seems to have advantages in building the neuron in the sense that it can do all the above operations in a single device by utilizing the facts that currents allow convenient summation of multiple inputs while the magnet provides the threshold function. Multiplication is simple due to the MTJ physics where the output current is proportional to the applied voltage V and the conductance of the MTJ which in turns is proportional to the state of the magnet x_{MTJ} : $I \sim VG_{MTJ} \sim Vx_{MTJ}$. On top of that, the neuron must have many fan-outs so that it can be used in typical network. One way to solve the fan-out problem for probabilistic neurons is a generic device shown in Fig.7.2(a) or Fig.6.2 mentioned in Chapter 6. The whole device can be viewed as a neuron having many synapse whose the weights are represented by the voltage V_i .

The new thing here is that ambient thermal fluctuations in these devices are used for generation of logistic transfer function representing probabilistic states of the device not requiring random bit generation circuits. The device performs the write (W) and read (R) operations by taking an input I_{IN} (which is the weighted sum of all previous units) and determining the *probabilities* of its state x_W or x_R being in the up or down directions. Then it sends an output current depending on both the state

(x_R) and the voltage V applied to it: $I_{OUT} \sim Vx_R$. Here we assume that, in average, all the W and R in the neurons have the same transfer characteristic functions. In other words, the probability of being in the state 1 of the unit Ri for a given input current I_{in} , namely $P(x_{Ri} = 1|I_{in})$, is the same for all R units in the Fig.7.2(a). Interconnections between various devices can be either bidirectional or unidirectional with strengths that can be tuned conveniently.

Fig.7.2(b) shows the simulations for the probabilistic logistic function for one of the W/R units in Fig.7.2(a) (note that all of them in average behave the same way). It calculates the probability of the state of the magnet in R unit to be in the "up" or 1 direction for a given input current I_{in} , namely $P(x_R = 1|I_{in})$ (note that $P(x_R = -1|I_{in}) = 1 - P(x_R = 1|I_{in})$). In Fig.7.2(b), the probability values are obtained by averaging over many trials (10000 in this case) in presence of ambient thermal fluctuations for each input current value I_{in} normalized by the critical switching current (I_c) of the W/R unit. Each trial starts with the magnetizations of both W and R in Fig.2.3 aligning along their hard axis by applying an external magnetic. The device is then left to relax to a binary final state under the influence of input current. The simulations with thermal noise are described in the appendix D.

7.3 Stochastic Spin Switch NN implementation for a Bayesian network

Now we would like to establish the operation of DBN SS neural network using a standard simulation model based on coupled LLG equations, one for each magnet in the network. The neurons in Fig.7.2(a) can represent nodes in a Bayesian network interconnected with unidirectional connections representing causal influences with their synaptic properties governing the interaction between various nodes. Fig.7.3(a) shows a typical example of a Bayesian network where we have a system of three units namely: Rain, Sprinkler and Lawn. The question we are looking for is: given the fact that Lawn is wet, what is the likelihood that it is due to Rain or Sprinkler? The

problem definition also involves the Rain to have a causal influence on Sprinkler, for example, when it rains, it is most likely that the Sprinkler has to be OFF.

Table 7.1

Conditional probability tables among Rain, Sprinkler and Lawn. Here 1 presents the ON state while -1 is the OFF state. The tables were obtained by taking average over 10000 trials of LLG simulations for the network in Fig.7.3(b) where the electrical signals are given in Table.7.2

			Sprinkler			Lawn			
Rain	1	-1	Rain	1	-1	Rain	Sprinkler	1	-1
Probability	0.2	0.8	1	0	1	1	1	1	0
			-1	0.6	0.4	1	-1	0.7	0.3
						-1	1	0.8	0.2
						-1	-1	0.96	0.04

To address the question, we first need to know the conditional probabilities among Rain, Sprinkler and Lawn, for example the ones shown in table 7.1. These values simply tell us the effects that Rain causes on Sprinkler and/or Lawn, Sprinkler and Rain on Lawn, etc... For example, when it rains, the Sprinkler is OFF and when it does not rain, the sprinkler is ON with some probability. Similarly, the Lawn should be wet when both Rain and Sprinkler are ON and so on. It is the conditional probability that decides what is the cause of the wet Lawn. In software implementation of the Bayesian network, these values are given before hand so that the network can make decisions.

Here we would like to demonstrate that (via LLG simulations) the values in Table 7.1 can be obtained by a **hardware** stochastic Spin Switch network shown in Fig.7.3(b) with the electrical values (voltages and bias currents) given in the table 7.2. The probability values are obtained by averaging over many trials (10000) of the

Table 7.2

Electrical values used in Fig.7.3(b) to produce the conditional probabilities in table 7.1. The values are normalized by threshold voltage or threshold current.

Electrical	Normalized value
V_{RS}	1
V_{RL}	-0.9
V_{SL}	-1
I_{bR}	0.1
I_{bS}	0.95
I_{bL}	-0.45

Table 7.3

Inference can be made based on the conditional probabilities values in table 7.1

Lawn is wet	Likelihood
Due to Rain	$P(L=1 R=1)=0.38$
Due to Sprinkler	$P(L=1 S=1)=0.56$

final states of Rain, Sprinkler and Lawn neurons in the network. In each trial, all the magnets are initially put in the hard axis and the system is relaxed to a state where the m_z of Read units at each neuron are recorded: $\{m_z^{Rain}, m_z^{Sprinkler}, m_z^{Lawn}\}$. Then the conditional probability tables are obtained by simply counting the states.

Now the decision or inference, given in Table 7.3, can be made based on the conditional probabilities. For example, the probability that the Lawn is wet due to Rain is the following (here Rain=R, Sprinkler=S and Lawn=L):

$$P(L = 1|R = 1) = \frac{P(R = 1, S = 1, L = 1) + P(R = 1, S = -1, L = 1)}{\text{total probability that Rain is ON}} \quad (7.2)$$

where

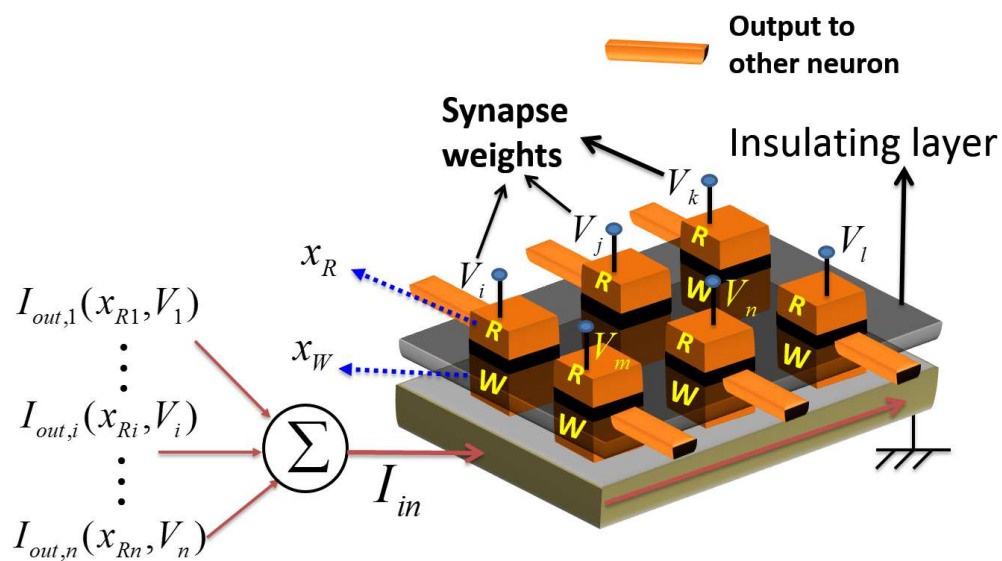
$$\begin{aligned} \text{total probability that Rain is ON} = \\ P(R = 1, S = 1, L = 1) + P(R = 1, S = -1, L = 1) \\ + P(R = 1, S = 1, L = -1) + P(R = 1, S = -1, L = -1) \end{aligned} \quad (7.3)$$

7.4 Summary

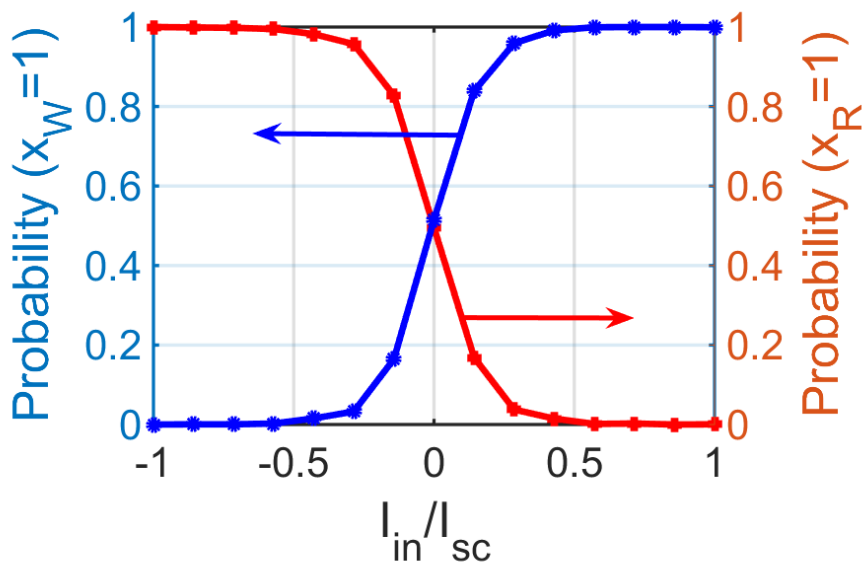
In this chapter, we have reviewed different types of artificial neural network and discussed in detail the hardware implementation of *stochastic* neurons (having many synapses) in deep belief network by using transistor-like spin switches. To our knowledge, this is the first ever proposal for a hardware implementation of such functions within a *single device*. The interconnections can be either bidirectional or unidirectional with strengths that can be tuned conveniently without the use of external amplifiers. Furthermore, we have demonstrated the operation of Bayesian SS neural network by solving standard coupled LLG equations, one for each magnet in the network.

The matlab codes used to generate the figures can be found at:

<https://drive.google.com/open?id=0B9ggzdMPbfz4VDdld0xPc19ldm8&authuser=0>

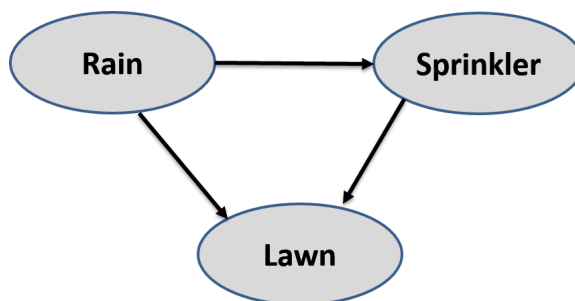


(a)

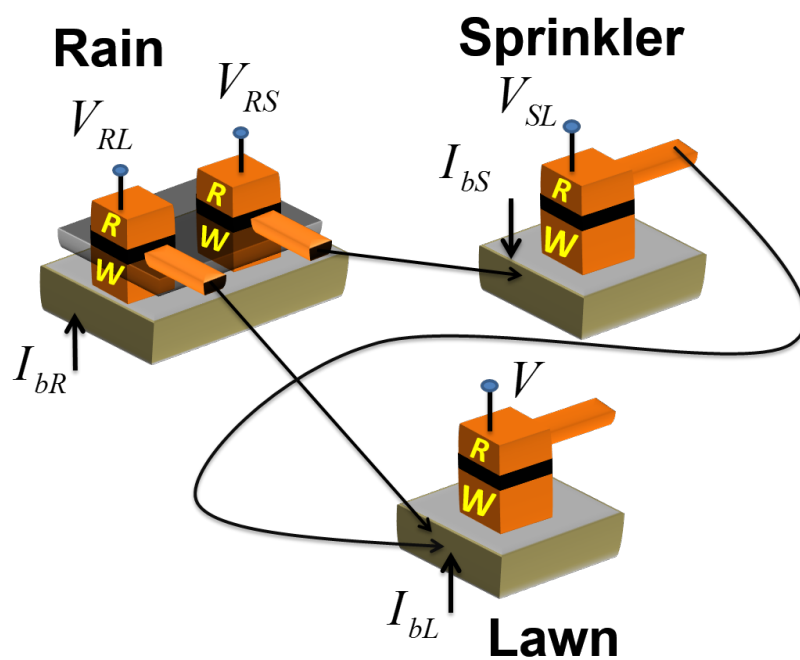


(b)

Fig. 7.2. a) A transistor like device used for hardware implementation of the stochastic neurons having many synapses. b) The probabilistic logistic function for the device where the simulations are done for Spin Switch devices.



(a)



(b)

Fig. 7.3. a) A simple Bayesian network for inference problem: Rain, Sprinkler and Lawn. The Rain has direct influence on the Sprinkler: when the Rain is ON, the Sprinkler is OFF. Given a wet Lawn, what is the likelihood that it is due to Rain or Sprinkler? b) The proposed hardware implementation of the Bayesian network based on probabilistic SS.

LIST OF REFERENCES

LIST OF REFERENCES

- [1] W. Haensch, E. J. Nowak, R. H. Dennard, P. M. Solomon, A. Bryant, O. H. Dokumaci, A. Kumar, X. Wang, J. B. Johnson, and M. V. Fischetti, "Silicon CMOS devices beyond scaling," *IBM Journal of Research and Development*, vol. 50, pp. 339–361, July 2006.
- [2] T. N. Theis and P. M. Solomon, "In Quest of the Next Switch: Prospects for Greatly Reduced Power Dissipation in a Successor to the Silicon Field-Effect Transistor," *Proceedings of the IEEE*, vol. 98, pp. 2005–2014, Dec. 2010.
- [3] K. Bernstein, R. K. Cavin, W. Porod, A. Seabaugh, and J. Welser, "Device and Architecture Outlook for Beyond CMOS Switches," *Proceedings of the IEEE*, vol. 98, pp. 2169–2184, Dec. 2010.
- [4] G. Bourianoff and D. E. Nikonov, "Progress, Opportunities and Challenges for Beyond CMOS Information Processing Technologies," *ECS Transactions*, vol. 35, no. 2, pp. 43–53, 2011.
- [5] D. E. Nikonov and I. A. Young, "Uniform methodology for benchmarking beyond-CMOS logic devices," in *2012 International Electron Devices Meeting*, pp. 25.4.1–25.4.4, IEEE, Dec. 2012.
- [6] A. Sarkar, D. E. Nikonov, I. A. Young, B. Behin-Aein, and S. Datta, "Charge-Resistance Approach to Benchmarking Performance of Beyond-CMOS Information Processing Devices," *arXiv:1308.4748 [cond-mat.mes-hall]*, Aug. 2013.
- [7] S. Datta, D. Vinh, and B. Behin-Aein, *What constitutes a nanoswitch: A perspective*. Ltd. Published 2014 by John Wiley & Sons, 2015.
- [8] M. Z. Hasan and C. L. Kane, "Colloquium: Topological insulators," *Reviews of Modern Physics*, vol. 82, pp. 3045–3067, Nov. 2010.
- [9] Y. Ando, "Topological Insulator Materials," *Journal of the Physical Society of Japan*, vol. 82, p. 102001, Oct. 2013.
- [10] C. H. Li, O. M. J. van 't Erve, J. T. Robinson, Y. Liu, L. Li, and B. T. Jonker, "Electrical detection of charge-current-induced spin polarization due to spin-momentum locking in Bi₂Se₃," *Nature nanotechnology*, vol. 9, pp. 218–24, Mar. 2014.
- [11] S. Hong, V. Diep, S. Datta, and Y. P. Chen, "Modeling potentiometric measurements in topological insulators including parallel channels," *Physical Review B*, vol. 86, p. 085131, Aug. 2012.

- [12] T. Maruyama, Y. Shiota, T. Nozaki, K. Ohta, N. Toda, M. Mizuguchi, A. A. Tulapurkar, T. Shinjo, M. Shiraishi, S. Mizukami, Y. Ando, and Y. Suzuki, "Large voltage-induced magnetic anisotropy change in a few atomic layers of iron.," *Nature nanotechnology*, vol. 4, pp. 158–61, Mar. 2009.
- [13] L. Q. Liu, C. F. Pai, Y. Li, H. W. Tseng, D. C. Ralph, and R. A. Buhrman, "Spin-Torque Switching with the Giant Spin Hall Effect of Tantalum," *Science*, vol. 336, p. 555, 2012.
- [14] V. Q. Diep and S. Datta, "The spin switch oscillator: A new approach based on gain and feedback," in *72nd Device Research Conference*, pp. 293–294, IEEE, June 2014.
- [15] V. Diep, B. Sutton, S. Datta, B. Behin-Aein, V. Quang Diep, B. Sutton, B. Behin-Aein, and S. Datta, "Spin switches for compact implementation of neuron and synapse," *Applied Physics Letters*, vol. 104, p. 222405, June 2014.
- [16] L. Liu, O. J. Lee, T. J. Gudmundsen, D. C. Ralph, and R. A. Buhrman, "Current-Induced Switching of Perpendicularly Magnetized Magnetic Layers Using Spin Torque from the Spin Hall Effect," *Physical Review Letters*, vol. 109, no. 9, p. 96602, 2012.
- [17] S. Datta, S. Salahuddin, and B. Behin-Aein, "Non-volatile spin switch for Boolean and non-Boolean logic," *Applied Physics Letters*, vol. 101, no. 25, p. 252411, 2012.
- [18] A. D. Kent and D. C. Worledge, "A new spin on magnetic memories.," *Nature nanotechnology*, vol. 10, pp. 187–191, Mar. 2015.
- [19] J. Slonczewski, "Current-driven excitation of magnetic multilayers," *Journal of Magnetism and Magnetic Materials*, vol. 159, pp. L1–L7, June 1996.
- [20] L. Berger, "Emission of spin waves by a magnetic multilayer traversed by a current," *Physical Review B*, vol. 54, pp. 9353–9358, Oct. 1996.
- [21] J. Sun, "Spin-current interaction with a monodomain magnetic body: A model study," *Physical Review B*, vol. 62, pp. 570–578, July 2000.
- [22] D. Ralph and M. Stiles, "Spin transfer torques," *Journal of Magnetism and Magnetic Materials*, vol. 320, pp. 1190–1216, Apr. 2008.
- [23] M. Julliere, "Tunneling between ferromagnetic films," *Physics Letters A*, vol. 54, pp. 225–226, Sept. 1975.
- [24] W. Butler, X.-G. Zhang, T. Schulthess, and J. MacLaren, "Spin-dependent tunneling conductance of Fe—MgO—Fe sandwiches," *Physical Review B*, vol. 63, p. 054416, Jan. 2001.
- [25] S. Ikeda, J. Hayakawa, Y. Ashizawa, Y. M. Lee, K. Miura, H. Hasegawa, M. Tsunoda, F. Matsukura, and H. Ohno, "Tunnel magnetoresistance of 604% at 300K by suppression of Ta diffusion in CoFeBMgOCoFeB pseudo-spin-valves annealed at high temperature," *Applied Physics Letters*, vol. 93, p. 082508, Aug. 2008.

- [26] I. M. Miron, K. Garello, G. Gaudin, P. J. Zermatten, M. V. Costache, S. Auffret, S. Bandiera, B. Rodmacq, A. Schuhl, and P. Gambardella, “Perpendicular switching of a single ferromagnetic layer induced by in-plane current injection,” *Nature*, vol. 476, no. 7359, pp. 189–U88, 2011.
- [27] B. Behin-Aein, D. Datta, S. Salahuddin, and S. Datta, “Proposal for an all-spin logic device with built-in memory,” *Nature nanotechnology*, vol. 5, pp. 266–70, Apr. 2010.
- [28] S. Srinivasan, A. Sarkar, B. Behin-Aein, and S. Datta, “All-Spin Logic Device With Inbuilt Nonreciprocity,” *IEEE Transactions on Magnetics*, vol. 47, pp. 4026–4032, Oct. 2011.
- [29] D. Morris, D. Bromberg, Jian-Gang Zhu, and L. Pileggi, “mLogic: Ultra-low voltage non-volatile logic circuits using STT-MTJ devices,” *Design Automation Conference (DAC), 2012 49th ACM/EDAC/IEEE*, pp. 486–491, 2012.
- [30] K. L. Wang, J. G. Alzate, and P. Khalili Amiri, “Low-power non-volatile spintronic memory: STT-RAM and beyond,” *Journal of Physics D: Applied Physics*, vol. 46, p. 074003, Feb. 2013.
- [31] J. T. Heron, M. Trassin, K. Ashraf, M. Gajek, Q. He, S. Y. Yang, D. E. Nikonov, Y.-H. Chu, S. Salahuddin, and R. Ramesh, “Electric-Field-Induced Magnetization Reversal in a Ferromagnet-Multiferroic Heterostructure,” *Physical Review Letters*, vol. 107, p. 217202, Nov. 2011.
- [32] R. P. Cowburn and M. E. Welland, “Room Temperature Magnetic Quantum Cellular Automata,” *Science*, vol. 287, pp. 1466–1468, Feb. 2000.
- [33] A. Imre, G. Csaba, L. Ji, A. Orlov, G. H. Bernstein, and W. Porod, “Majority logic gate for magnetic quantum-dot cellular automata,” *Science (New York, N.Y.)*, vol. 311, pp. 205–8, Jan. 2006.
- [34] M. T. Niemier, G. H. Bernstein, G. Csaba, A. Dingler, X. S. Hu, S. Kurtz, S. Liu, J. Nahas, W. Porod, M. Siddiq, and E. Varga, “Nanomagnet logic: progress toward system-level integration,” *Journal of physics. Condensed matter : an Institute of Physics journal*, vol. 23, p. 493202, Dec. 2011.
- [35] M. T. Alam, S. J. Kurtz, M. A. J. Siddiq, M. T. Niemier, G. H. Bernstein, X. S. Hu, and W. Porod, “On-Chip Clocking of Nanomagnet Logic Lines and Gates,” *IEEE Transactions on Nanotechnology*, vol. 11, pp. 273–286, Mar. 2012.
- [36] M. Colci and M. Johnson, “Dipolar Coupling Between Nanopillar Spin Valves and Magnetic Quantum Cellular Automata Arrays,” *IEEE Transactions on Nanotechnology*, vol. 12, pp. 824–830, Sept. 2013.
- [37] R. Skomski and J. Coey, “Giant energy product in nanostructured two-phase magnets,” *Physical Review B*, vol. 48, pp. 15812–15816, Dec. 1993.
- [38] E. E. Fullerton, J. S. Jiang, M. Grimsditch, C. H. Sowers, and S. D. Bader, “Exchange-spring behavior in epitaxial hard/soft magnetic bilayers,” *Physical Review B*, vol. 58, pp. 12193–12200, Nov. 1998.
- [39] E. E. Fullerton, J. Jiang, and S. Bader, “Hard/soft magnetic heterostructures: model exchange-spring magnets,” *Journal of Magnetism and Magnetic Materials*, vol. 200, pp. 392–404, Oct. 1999.

- [40] R. Victora, "Composite media for perpendicular magnetic recording," *IEEE Transactions on Magnetism*, vol. 41, pp. 537–542, Feb. 2005.
- [41] D. Bhowmik, L. You, and S. Salahuddin, "Spin Hall effect clocking of nanomagnetic logic without a magnetic field.," *Nature nanotechnology*, vol. 9, pp. 59–63, Jan. 2014.
- [42] A. Singh, O. Mryasov, S. Gupta, S. Okatov, K. Gao, and E. Girt, "Micro Magnetic Exchange Interaction Tensor and Magnetization Reversal of FePt Based Alloy Thin Film Nano-Structures," *IEEE Transactions on Magnetism*, vol. 49, pp. 3799–3801, July 2013.
- [43] A. J. Newell, W. Williams, and D. J. Dunlop, "A generalization of the demagnetizing tensor for nonuniform magnetization," *Journal of Geophysical Research: Solid Earth*, vol. 98, no. B6, pp. 9551–9555, 1993.
- [44] K. Miura, S. Ikeda, M. Yamanouchi, H. Yamamoto, K. Mizunuma, H. Gan, J. Hayakawa, R. Koizumi, F. Matsukura, and H. Ohno, "CoFeB/MgO based perpendicular magnetic tunnel junctions with stepped structure for symmetrizing different retention times of 0 and 1 information," 2011.
- [45] Y.-H. Wang, S.-H. Huang, D.-Y. Wang, K.-H. Shen, C.-W. Chien, K.-M. Kuo, S.-Y. Yang, and D.-L. Deng, "Impact of stray field on the switching properties of perpendicular MTJ for scaled MRAM," in *2012 International Electron Devices Meeting*, pp. 29.2.1–29.2.4, IEEE, Dec. 2012.
- [46] C.-F. Pai, L. Liu, Y. Li, H. W. Tseng, D. C. Ralph, and R. A. Buhrman, "Spin transfer torque devices utilizing the giant spin Hall effect of tungsten," *Applied Physics Letters*, vol. 101, no. 12, p. 122404, 2012.
- [47] Y. Niimi, Y. Kawanishi, D. Wei, C. Deranlot, H. Yang, M. Chshiev, T. Valet, A. Fert, and Y. Otani, "Giant Spin Hall Effect Induced by Skew Scattering from Bismuth Impurities inside Thin Film CuBi Alloys," *Physical Review Letters*, vol. 109, pp. 1–5, Oct. 2012.
- [48] J.-G. J. Zhu and C. Park, "Magnetic tunnel junctions," *Materials Today*, vol. 9, pp. 36–45, Nov. 2006.
- [49] A. V. Khvalkovskiy, D. Apalkov, S. Watts, R. Chepulskii, R. S. Beach, A. Ong, X. Tang, A. Driskill-Smith, W. H. Butler, P. B. Visscher, D. Lottis, E. Chen, V. Nikitin, and M. Krounbi, "Basic principles of STT-MRAM cell operation in memory arrays," *Journal of Physics D: Applied Physics*, vol. 46, p. 074001, Feb. 2013.
- [50] W. G. Wang and C. L. Chien, "Voltage-induced switching in magnetic tunnel junctions with perpendicular magnetic anisotropy," *Journal of Physics D: Applied Physics*, vol. 46, p. 074004, Feb. 2013.
- [51] S. Ikeda, K. Miura, H. Yamamoto, K. Mizunuma, H. D. Gan, M. Endo, S. Kanai, J. Hayakawa, F. Matsukura, and H. Ohno, "A perpendicular-anisotropy CoFeB-MgO magnetic tunnel junction.," *Nature materials*, vol. 9, pp. 721–4, Sept. 2010.

- [52] D. C. Worledge, G. Hu, D. W. Abraham, J. Z. Sun, P. L. Trouilloud, and J. Nowak, "Spin torque switching of perpendicular TaCoFeBMgO-based magnetic tunnel junctions Spin torque switching of perpendicular Ta CoFeB MgO-based magnetic tunnel junctions," vol. 022501, no. 2011, 2012.
- [53] D. C. Worledge, G. Hu, D. W. Abraham, P. L. Trouilloud, and S. Brown, "Development of perpendicularly magnetized Ta—CoFeB—MgO-based tunnel junctions at IBM (invited)," *Journal of Applied Physics*, vol. 115, p. 172601, May 2014.
- [54] M. Gajek, J. J. Nowak, J. Z. Sun, P. L. Trouilloud, E. J. OSullivan, D. W. Abraham, M. C. Gaidis, G. Hu, S. Brown, Y. Zhu, R. P. Robertazzi, W. J. Gallagher, and D. C. Worledge, "Spin torque switching of 20nm magnetic tunnel junctions with perpendicular anisotropy," *Applied Physics Letters*, vol. 100, no. 13, p. 132408, 2012.
- [55] N. Derby and S. Olbert, "Cylindrical magnets and ideal solenoids," *American Journal of Physics*, vol. 78, no. 3, p. 229, 2010.
- [56] N. Nishimura, T. Hirai, A. Koganei, T. Ikeda, K. Okano, Y. Sekiguchi, and Y. Osada, "Magnetic tunnel junction device with perpendicular magnetization films for high-density magnetic random access memory," *Journal of Applied Physics*, vol. 91, p. 5246, Mar. 2002.
- [57] J. L. Leal and M. H. Kryder, "Spin valves exchange biased by Co/Ru/Co synthetic antiferromagnets," *Journal of Applied Physics*, vol. 83, p. 3720, Apr. 1998.
- [58] S. Bandiera, R. C. Sousa, Y. Dahmane, C. Ducruet, C. Portemont, V. Baltz, S. Auffret, I. L. Prejbeanu, and B. Dieny, "Comparison of Synthetic Antiferromagnets and Hard Ferromagnets as Reference Layer in Magnetic Tunnel Junctions With Perpendicular Magnetic Anisotropy," *IEEE Magnetism Letters*, vol. 1, pp. 3000204–3000204, 2010.
- [59] S. Mangin, Y. Henry, D. Ravelosona, J. a. Katine, and E. E. Fullerton, "Reducing the critical current for spin-transfer switching of perpendicularly magnetized nanomagnets," *Applied Physics Letters*, vol. 94, no. 1, p. 012502, 2009.
- [60] K. Yakushiji, T. Saruya, H. Kubota, A. Fukushima, T. Nagahama, S. Yuasa, and K. Ando, "Ultrathin Co/Pt and Co/Pd superlattice films for MgO-based perpendicular magnetic tunnel junctions," *Applied Physics Letters*, vol. 97, p. 232508, Dec. 2010.
- [61] F. J. A. den Broeder, H. C. Donkersloot, H. J. G. Draaisma, and W. J. M. de Jonge, "Magnetic properties and structure of Pd/Co and Pd/Fe multilayers," *Journal of Applied Physics*, vol. 61, p. 4317, Apr. 1987.
- [62] P. Carcia, A. Suna, D. Onn, and R. van Antwerp, "Structural, magnetic, and electrical properties of thin film Pd/Co layered structures," *Superlattices and Microstructures*, vol. 1, pp. 101–109, Jan. 1985.
- [63] S. Pal, B. Rana, O. Hellwig, T. Thomson, and a. Barman, "Tunable magnonic frequency and damping in [Co/Pd]₈ multilayers with variable Co layer thickness," *Applied Physics Letters*, vol. 98, no. 8, p. 082501, 2011.

- [64] J. Z. Sun, R. P. Robertazzi, J. Nowak, P. L. Trouilloud, G. Hu, D. W. Abraham, M. C. Gaidis, S. L. Brown, E. J. OSullivan, W. J. Gallagher, and D. C. Worledge, "Effect of subvolume excitation and spin-torque efficiency on magnetic switching," *Physical Review B*, vol. 84, p. 064413, Aug. 2011.
- [65] Stephen E. Russek, W. H. Rippard, T. Cecil, and R. Heindl, *Handbook of Nanophysics: Functional Nanomaterials*. CRC Press, Chap. 38, 2010.
- [66] Z. Zeng, G. Finocchio, B. Zhang, P. Khalili Amiri, J. a. Katine, I. N. Krivorotov, Y. Huai, J. Langer, B. Azzerboni, K. L. Wang, and H. Jiang, "Ultralow-current-density and bias-field-free spin-transfer nano-oscillator.," *Scientific reports*, vol. 3, p. 1426, Jan. 2013.
- [67] L. Liu, C.-F. Pai, D. C. Ralph, and R. a. Buhrman, "Magnetic Oscillations Driven by the Spin Hall Effect in 3-Terminal Magnetic Tunnel Junction Devices," *Physical Review Letters*, vol. 109, p. 186602, Oct. 2012.
- [68] C.-C. Lin, A. V. Penumatcha, Y. Gao, V. Q. Diep, J. Appenzeller, and Z. Chen, "Spin Transfer Torque in Graphene Lateral Spin Valve Assisted by External Magnetic Field.," *Nano letters*, vol. 13, p. 5177, Oct. 2013.
- [69] C.-S. Poon and K. Zhou, "Neuromorphic silicon neurons and large-scale neural networks: challenges and opportunities.," *Frontiers in neuroscience*, vol. 5, p. 108, Jan. 2011.
- [70] J. Misra and I. Saha, "Artificial neural networks in hardware: A survey of two decades of progress," *Neurocomputing*, vol. 74, pp. 239–255, Dec. 2010.
- [71] M. Di Ventra and Y. V. Pershin, "The parallel approach," *Nature Physics*, vol. 9, pp. 200–202, Apr. 2013.
- [72] N. Locatelli, V. Cros, and J. Grollier, "Spin-torque building blocks.," *Nature materials*, vol. 13, pp. 11–20, Jan. 2014.
- [73] X. Wang, Y. Chen, H. Xi, H. Li, and D. Dimitrov, "Spintronic Memristor Through Spin-Torque-Induced Magnetization Motion," *IEEE Electron Device Letters*, vol. 30, pp. 294–297, Mar. 2009.
- [74] S. Mrigank, C. Augustine, G. Panagopoulos, and K. Roy, "Spin Based Neuron-Synapse Module for Ultra Low Power," *WCCI 2012 IEEE World Congress on Computational Intelligence*, pp. 10–15, 2012.
- [75] H. Zhao, A. Lyle, Y. Zhang, P. K. Amiri, G. Rowlands, Z. Zeng, J. Katine, H. Jiang, K. Galatsis, K. L. Wang, I. N. Krivorotov, and J.-P. Wang, "Low writing energy and sub nanosecond spin torque transfer switching of in-plane magnetic tunnel junction for spin torque transfer random access memory," *Journal of Applied Physics*, vol. 109, p. 07C720, Mar. 2011.
- [76] T. Tanaka, H. Kontani, M. Naito, T. Naito, D. S. Hirashima, K. Yamada, and J. Inoue, "Intrinsic spin Hall effect and orbital Hall effect in 4d and 5d transition metals," *Physical Review B*, vol. 77, no. 16, p. 16, 2008.
- [77] B. Zamanlooy and M. Mirhassani, "Efficient hardware implementation of threshold neural networks," in *New Circuits and Systems Conference (NEW-CAS), 2012 IEEE 10th International*, pp. 1–4, IEEE, June 2012.

- [78] P. K. AMIRI and K. L. WANG, “VOLTAGE-CONTROLLED MAGNETIC ANISOTROPY IN SPINTRONIC DEVICES,” *SPIN*, vol. 02, p. 1240002, Sept. 2012.
- [79] L. Liu, C.-F. Pai, D. C. Ralph, and R. A. Buhrman, “Gate voltage modulation of spin-Hall-torque-driven magnetic switching,” *arXiv:1209.0962 [cond-mat.mtrl-sci]*, Sept. 2012.
- [80] D. Rumelhart, G. Hinton, and W. RJ, “Learning representations by back-propagating errors,” *Nature*, vol. 323, no. 9, p. 533, 1986.
- [81] M. Jabri and B. Flower, “Weight Perturbation: An Optimal Architecture and Learning Technique for Analog VLSI Feedforward and Recurrent Multilayer Networks,” *IEEE TRANSACTIONS ON NEURAL NETWORKS*, vol. 3, no. 1, pp. 154–157, 1992.
- [82] G. Huang, Q. Zhu, and K. Mao, “Can threshold networks be trained directly?,” *IEEE TRANSACTIONS ON CIRCUITS AND SYSTEMS*, vol. 53, no. 3, pp. 187–191, 2006.
- [83] C. Diorio, P. Hasler, B. A. Minch, and C. Mead, “A Single-Transistor Silicon Synapse,” *IEEE TRANSACTIONS ON ELECTRON DEVICES*, vol. 43, no. 11, pp. 1–9, 1996.
- [84] V. Srinivasan, D. W. Graham, and P. Hasler, “Floating-gates transistors for precision analog circuit design: an overview,” 2005.
- [85] L. A. Chen and P. Hasler, “Basics of floating-gate low-dropout voltage regulators,” 2000.
- [86] V. N. Vapnik, *Statistical Learning Theory*. 1998.
- [87] G. Indiveri, B. Linares-Barranco, T. J. Hamilton, A. van Schaik, R. Etienne-Cummings, T. Delbruck, S.-C. Liu, P. Dudek, P. Häfliger, S. Renaud, J. Schemmel, G. Cauwenberghs, J. Arthur, K. Hynna, F. Folowosele, S. Saighi, T. Serrano-Gotarredona, J. Wijekoon, Y. Wang, and K. Boahen, “Neuromorphic silicon neuron circuits,” *Frontiers in neuroscience*, vol. 5, p. 73, Jan. 2011.
- [88] W. Maass, “Networks of spiking neurons: The third generation of neural network models,” *Neural Networks*, vol. 10, no. 9, pp. 1659–1671, 1997.
- [89] M. A. Nielsen, “Neural Networks and Deep Learning,” 2015.
- [90] J. Krüger and F. Aiple, “Multimicroelectrode investigation of monkey striate cortex: spike train correlations in the infragranular layers,” *Journal of neurophysiology*, vol. 60, pp. 798–828, Aug. 1988.
- [91] S. Ghosh-Dastidar and H. Adeli, “Spiking neural networks,” *International journal of neural systems*, vol. 19, pp. 295–308, Aug. 2009.
- [92] Y. V. Pershin and M. Di Ventra, “Experimental demonstration of associative memory with memristive neural networks,” *Neural networks*, vol. 23, pp. 881–6, Oct. 2010.
- [93] J. Schmidhuber, “Deep learning in neural networks: An overview,” *Neural Networks*, vol. 61, pp. 85–117, Oct. 2014.

- [94] G. E. Hinton, S. Osindero, and Y.-W. Teh, “A fast learning algorithm for deep belief nets.,” *Neural computation*, vol. 18, pp. 1527–54, July 2006.
- [95] J. Pearl, “CAUSALITY: MODELS, REASONING, AND INFERENCE Cambridge University Press, 2000,” 2003.
- [96] S. K. Kim, P. L. McMahon, and K. Olukotun, “A Large-Scale Architecture for Restricted Boltzmann Machines,” in *2010 18th IEEE Annual International Symposium on Field-Programmable Custom Computing Machines*, pp. 201–208, IEEE, 2010.
- [97] D. L. Ly and P. Chow, “High-performance reconfigurable hardware architecture for restricted Boltzmann machines.,” *IEEE transactions on neural networks / a publication of the IEEE Neural Networks Council*, vol. 21, pp. 1780–92, Nov. 2010.
- [98] R. Sugano, M. Ichimura, S. Takahashi, and S. Maekawa, “Three dimensional simulations of spin Hall effect in magnetic nanostructures,” *Journal of Applied Physics*, vol. 103, no. 7, p. 3, 2008.
- [99] S. Zhang, “Spin Hall Effect in the Presence of Spin Diffusion,” *Physical Review Letters*, vol. 85, pp. 393–396, July 2000.
- [100] R. Engel-Herbert and T. Hesjedal, “Calculation of the magnetic stray field of a uniaxial magnetic domain,” *Journal of Applied Physics*, vol. 97, no. 7, p. 074504, 2005.
- [101] M. Benidir and B. Picinbono, “Extended table for eliminating the singularities in Routh’s array,” *IEEE Transactions on Automatic Control*, vol. 35, no. 2, pp. 218–222, 1990.
- [102] Z. Li and S. Zhang, “Magnetization dynamics with a spin-transfer torque,” *Physical Review B*, vol. 68, p. 024404, July 2003.
- [103] Z. Li and S. Zhang, “Thermally assisted magnetization reversal in the presence of a spin-transfer torque,” *Physical Review B*, vol. 69, p. 134416, Apr. 2004.
- [104] J. Z. Sun, “Spin angular momentum transfer in current-perpendicular nanomagnetic junctions,” *IBM Journal of Research and Development*, vol. 50, pp. 81–100, Jan. 2006.
- [105] W. Scholz, T. Schrefl, and J. Fidler, “Micromagnetic simulation of thermally activated switching in fine particles,” *Journal of Magnetism and Magnetic Materials*, vol. 233, pp. 296–304, Aug. 2001.
- [106] J. García-Palacios and F. Lázaro, “Langevin-dynamics study of the dynamical properties of small magnetic particles,” *Physical Review B*, vol. 58, pp. 14937–14958, Dec. 1998.
- [107] J.-G. Zhu, “Thermal magnetic noise and spectra in spin valve heads,” *Journal of Applied Physics*, vol. 91, p. 7273, May 2002.

APPENDICES

A. SIMPLE MODEL FOR GSHE

A.1 Drift-diffusion model for GSHE

We would like to derive the Eq.(2.4) in 2D:

$$J_s = \theta_H J_c \left(1 - \operatorname{sech}(d/\lambda_{sf})\right) \approx \theta_H J_c$$

Here are the two things that we need to prove first:

1. The relation between the current density with the electro-chemical potential in 2D for spin hall effect (SHE) and inverse spin hall effect (ISHE)

$$\begin{bmatrix} J_x^c \\ J_y^s \end{bmatrix} = \frac{\sigma_{xx}}{2q} \begin{bmatrix} 1 & \theta_H \\ -\theta_H & 1 \end{bmatrix} \begin{bmatrix} \partial_x \mu_c \\ \partial_y \mu_s \end{bmatrix} \quad \text{(SHE)} \quad (\text{A.1})$$

$$\begin{bmatrix} J_x^s \\ J_y^c \end{bmatrix} = \frac{\sigma_{xx}}{2q} \begin{bmatrix} 1 & \theta_H \\ -\theta_H & 1 \end{bmatrix} \begin{bmatrix} \partial_x \mu_s \\ \partial_y \mu_c \end{bmatrix} \quad \text{(ISHE)} \quad (\text{A.2})$$

where θ_H is the hall angle. And σ_{xx} is the conductivity of the material.

2. The drift-diffusion equations that govern the GSHE material in 2D

$$\begin{aligned} \frac{\partial^2 \mu_c}{\partial^2 x} + \frac{\partial^2 \mu_c}{\partial^2 y} &= 0 \\ \frac{\partial^2 \mu_s}{\partial^2 x} + \frac{\partial^2 \mu_s}{\partial^2 y} &= \frac{1}{\lambda_{sf}^2} \mu_s \end{aligned} \quad (\text{A.3})$$

where μ_c and μ_s are the charge and spin electro-chemical potential respectively.

λ_{sf} is the spin flip scattering length for the material.

We start with the general definition of current density:

$$\vec{J} = \frac{\sigma}{q} \vec{\nabla} \mu = \frac{\sigma}{q} \left(\frac{\partial \mu}{\partial x} \hat{x} + \frac{\partial \mu}{\partial y} \hat{y} \right)$$

In form of matrix:

$$\begin{bmatrix} J_x \\ J_y \end{bmatrix} = \frac{\sigma_{2 \times 2}}{q} \begin{bmatrix} \partial_x \mu \\ \partial_y \mu \end{bmatrix}$$

For GSHE material, we assume that the conductivity is a matrix with following form:

$$\begin{bmatrix} J_x \\ J_y \end{bmatrix} = \frac{1}{q} \begin{bmatrix} \sigma_{xx} & \sigma_{xy} \\ -\sigma_{xy} & \sigma_{yy} \end{bmatrix} \begin{bmatrix} \partial_x \mu \\ \partial_y \mu \end{bmatrix}$$

Let us define $\theta_H = \sigma_{xy}/\sigma_{xx}$, and notice that up spin and down spin have opposited sign of θ_H . The above matrix current can be split into the up and down components as the following:

$$\begin{bmatrix} J_x^\uparrow \\ J_y^\uparrow \end{bmatrix} = \frac{\sigma_{xx}}{q} \begin{bmatrix} 1 & \theta_H \\ -\theta_H & 1 \end{bmatrix} \begin{bmatrix} \partial_x \mu_\uparrow \\ \partial_y \mu_\uparrow \end{bmatrix} \quad (\text{A.4})$$

$$\begin{bmatrix} J_x^\downarrow \\ J_y^\downarrow \end{bmatrix} = \frac{\sigma_{xx}}{q} \begin{bmatrix} 1 & -\theta_H \\ \theta_H & 1 \end{bmatrix} \begin{bmatrix} \partial_x \mu_\downarrow \\ \partial_y \mu_\downarrow \end{bmatrix} \quad (\text{A.5})$$

Define:

$$\mu_c = (\mu_\uparrow + \mu_\downarrow)/2$$

$$\mu_s = (\mu_\uparrow - \mu_\downarrow)/2$$

$$\begin{bmatrix} J_x^c \\ J_y^s \end{bmatrix} = \frac{\sigma_{xx}}{2q} \begin{bmatrix} 1 & \theta_H \\ -\theta_H & 1 \end{bmatrix} \begin{bmatrix} \partial_x \mu_c \\ \partial_y \mu_s \end{bmatrix} \quad (\text{SHE}) \quad (\text{A.6})$$

$$\begin{bmatrix} J_x^s \\ J_y^c \end{bmatrix} = \frac{\sigma_{xx}}{2q} \begin{bmatrix} 1 & \theta_H \\ -\theta_H & 1 \end{bmatrix} \begin{bmatrix} \partial_x \mu_s \\ \partial_y \mu_c \end{bmatrix} \quad (\text{ISHE}) \quad (\text{A.7})$$

Which is the same as the definitions in Maekawa's paper [98]:

$$\mathbf{J}_c = \mathbf{j}_q + \theta_H [\hat{z} \times \mathbf{j}_s]$$

$$\mathbf{J}_s = \theta_H [\hat{z} \times \mathbf{j}_q] + \mathbf{j}_s$$

For the second part, in the presence of spin flip scattering g_{sf} , the continuity equation will read:

$$\begin{aligned} \frac{dJ_x^\uparrow}{dx} + \frac{dJ_y^\uparrow}{dy} &= \frac{g_{sf}}{q} (\mu_\uparrow - \mu_\downarrow) \\ \frac{dJ_x^\downarrow}{dx} + \frac{dJ_y^\downarrow}{dy} &= -\frac{g_{sf}}{q} (\mu_\uparrow - \mu_\downarrow) \end{aligned} \quad (\text{A.8})$$

Using: Eq.(A.4) and Eq.(A.5), the Eq. (A.8) will become:

$$\begin{aligned}\frac{\partial^2 \mu_\uparrow}{\partial^2 x} + \frac{\partial^2 \mu_\uparrow}{\partial^2 y} &= \frac{g_{sf}}{2\sigma_{xx}}(\mu_\uparrow - \mu_\downarrow) = \frac{1}{2\lambda_{sf}^2}(\mu_\uparrow - \mu_\downarrow) \\ \frac{\partial^2 \mu_\downarrow}{\partial^2 x} + \frac{\partial^2 \mu_\downarrow}{\partial^2 y} &= -\frac{g_{sf}}{2\sigma_{xx}}(\mu_\uparrow - \mu_\downarrow) = -\frac{1}{2\lambda_{sf}^2}(\mu_\uparrow - \mu_\downarrow)\end{aligned}\quad (\text{A.9})$$

Which leads to:

$$\begin{aligned}\frac{\partial^2 \mu_c}{\partial^2 x} + \frac{\partial^2 \mu_c}{\partial^2 y} &= 0 \\ \frac{\partial^2 \mu_s}{\partial^2 x} + \frac{\partial^2 \mu_s}{\partial^2 y} &= \frac{1}{\lambda_{sf}^2} \mu_s\end{aligned}\quad (\text{A.10})$$

A.2 Spin Hall Effect: spin current and spin voltage

Now we are ready to derive the Eq.(2.4) which is re-written here:

$$J_s = \theta_H J_c \left(1 - \text{sech}(t/\lambda_{sf})\right) \approx \theta_H J_c$$

In the previous section, we provided the drift-diffusion equation for GSHE. In that form, the spin and charge electro-chemical potential are nicely decoupled into two equations.

$$\begin{bmatrix} J_x^c \\ J_y^s \end{bmatrix} = \frac{\sigma_{xx}}{2q} \begin{bmatrix} 1 & \theta_H \\ -\theta_H & 1 \end{bmatrix} \begin{bmatrix} \partial_x \mu_c \\ \partial_y \mu_s \end{bmatrix}\quad (\text{A.11})$$

$$\begin{aligned}\frac{\partial^2 \mu_c}{\partial^2 x} + \frac{\partial^2 \mu_c}{\partial^2 y} &= 0 \\ \frac{\partial^2 \mu_s}{\partial^2 x} + \frac{\partial^2 \mu_s}{\partial^2 y} &= \frac{1}{\lambda_{sf}^2} \mu_s\end{aligned}\quad (\text{A.12})$$

Now we assume that:

$$\frac{d\mu_s}{dx} = 0 \text{ in the middle of channel}$$

The spin voltage equation in Eq. (A.12) becomes

$$\frac{\partial^2 \mu_s}{\partial^2 y} = \frac{1}{\lambda_{sf}^2} \mu_s;\quad (\text{A.13})$$

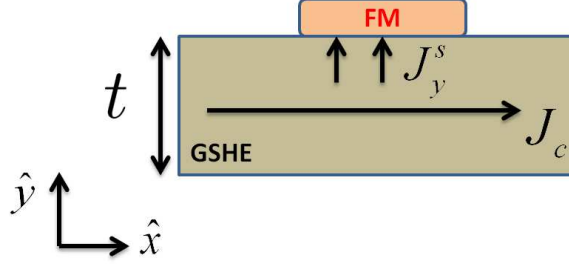


Fig. A.1. Physical structure for calculating spin current at the FM magnet

Spin current: short circuit spin voltage

First, we have to define what is the physical problem in calculating the spin current. Fig.A.2 is the physical setup showing how a ferromagnetic (FM) contact collects spin current generated from charge current flowing in the GSHE material. This problem can be translated to the following boundary conditions:

$$\mu_s(y = t) = 0; J_y^s(y = 0) = 0 \quad (\text{A.14})$$

Then we would like to solve the equation Eq.(A.13) with the boundary conditions Eq.(A.20). Now, from Eq.(A.11):

$$J_y^s = 0 \rightarrow \frac{d\mu_s}{dy} = \theta_H \frac{d\mu_c}{dx}$$

By using:

$$\frac{d\mu_c}{dx} = \frac{2qJ_x^c}{\sigma_{xx}} - \theta_H \frac{d\mu_s}{dy}$$

The boundary condition can be re-written in a new form:

$$J_y^s(y = 0) = 0 \rightarrow \frac{d\mu_s}{dy} \Big|_{y=0} = \frac{\theta_H}{1 + \theta_H^2} \frac{2qJ_c}{\sigma_{xx}} \quad (\text{A.15})$$

Therefore the whole problem can be reduced to solve the Eq.(A.13) with boundary conditions:

$$\begin{aligned} \frac{\partial^2 \mu_s}{\partial^2 y} &= \frac{1}{\lambda_{sf}^2} \mu_s \\ \mu_s(y = t) &= 0 \\ \frac{d\mu_s}{dy} \Big|_{y=0} &= \frac{\theta_H}{1 + \theta_H^2} \frac{2qJ_c}{\sigma_{xx}} \end{aligned} \quad (\text{A.16})$$

It is straightforward to show that, the solution of this equation is:

$$\mu_s(y) = \frac{\theta_H}{1 + \theta_H^2} \frac{2qJ_c}{\sigma_{xx}} \lambda_{sf} \left(\sinh(y/\lambda_{sf}) + \tanh(t/\lambda_{sf}) \cosh(y/\lambda_{sf}) \right) \quad (\text{A.17})$$

Then the spin current density can be calculated as in Eq.(A.11):

$$J_y^s(y) = \frac{\sigma_{xx}}{2q} \left[(1 + \theta_H^2) \frac{d\mu_s}{dy} - \theta_H \frac{2qJ_c}{\sigma_{xx}} \right] \quad (\text{A.18})$$

Which will give:

$$J_y^s(y = t) = \theta_H J_c \left(1 - \operatorname{sech}(t/\lambda_{sf}) \right) \approx \theta_H J_c \quad (\text{A.19})$$

Spin voltage: open circuit

For the completeness, we would like to derive the spin voltage of GSHE in the case there is no FM. Again, we would like to solve the equation Eq.(A.13) with the

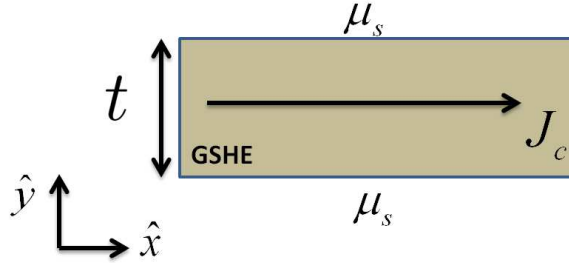


Fig. A.2. Physical structure for calculating spin voltage

boundary conditions

$$J_y^s(y = t) = 0; J_y^s(y = 0) = 0 \quad (\text{A.20})$$

Similarly to the case of spin current, we re-write the boundary condition in a new form:

$$J_y^s = 0 \rightarrow \frac{d\mu_s}{dy} = \frac{\theta_H}{1 + \theta_H^2} \frac{qJ_c}{\sigma_{xx}} \quad (\text{A.21})$$

Therefore the spin voltage can be solved from the following equation with boundary conditions:

$$\begin{aligned}\frac{\partial^2 \mu_s}{\partial^2 y} &= \frac{1}{\lambda_{sf}^2} \mu_s \\ \frac{d\mu_s}{dy} \Big|_{y=0, y=t} &= \frac{\theta_H}{1 + \theta_H^2} \frac{2qJ_c}{\sigma_{xx}}\end{aligned}\tag{A.22}$$

The solution of Eq. (A.23):

$$\mu_s(y) = \frac{\theta_H}{1 + \theta_H^2} \frac{2qJ_c}{\sigma_{xx}} \lambda_{sf} \left[\sinh(y/\lambda_{sf}) + \frac{1 - \cosh(y/\lambda_{sf})}{\sinh(y/\lambda_{sf})} \cosh(y/\lambda_{sf}) \right]\tag{A.23}$$

At $y = t$, this will lead to the spin voltage expression, $V_s = \mu_s/q$:

$$V_s = \frac{\theta_H}{1 + \theta_H^2} \lambda_{sf} \frac{2J_c}{\sigma_{xx}} \tanh(t/2\lambda_{sf})\tag{A.24}$$

This result is in agreement with Zang's results [99].

B. EVALUATING DIPOLAR COUPLING TENSOR FOR IN-PLANE MAGNETS

As mentioned in the main text, we would like to analytically calculate dipolar tensor at a point $r(x, y, z)$ due to a bar magnet whose dimension is $(2x_b, 2y_b, 2z_b)$ and points in $j = x, y, z$ direction (Fig. S1):

$$[\tilde{d}]_{ij}(r) = \int_V \nabla_i \nabla_j \left(\frac{1}{|\mathbf{r} - \mathbf{r}'|} \right) dr' \quad (\text{B.1})$$

where the integration is taken over the volume V of the magnet. The field at point can be then written as:

$$\mathbf{H} = M_s [\tilde{d}]_{ij} \begin{bmatrix} m_x \\ m_y \\ m_z \end{bmatrix} \quad (\text{B.2})$$

M_s is the magnetization of the magnet. The derivation steps can be summarized as in the following way [100]:

$$\nabla \cdot \mathbf{B} = 0 \quad (\text{B.3})$$

$$\nabla \times \mathbf{H} = 0 \rightarrow \mathbf{H} = -\nabla_{\mathbf{r}} \Phi_M(\mathbf{r}) \quad (\text{B.4})$$

$$\mathbf{B} = \mu_0(\mathbf{H} + \mathbf{M}) \quad (\text{B.5})$$

which leads to the poisson equation for the magnetic potential:

$$\nabla^2 \Phi_M(\mathbf{r}) = \nabla \cdot \mathbf{M} \quad (\text{B.6})$$

Note that the poisson equation for electrostatic potential is:

$$\nabla^2 \phi_E = -\rho/\epsilon_0 \quad (\text{B.7})$$

where ρ is the charge density.

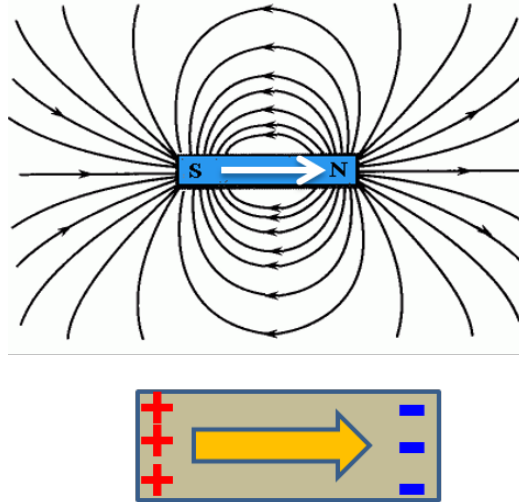


Fig. B.1. The equivalent charge model of a bar magnet.

Compare equation Eq.(B.6) to Eq.(B.7), one can argue that dipolar fields coming out from a magnet could be viewed as the electric fields coming out from the two sheets of charge ($\rho = -\nabla M$) concentrated at the poles of the magnets indicated in Fig.B.1.

Therefore, the solutions of Eq.(B.6) are:

$$\begin{aligned}\Phi_M(\mathbf{r}) &= \frac{-1}{4\pi} \int_V \frac{\nabla_{\mathbf{r}'} \cdot \mathbf{M}(\mathbf{r}')}{|\mathbf{r} - \mathbf{r}'|} d^3\mathbf{r}' \\ &= \frac{1}{4\pi} \int \mathbf{M}(\mathbf{r}') \cdot \nabla_{\mathbf{r}'} \left(\frac{1}{|\mathbf{r} - \mathbf{r}'|} \right) d^3\mathbf{r}'\end{aligned}\quad (\text{B.8})$$

$$= \frac{-1}{4\pi} \int \mathbf{M}(\mathbf{r}') \cdot \nabla_{\mathbf{r}} \left(\frac{1}{|\mathbf{r} - \mathbf{r}'|} \right) d^3\mathbf{r}' = \frac{-1}{4\pi} \nabla_{\mathbf{r}} \cdot \int \mathbf{M}(\mathbf{r}') \left(\frac{1}{|\mathbf{r} - \mathbf{r}'|} \right) d^3\mathbf{r}' \quad (\text{B.9})$$

which could be written in the following way:

$$\Phi_M(x, y, z) = -M_s m_x \phi_x(x, y, z) - M_s m_y \phi_y(x, y, z) - M_s m_z \phi_z(x, y, z) \quad (\text{B.10})$$

$$\phi_i = \frac{1}{4\pi} \frac{\partial}{\partial x_i} \left[\int_{-x_b}^{x_b} \int_{-y_b}^{y_b} \int_{-z_b}^{z_b} \frac{dx' dy' dz'}{\sqrt{(x-x')^2 + (y-y')^2 + (z-z')^2}} \right] \quad (\text{B.11})$$

and $i = x, y, z$. The field at $r(x, y, z)$ is:

$$\mathbf{H} = -\nabla_{\mathbf{r}}\Phi_M(\mathbf{r}) = M_s \begin{bmatrix} \frac{\partial\phi_x}{\partial x} & \frac{\partial\phi_x}{\partial y} & \frac{\partial\phi_x}{\partial z} \\ \frac{\partial\phi_y}{\partial x} & \frac{\partial\phi_y}{\partial y} & \frac{\partial\phi_y}{\partial z} \\ \frac{\partial\phi_z}{\partial x} & \frac{\partial\phi_z}{\partial y} & \frac{\partial\phi_z}{\partial z} \end{bmatrix} \begin{bmatrix} m_x \\ m_y \\ m_z \end{bmatrix} \quad (\text{B.12})$$

Compared to Eq.(B.2), the dipolar tensor can be calculated as:

$$\tilde{d}_{ij}(\vec{r}) = \frac{\partial\phi_i(\vec{r})}{\partial x_j} \quad (\text{B.13})$$

Note that, if the point \vec{r} is outside the magnet, \tilde{d}_{ij} is the dipolar tensor of the magnet at that point and if it is inside the magnet, \tilde{d}_{ij} is the demagnetization tensor. By extending previous work [100], we can analytically derive the expression of \tilde{d}_{ij} as

$$\begin{aligned} \tilde{d}_{xx}(x, y, z) = & - \sum_{k,l,m=1}^2 (-1)^{k+l+m} \frac{(y + (-1)^l y_b) (x + (-1)^k x_b)}{|y + (-1)^l y_b| |x + (-1)^k x_b|} \\ & \times \arctan \left\{ \frac{|y + (-1)^l y_b| (z + (-1)^m z_b)}{|x + (-1)^k x_b| \Gamma_{r,b}} \right\} \end{aligned} \quad (\text{B.14})$$

$$\tilde{d}_{xy}(x, y, z) = \sum_{k,l,m=1}^2 (-1)^{k+l+m} \ln \{z + (-1)^m z_b + \Gamma_{r,b}\}$$

$$\tilde{d}_{xz}(x, y, z) = \sum_{k,l,m=1}^2 (-1)^{k+l+m} \ln \{y + (-1)^l y_b + \Gamma_{r,b}\}$$

$$\tilde{d}_{yx}(x, y, z) = \sum_{k,l,m=1}^2 (-1)^{k+l+m} \ln \{z + (-1)^m z_b + \Gamma_{r,b}\}$$

$$\begin{aligned} \tilde{d}_{yy}(x, y, z) = & - \sum_{k,l,m=1}^2 (-1)^{k+l+m} \frac{(y + (-1)^l y_b) (x + (-1)^k x_b)}{|y + (-1)^l y_b| |x + (-1)^k x_b|} \\ & \times \arctan \left\{ \frac{|x + (-1)^k x_b| (z + (-1)^m z_b)}{|y + (-1)^l y_b| \Gamma_{r,b}} \right\} \end{aligned} \quad (\text{B.15})$$

$$\tilde{d}_{yz}(x, y, z) = \sum_{k,l,m=1}^2 (-1)^{k+l+m} \ln \{x + (-1)^k x_b + \Gamma_{r,b}\}$$

$$\begin{aligned}
\tilde{d}_{zx}(x, y, z) &= \sum_{k,l,m=1}^2 (-1)^{k+l+m} \ln \left\{ y + (-1)^l y_b + \Gamma_{r,b} \right\} \\
\tilde{d}_{zy}(x, y, z) &= \sum_{k,l,m=1}^2 (-1)^{k+l+m} \ln \left\{ x + (-1)^k x_b + \Gamma_{r,b} \right\} \\
\tilde{d}_{zz}(x, y, z) &= - \sum_{k,l,m=1}^2 (-1)^{k+l+m} \frac{(z + (-1)^m z_b) \left(x + (-1)^k x_b \right)}{|z + (-1)^m z_b| \left| x + (-1)^k x_b \right|} \\
&\quad \times \arctan \left\{ \frac{\left| x + (-1)^k x_b \right| \left(y + (-1)^l y_b \right)}{\left| x + (-1)^k x_b \right| \Gamma_{r,b}} \right\}
\end{aligned} \tag{B.16}$$

where

$$\Gamma_{r,b} = \sqrt{[x + (-1)^k x_b]^2 + [y + (-1)^l y_b]^2 + [z + (-1)^m z_b]^2} \tag{B.17}$$

C. DERIVATION OF THE JACOBIAN OF COUPLED MAGNETS INTERACTING WITH SPIN CURRENT

C.1 In-plane dipolar coupled magnets

Starting from the LLG equation of Write and Read coupled system:

$$\begin{aligned}
(1 + \alpha_W^2) \frac{d\hat{m}_W}{dt} &= -\gamma \hat{m}_W \times \vec{H}_W(\hat{m}_W, \hat{m}_R) - \alpha_W \gamma \hat{m}_W \times \hat{m}_W \times \vec{H}_W(\hat{m}_W, \hat{m}_R) \\
&\quad - \hat{m}_W \times \hat{m}_W \times \frac{\hat{I}_s}{qM_s^W V_W} + \alpha_W \hat{m}_W \times \frac{\hat{I}_s}{qM_s^W V_W} \\
(1 + \alpha_R^2) \frac{d\hat{m}_R}{dt} &= -\gamma \hat{m}_R \times \vec{H}_R(\hat{m}_W, \hat{m}_R) - \alpha_R \gamma \hat{m}_R \times \hat{m}_R \times \vec{H}_R(\hat{m}_W, \hat{m}_R)
\end{aligned} \tag{C.1}$$

where the fields are defined as:

$$\begin{aligned}
\vec{H}_W &= ([N]^W + [H_k]^W) M_W + [D]^{WR} M^R \\
\vec{H}_R &= ([N]^R + [H_k]^R) M_R + [D]^{RW} M^W
\end{aligned} \tag{C.2}$$

We mentioned in the main text that Eq.(3.29):

$$[N]^{W,R} + [H_k]^{W,R} = \begin{bmatrix} 0 & 0 & 0 \\ 0 & -H_d^{W,R}/M_s^{W,R} & 0 \\ 0 & 0 & H_c^{W,R}/M_s^{W,R} \end{bmatrix} \tag{C.3}$$

and the dipolar tensor for in-plane coupled magnets:

$$\frac{V_W}{V_R} [D]^{WR} = [D]^{RW} \approx \begin{bmatrix} D_{xx} & 0 & 0 \\ 0 & 0 & 0 \\ 0 & 0 & D_{zz} \end{bmatrix} \tag{C.4}$$

It is convenient to convert the coupled LLG equations into dimensionless equations:

$$\begin{aligned}
\frac{1 + \alpha_W^2}{1 + \alpha_R^2} \frac{d\hat{m}_w}{d\tau} &= -\hat{m}_w \times \vec{h}_W - \alpha_W \hat{m}_w \times \hat{m}_w \times \vec{h}_W - \hat{m}_w \times \hat{m}_w \times \vec{i}_s + \alpha \hat{m}_w \times \vec{i}_s \\
\frac{d\hat{m}_R}{d\tau} &= -\hat{m}_R \times \vec{h}_R - \alpha_R \hat{m}_R \times \hat{m}_R \times \vec{h}_R
\end{aligned} \tag{C.5}$$

Where $\tau = (\gamma\mu_0 H_k t)/(1 + \alpha_W^2)$ and $\vec{h}_W = \vec{H}_W/H_c^R$, $\vec{h}_R = \vec{H}_R/H_c^R$, and H_c^R is the coercive field of Read magnet. The normalized current is defined as:

$$\vec{i}_s = \frac{\vec{I}_s}{(2q/\hbar)\mu_0 H_c^R M_s^W V_W} \quad (\text{C.6})$$

and

$$\vec{h}_W = \begin{bmatrix} V_{rw} d_{xx} m_x^R \\ -h_d^W m_y^W \\ (V_{rw} d_{zz} + h_c^W) m_z^W \end{bmatrix}; \vec{h}_R = \begin{bmatrix} d_{xx} m_x^W \\ -h_d^R m_y^R \\ (d_{zz} + h_c^R) m_z^R \end{bmatrix} \quad (\text{C.7})$$

where $d_{ij} = D_{ij} M_s^W / H_c^R$; $V_{rw} = M_s^R V_R / M_s^W V_W$. The LLG equations Eq.(C.5) can be written in the following way:

$$\begin{aligned} \frac{d}{d\tau} \{m\}_i &= F_i \quad i = 1..6 \\ \{m\} &= [m_x^W \quad m_y^W \quad m_z^W \quad m_x^R \quad m_y^R \quad m_z^R] \end{aligned} \quad (\text{C.8})$$

where F_i are functions of the right hand side of Eq. by using fields in Eq.(C.5). We assumed the spin current $\vec{i}_s = (0, 0, i_z)$ or it polarizes only in the \hat{z} direction, the easy axis of magnet. The fix points ($dm/dt = 0$) of this equation are $m_z^W = \pm 1, m_z^R = \pm 1$. To derive the stability condition, we want to consider the eigenvalues of the Jacobian at the fix points:

$$J = \begin{bmatrix} \frac{\partial F_1}{\partial m_x^W} & \cdots & \frac{\partial F_1}{\partial m_z^R} \\ \vdots & \ddots & \vdots \\ \frac{\partial F_6}{\partial m_x^W} & \cdots & \frac{\partial F_6}{\partial m_z^R} \end{bmatrix} \quad (\text{C.9})$$

which leads to the following 4×4 Jacobian (in the basis of $\{m_x^W, m_y^W, m_x^R, m_y^R\}$ by noting that at fix points, $\partial F_i / \partial m_z^{W,R} = 0$ for all $i = 1..6$).

$$J = \begin{bmatrix} J_{11} & J_{12} & J_{13} & 0 \\ J_{21} & J_{22} & J_{23} & 0 \\ J_{31} & 0 & J_{33} & J_{34} \\ J_{41} & 0 & J_{43} & J_{44} \end{bmatrix} \quad (\text{C.10})$$

where

$$\begin{aligned}
J_{11} &= -\alpha_W(V_{rw}d_{zz}m_z^R m_z^W + h_c^W) - i_z W_z \\
J_{12} &= -V_{rw}d_{zz}m_z^R + h_d^W m_z^W + m_z^W h_c^W \\
J_{13} &= \alpha_W V_{rw} d_{xx} \\
J_{21} &= V_{rw}d_{zz}m_z^R + m_z^W h_c^W - i_z \alpha_W \\
J_{22} &= -\alpha_W (V_{rw}d_{zz}m_z^R m_z^W + h_c^W + h_d^W) - i_z W_z \\
J_{23} &= -V_{rw}d_{xx} W_z \\
J_{31} &= \alpha_R d_{xx} \\
J_{33} &= -\alpha_R (d_{zz}m_z^R m_z^W + h_c^R) \\
J_{34} &= - (d_{zz}m_z^W + h_d^R m_z^R + m_z^R h_c^R) \\
J_{41} &= -d_{xx} m_z^R \\
J_{43} &= d_{zz} m_z^W + m_z^R h_c^R \\
J_{44} &= -\alpha_R (d_{zz}m_z^R m_z^W + h_c^R + h_d^R)
\end{aligned} \tag{C.11}$$

C.1.1 Stability of one magnet: Sun's criteria

First, let us consider the case where we just have one magnet, namely the W magnet and there is no dipolar coupling $d_{xx} = d_{zz}$, then the Jacobian in Eq.(C.10) can be reduced into 2×2 matrix and we can even add the external magnetic field pointing in the easy axis direction $\vec{H} = [0; 0; h_{ext}]$:

$$J_W = \begin{bmatrix} -\alpha_W (h_{ext}m_z^W + h_c^W) - i_z m_z^W & \alpha_W i_z - h_{ext} - (h_d^W + h_c^W) m_z^W \\ h_{ext} + m_z^W h_c^W - i_z \alpha_W & -\alpha_W (h_{ext}m_z^W + h_c^W + h_d^W) - i_z m_z^W \end{bmatrix} \tag{C.12}$$

By analyzing the Rouths table [101] of the Jacobian, it is straightforward to show that the system is unstable when one or more elements of the first column of following Rouths table is positive:

Routh's table =

$$\begin{bmatrix} 1 & (\alpha^2 + 1) [i_z^2 + h_{c,ext}^W (h_d^W + h_{c,ext}^W)] & \lambda^2 \\ \alpha_W (h_d^W + 2h_{c,ext}^W) + 2i_z m_z^W & 0 & \lambda \\ (\alpha^2 + 1) [i_z^2 + h_{c,ext}^W (h_d^W + h_{c,ext}^W)] & 0 & 1 \end{bmatrix} \quad (C.13)$$

where we defined:

$$h_{c,ext}^W = h_{ext} m_z^W + h_c^W$$

Therefore, the system is unstable when:

$$RT_{21} = \alpha_W (h_d^W + 2h_{c,ext}^W) + 2i_z m_z^W < 0 \quad \text{OR} \quad (C.14)$$

$$RT_{31} = i_z^2 + h_{c,ext}^W (h_d^W + h_{c,ext}^W) < 0 \quad (C.15)$$

The $RT_{21} < 0$ is the stability condition for a system under the effect of spin current. It is the same as Sun's criteria known in literature [21]. On the other hand, the $RT_{31} < 0$ is stability condition of the system under the influence of the external magnetic field. When $i_z = 0$, it reduces to Sun's results [21].

C.1.2 Stability of coupled magnet

In the general case, one can derive the Routh's table from the Jacobian in Eq.(C.10)

$$\begin{bmatrix} 1 \\ RT_{21}^{ip} = a_w + a_r \\ RT_{31}^{ip} = a_w a_r + c_w + c_r - \frac{a_w c_r + c_w a_r - (\alpha_W e_w + \alpha_R e_r) V_{rw} d_{xx}^2}{a_w + a_r} \\ RT_{41}^{ip} = a_w c_r + c_w a_r - (\alpha_W e_w + \alpha_R e_r) V_{rw} d_{xx}^2 - \frac{(a_w + a_r) RT_{51}^{ip}}{RT_{31}^{ip}} \\ RT_{51}^{ip} = (c_w c_r - V_{rw} d_{xx}^2 e_w e_r) \end{bmatrix} \quad (C.16)$$

where the coefficient are defined as below:

$$\begin{aligned}
h_z^W &= h_c^W + V_{rw}d_{zz}m_z^W m_z^R, h_z^R = h_c^R + d_{zz}m_z^W m_z^R \\
a_w &= (\alpha_W h_d^W + 2\alpha_W h_z^W + 2i_{sz}m_z^W); \\
a_r &= (\alpha_R h_d^R + 2\alpha_R h_z^R); \\
c_w &= (1 + \alpha_W^2) [i_{sz}^2 + h_z^W (h_d^W + h_z^W)]; \\
c_r &= (1 + \alpha_R^2) [h_z^R (h_d^R + h_z^R)]; \\
e_w &= h_d^W + h_z^W; e_r = h_d^R + h_z^R;
\end{aligned} \tag{C.17}$$

In general, one has to look at the signs of all Rouths elements to decide the stability of the system. Note that RT_{31}^{ip} and RT_{51}^{ip} are possibly negative when there is no spin current $i_s = 0$ (both RT_{21}^{ip} and $RT_{41}^{ip} > 0$). Therefore, $RT_{31}^{ip} < 0$ or/and $RT_{51}^{ip} < 0$ are the necessary conditions for the dipolar coupling Write and Read system to be unstable.

If $\alpha_W = \alpha_R = \alpha$, $h_d^R = h_d^W = h_d$, one can decide the sign of RT_{31}^{ip} and RT_{51}^{ip} as in Eq.(3.5) which is re-written here for the purpose of clarity:

$$RT_{31}^{ip} = h_c^W + 1 + m_z^R m_z^W (1 + V_{rw}d_{zz}) \tag{C.18}$$

$$RT_{51}^{ip} = (1 + m_z^R m_z^W d_{zz})(h_c^W + m_z^R m_z^W V_{rw}d_{zz}) - V_{rw}d_{xx}^2 \tag{C.19}$$

Similarly, if $h_d^W = h_d^R = h_d$, $\alpha_W = \alpha_R = \alpha$, RT_{21}^{ip} and RT_{41}^{ip} can be simplified as: (same as Eq.(3.7))

$$RT_{21}^{ip} = m_z^W i_s + 2i_{sc}^W + \alpha m_z^W m_z^R (1 + V_{rw})d_{zz} \tag{C.20}$$

$$\begin{aligned}
RT_{41}^{ip} &= 4V_{rw} \left[\alpha m_z^W i_s (h_z^R - h_z^W) + (m_z^W i_s + 2I_{sc}^W)^2 \right] d_{xx}^2 \\
&\quad + \alpha (m_z^W i_s + I_{sc}^W) \left[(h_z^R - h_z^W)^2 h_d \right. \\
&\quad \left. + 4(m_z^W i_s + I_{sc}^W) [(m_z^W i_s + I_{sc}^W) h_z^R + I_{sc}^W h_z^W] \right]
\end{aligned} \tag{C.21}$$

where the normalized spin current is defined as:

$$i_s = \frac{\vec{I}_s \cdot \hat{z}}{(2q/\hbar)\mu_0 H_c^R M_s^W V_W}$$

and $i_{sc}^W = \alpha_W (h_c^W + h_d^W/2)$

C.2 PMA dipolar coupled magnets

PMA: Following the same procedure as for in-plane magnet with spin current $\vec{i}_s = i_{sy}\hat{y}$ and the dipolar tensor (same as Eq.(3.8))

$$\frac{V_W}{V_R}[D]^{WR} = [D]^{RW} \approx \begin{bmatrix} D_{xx} & 0 & 0 \\ 0 & -2D_{xx} & 0 \\ 0 & 0 & D_{xx} \end{bmatrix} \quad (\text{C.22})$$

One can obtain the Rouths table for PMA magnet as in the following:

$$\left[\begin{array}{c} 1 \\ RT_{21}^{PMA} = a_w + a_r \\ RT_{31} = 2V_{rw}d_{xx}^2 m_y^R m_y^W + a_w a_r + c_w + c_r \\ \quad - \frac{a_w c_r + c_w a_r - 2(\alpha_W h_y^W + \alpha_R h_y^R - i_{sy} m_y^R) V_{rw} d_{xx}^2}{a_w + a_r} \\ RT_{41} = a_w c_r + c_w a_r - 2(\alpha_W h_y^W + \alpha_R h_y^R - i_{sy} m_y^R) V_{rw} d_{xx}^2 \\ \quad - \frac{(a_w + a_r) RT_{51}}{RT_{31}} \\ RT_{51} = c_w c_r + (-2V_{rw} d_{xx}^2 h_y^W h_y^R + V_{rw}^2 d_{xx}^4) (1 + \alpha_R^2 + \alpha_W^2) \end{array} \right] \quad (\text{C.23})$$

where the coefficients are defined as:

$$\begin{aligned} h_y^W &= h_c^W - 2V_{rw} d_{xx} m_y^W m_y^R; h_y^R = h_c^R - 2d_{xx} m_y^W m_y^R \\ V_{rw} &= V_R M_s^R / V_W M_s^W \\ a_w &= (2\alpha_W h_y^W + 2i_{sy} m_y^W); a_r = 2\alpha_R h_y^R; \\ c_w &= (1 + \alpha_W^2) [i_{sy}^2 + h_y^W h_y^W]; \\ c_r &= (1 + \alpha_R^2) h_y^R h_y^R; \end{aligned} \quad (\text{C.24})$$

If $h_d^W = h_d^R = h_d, \alpha_W = \alpha_R = \alpha$, one can have Eq.(3.9) and Eq.(3.10) in the main text:

$$\begin{aligned} RT_{51}^{PMA} &= [(1 - 2m_y^R m_y^W d_{xx}) + (h_c^W - 2m_y^R m_y^W V_{rw} d_{xx})] \\ &\quad \times [(1 - 2m_y^R m_y^W d_{xx}) (h_c^W - 2m_y^R m_y^W V_{rw} d_{xx}) - V_{rw} d_{xx}^2] \end{aligned} \quad (\text{C.25})$$

$$\begin{aligned} RT_{41}^{PMA} &= -4V_{rw}^2 \alpha^2 d_{xx}^4 + \alpha (h_{yr} - h_{yw})^2 \left[h_{yr} (m_y^W i_s + i_{sc}^{W'}) - \alpha V_{rw} d_{xx}^2 \right] \\ &\quad + \left[4\alpha h_{yr} (m_y^W i_s + i_{sc}^{W'}) + i_s^2 \right] \left[\alpha h_{yr} (m_y^W i_s + i_{sc}^{W'}) + V_{rw} d_{xx}^2 \right] \end{aligned} \quad (\text{C.26})$$

and

$$h_{yw} = h_c^W - 2V_{rw}d_{xx}m_y^W m_y^R; h_{yr} = h_c^R - 2d_{xx}m_y^W m_y^R$$

$$i_{sc}^{W'} = \alpha_W(h_c^W - 2V_{rw}d_{xx}m_y^W m_y^R)$$

The maple codes used to calculate the jacobian can be found at:

<https://drive.google.com/open?id=0B9ggzdMPbfz4VDdld0xPc19ldm8&authuser=>

0

D. LLG WITH THERMAL NOISE

In Chapter 3 and Chapter 6 we did mention the simulations for W/R pair magnet but at zero temperature. Here we would like to include the thermal noise effects in the simulations so that one can obtain the probabilistic sigmoid function as in Fig.7.2(b). One of the most straightforward way to include noise in the LLG is to introduce the random magnetic field (see for example [27, 102–104])

$$(1 + \alpha^2) \frac{d\vec{m}}{d\tau} = -\gamma \vec{m} \times (\hat{h} + \hat{h}_{th}) - \gamma \alpha \times \vec{m} \times \vec{m} \times (\hat{h} + \hat{h}_{th}) - \vec{m} \times \vec{m} \times \frac{\vec{I}_s}{qN_s} + \alpha \vec{m} \times \frac{\vec{I}_s}{qN_s} \quad (\text{D.1})$$

where the random fields have zero mean and totally uncorrelated.

$$\langle \hat{h}_{th} \rangle = 0 \quad (\text{D.2})$$

$$\langle h_{th,i}(t) h_{th,k}(t') \rangle = 2D \delta_{i,k} \delta(t - t') \quad (\text{D.3})$$

$$D = \frac{\alpha}{1 + \alpha^2} \frac{k_B T}{\gamma M_s V} \quad (\text{D.4})$$

therefore the random fields in the $i = x, y, z$ directions of the magnet given the temperature T is:

$$h_{th,i} = \sqrt{\frac{\alpha}{1 + \alpha^2} \frac{2k_B T}{\gamma M_s V}} I_{ran,i}(t) \quad (\text{D.5})$$

where $I_{ran,i}$ is a gaussian distribute random number. Then, it comes to the question, how can we solve or integrate the LLG equation, Eq.(D.1), with the random fields as in Eq.(D.4)? To answer this, we note that the LLG equation can be re-written in a very general form [105]:

$$\frac{dm_i}{dt} = A_i(m, t) + B_{ik}(m, t) h_{th,k}(t) \quad (\text{D.6})$$

A_i and B_{ik} represent the deterministic and stochastic parts of the equation respectively. In general, the equation can be solved by using the Huen scheme [106]:

$$m_i(t + \Delta t) = m_i(t) + \frac{1}{2} [A_i(\bar{m}_i, t + \Delta t) + A_i(m, t)] \Delta t + \frac{1}{2} [B_{ik}(\bar{m}_i, t + \Delta t) + B_{ik}(m, t)] \Delta W_k \quad (\text{D.7})$$

where the predictor is defined as:

$$\bar{m}_i(t + \Delta t) = m_i(t) + A_i(\vec{m}, t) \Delta t + B_{ik}(\vec{m}, t) \Delta W_k \quad (\text{D.8})$$

and the Wannier's process:

$$\Delta W_k = \int_t^{t+\Delta t} h_{th,k}(t') dt' \stackrel{\text{Random Walk}}{=} h_{th,k}(t) \sqrt{\Delta t} \quad (\text{D.9})$$

If one wants to work with the Δt and don't bother to remember to carry $\sqrt{\Delta t}$ in the Eq.(D.9), we could redefine the random field as:

$$h_{th,i}(\Delta t) = \sqrt{\frac{\alpha}{1 + \alpha^2} \frac{2k_B T}{\gamma M_s V \Delta \mathbf{t}}} I_{ran,i}(t) \quad (\text{D.10})$$

This definition of field noise is also usually seen in literature [107]. Then the Huen's scheme integration can be written as:

$$m_i(t + \Delta t) = m_i(t) + \frac{1}{2} [A_i(\bar{m}_i, t + \Delta t) + A_i(m, t)] \Delta t \quad (\text{D.11})$$

$$+ \frac{1}{2} h_{th,i}(\Delta t) [B_{ik}(\bar{m}_i, t + \Delta t) + B_{ik}(m, t)] \Delta t \quad (\text{D.12})$$

and the predictor

$$\bar{m}_i(t + \Delta t) = m_i(t) + A_i(\vec{m}, t) \Delta t + h_{th,i}(\Delta t) B_{ik}(\vec{m}, t) \Delta t \quad (\text{D.13})$$

VITA

VITA

Vinh Q Diep was born in Tien Giang, Vietnam. He received bachelor degree in theoretical physics from the University of Science, Ho Chi Minh City, Vietnam in 2002. Between 2004 and 2006, he studied condensed matter physics at International Center for Theoretical Physics (ICTP) and the International Center for Advance Studies (SISSA), Trieste, Italy. In 2007, he came to Purdue University as a graduate student in the physics department and then transferred to the electrical computer and engineering department in 2009.